NTNU

Norwegian University of
Science and Technology

Design and Analysis of Optical Fiber Probes for Glucose Sensing in the Peritoneal Cavity

Per Magnus Walmsness

Master of Science in Physics and Mathematics
Submission date: June 2016
Supervisor: Ursula Gibson, IFY

Norwegian University of Science and Technology
Department of Physics

Abstract

This thesis is focused on the design and analysis of optical fiber probes for glucose sensing in the peritoneal cavity. The probes are to be used as absorption cells for near-infrared absorption spectroscopy of peritoneal fluid. A design based on miniature spherical cavities with highly reflective walls is proposed for investigation. The design is based on optical fibers entering a spherical cavity through a microfluidic channel. Active pumping of peritoneal fluid is envisioned, along with possibilities of achieving in-vivo rinsing of the probe. A Monte Carlo model is implemented to study the behaviour of the spherical cavity probe in turbid media. Results from the model suggest that the probe is resistant to losses due to light scattering, and that optical path lengths much longer than the physical size of the probe are obtainable. Early prototypes of spherical cavities are designed and fabricated in aluminium and PTFE. Investigation of the performance of the fabricated cavities, using several fiber configurations, is done experimentally. The cavities behave as expected, and the results suggest possibilities of significant performance increases when moving to a more sophisticated fabrication process. Experimental work with spherical cavities filled with fluids of various optical properties is needed to better understand the proposed design and to verify parts of the results from the model.

Sammendrag

Denne oppgaven tar for seg design og analyse av fiberoptiske prober som kan brukes for måling av glukose i bukhulen. Probene skal kunne bli brukt som absorpsjonsceller for analyse av peritonealvæske ved bruk av absorpsjonsspektroskopi. Et design basert på hule kuler hvor veggene har høy reflektivitet er foreslått for undersøkelse. Designet er basert på optiske fibre som ledes inn i en hul kule gjennom en mikrofluidisk kanal. Aktiv pumping av peritonealvæske er sett for seg, samt muligheter for å oppnå in-vivo rensing av proben. En Monte Carlo modell er implementert for å undersøke oppførselen til den sfæriske proben i væsker som både absorberer og sprer lys. Resultater fra modellen indikerer at proben er resistent mot lysspredning, og at en kan oppnå optiske lengder som er mye lengre enn den fysiske størrelsen til proben. Tidlige prototyper av hule kuler er produsert i aluminium og PTFE. Flere fiberkonfigurasjoner er brukt for å studere ytelsen til de produserte kulene eksperimentelt. Resultatene indikerer at signifikante ytelsesforbedringer er mulige om en bruker en mer sofistikert produksjonsprosess i produksjon av kulene. Eksperimentelt arbeid med hule kuler fylt med væsker av varierende turbiditet er nødvendig for å få en bedre forståelse av den sfæriske proben, og for å kunne verifisere deler av modellen.

Preface

This thesis concludes a master's degree in Applied Physics and Mathematics at the Norwegian University of Science and Technology. The work was carried out at the Department of Physics during the spring of 2016 under the supervision of Professor Ursula Gibson.

First and foremost, I would like to thank Professor Ursula Gibson for her guidance, support and patience throughout the time I have been under her supervision. In addition, I would like to thank Eric Karhu and Vedran Furtula for valuable help in the laboratory. I would also like to thank everyone in Artificial Pancreas Trondheim for introducing me to their work, and to the Fine Mechanical Workshop at the Faculty of Natural Sciences and Technology at NTNU for providing me with components used in experimental work. Lastly, I would like to thank my better half, Ine, for her everlasting support.

Per Magnus Walmsness
Trondheim, Norway
June 2016

Table of Contents

List of Tables

List of Figures

Chapter 1

Introduction

Continuous glucose monitoring (CGM) seeks to accurately monitor a persons blood glucose concentration with minimal need for the person to aid the monitoring process. This is of particular interest for diabetic patients. Diabetes mellitus, commonly called diabetes, is a metabolic disease which is mainly characterized by a lack of blood glucose control. World Health Organization (WHO) estimated that in 2014 the prevalence of diabetes was 9%, and that diabetes was responsible for 1.5 million deaths in 2012 [1]. Common long term consequences of diabetes are nerve damage, visual impairment, kidney failure and increased risk of cardiovascular diseases [2]. An order of 50% of deaths in diabetic patients may be contributed to cardiovascular diseases [3].

Diabetes is typically divided into two groups, type 1 diabetes and type 2 diabetes, and they differ in how the body responds to insulin. A person with diabetes type 1 must inject insulin to reduce blood glucose levels. For a person with diabetes type 2, insulin injections may not have any effect, leading to a need for medicaments. For people with diabetes type 1, it has been shown that keeping blood glucose levels in a healthy range reduces the risk of cardiovascular disease [4]. A well implemented CGM system may provide information to an insulin infusion pump, leading to a closed loop system which may monitor and control a persons blood glucose levels. Such a system is highly dependent on accurate measurements of glucose levels, as providing inaccurate information to the insulin delivery system may lead to a wrong amount of infused insulin.

Over the course of decades, numerous methods for glucose sensing have emerged. Sensors based on spectroscopy, enzymes and bioimpedance are common [5]. The majority of these sensing methods are based on measuring glucose in the interstitial fluid (IF) surrounding tissue cells. One problem of this approach is that the time required for glucose to diffuse from the blood to the IF may be long. A measured glucose concentration in the IF is often not equal to the true blood glucose concentration, but lags behind.

An alternative sensing location is the peritoneal cavity. The peritoneal cavity is a space surrounded by a membrane, the peritoneum. The peritoneum covers the abdominal and pelvic walls and various organs. The peritoneal cavity is filled with a thin sheet of peritoneal fluid (PF). Studies suggest that glucose measurements in PF may yield reduced latency compared to measurements in IF [6, 7]. Artificial Pancreas Trondheim (APT) is a research group at NTNU which investigates the possibility of both glucose sensing and insulin infusion in the peritoneal cavity. The long term goal of the group is the development of a clinically relevant closed loop CGM system. Such a system would contain a sensing element placed inside the peritoneal

cavity, along with an external unit containing an insulin pump and necessary components for communication with the sensing element. A small port through the abdomen would allow miniature tubing into the peritoneal cavity, allowing for insulin infusion and a potential physical connection between the sensing element and the external unit.

One of APTs partners have acquired considerable experience and knowledge of glucose sensing by spectroscopic techniques in the near-infrared (NIR) region. This experience might be taken advantage of by sensing glucose in the PF by NIR absorption spectroscopy. Light sources and detectors would then be placed on the external unit, and optical fibers would allow for remote sensing in the peritoneal cavity. The light emitted by the sources would be coupled into a source fiber, and the light would be guided to an optical fiber probe immersed in the PF, acting as an absorption cell. In the probe the light would interact with the PF before being returned to the external unit.

This thesis is focused on the design and analysis of an optical fiber probe that may be suitable for glucose sensing by NIR absorption spectroscopy in the peritoneal cavity. Fundamental optical properties of a proposed probe design will be investigated by means of modeling and experimental work. The thesis begins with a section of background information. Following this, the chosen probe design is presented. Details of the model used for investigating the probe is then given. After this, a section covering the fabrication of preliminary probe prototypes, experimental setups and the performed measurements is presented. The results obtained from modeling and from experiments are then discussed. A conclusion and an outlook end the thesis.

Chapter 2

Background

The aim of this chapter is to introduce theory and concepts that may be necessary or helpful in the understanding of the rest of the thesis.

2.1 Fundamental electromagnetic theory

The theory presented in this section is primarily based on [8].

Maxwell's equations

The governing equations for propagation of light are Maxwell's equations. In a source free medium these are

$$\nabla \times \mathbf{H} = \frac{\partial \mathbf{D}}{\partial t} \tag{2.1}$$

$$\nabla \times \mathbf{E} = -\frac{\partial \mathbf{B}}{\partial t} \tag{2.2}$$

$$\nabla \cdot \mathbf{D} = 0 \tag{2.3}$$

$$\nabla \cdot \mathbf{B} = 0 \tag{2.4}$$

where $\mathbf{E}$ is the electric field, $\mathbf{H}$ the magnetic field, $\mathbf{D}$ the electric flux density, $\mathbf{B}$ the magnetic flux density and t is time. The equations relating the fields to the flux densities are defined as

$$\mathbf{D} = \epsilon_0 \mathbf{E} + \mathbf{P} \tag{2.5}$$

$$\mathbf{B} = \mu_0 \mathbf{H} + \mu_0 \mathbf{M} \tag{2.6}$$

where $\mathbf{P}$ is the polarization density and $\mathbf{M}$ the magnetization density. The vacuum electric permittivity ϵ_0 and the vacuum magnetic permeability μ_0 are constants. In a linear, homogeneous and isotropic medium, the polarization and magnetization densities are linear in and aligned with their respective fields

$$\mathbf{P} = \chi_e \epsilon_0 \mathbf{E} \tag{2.7}$$

$$\mathbf{M} = \chi_m \mathbf{H} \tag{2.8}$$

Here χ_e and χ_e are the electric and magnetic susceptibilities, respectively. Insertion of (2.7) into (2.5), and (2.8) into (2.6) results in

$$\mathbf{D} = \epsilon \mathbf{E} \tag{2.9}$$

$$\mathbf{B} = \mu \mathbf{H} \tag{2.10}$$

where $\epsilon = \epsilon_0(1 + \chi_e)$ and $\mu = 1 + \chi_m$. Maxwell's equations can then be written as

$$\nabla \times \mathbf{H} = \epsilon \frac{\partial \mathbf{E}}{\partial t} \tag{2.11}$$

$$\nabla \times \mathbf{E} = -\mu \frac{\partial \mathbf{H}}{\partial t} \tag{2.12}$$

$$\nabla \cdot \mathbf{E} = 0 \tag{2.13}$$

$$\nabla \cdot \mathbf{H} = 0 \tag{2.14}$$

Operating with $\nabla\times$ on (2.12) and using the vector relation $\nabla \times (\nabla \times \mathbf{A}) = \nabla(\nabla \cdot \mathbf{A}) - \nabla^2 \mathbf{A}$ yields

$$\nabla^2 \mathbf{E} - \mu \nabla \times \frac{\partial \mathbf{H}}{\partial t} - \nabla(\nabla \cdot \mathbf{E}) = 0 \tag{2.15}$$

By use of (2.11) and (2.13), one obtains the wave equation for the electric field

$$\nabla^2 \mathbf{E} - \frac{1}{c^2} \frac{\partial^2 \mathbf{E}}{\partial t^2} = 0 \tag{2.16}$$

Here c is the speed of light in the medium, and is given by $c = \frac{1}{\sqrt{\epsilon\mu}}$. The ratio of the speed of light in vacuum c_0 to the speed in the medium c is defined as the refractive index

$$n = \frac{c_0}{c} = \sqrt{\frac{\epsilon\mu}{\epsilon_0\mu_0}} \tag{2.17}$$

For a boundary of different refractive indices n_1 and n_2, the boundary conditions of the fields may conveniently be summed up in a simple figure, as shown in figure 2.1. The arrows indicate continuity in longitudinal and normal directions. The figure is inspired by [8].

Monochromatic waves

Monochromatic waves are electromagnetic waves in which every component of the fields oscillate with the same frequency f, corresponding to an angular frequency $\omega = 2\pi f$. Choosing a complex notation, the electric and magnetic fields can be written

$$\mathbf{E}(\mathbf{r}, t) = \text{Re}\left\{\boldsymbol{\mathcal{E}}(\mathbf{r}) e^{i\omega t}\right\} \tag{2.18}$$

$$\mathbf{H}(\mathbf{r}, t) = \text{Re}\left\{\boldsymbol{\mathcal{H}}(\mathbf{r}) e^{i\omega t}\right\} \tag{2.19}$$

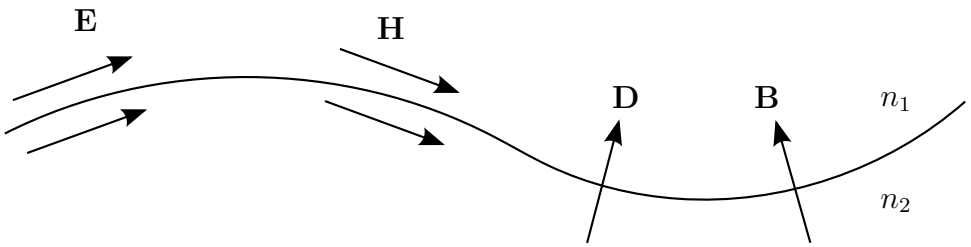

Figure 2.1: A figure showing the boundary conditions for electromagnetic fields. The two media have different refractive indices n_1 and n_2. Arrows indicate continuity in longitudinal and normal directions. The figure is inspired by [8].

$\boldsymbol{\mathcal{E}}(\mathbf{r})$ and $\boldsymbol{\mathcal{H}}(\mathbf{r})$ are now spatially varying field amplitudes, and are generally complex. By inserting (2.18) into the wave equation (2.16), one obtains the Helmoltz equation for the electric field

$$\nabla^2 \boldsymbol{\mathcal{E}}(\mathbf{r}) + k^2 \boldsymbol{\mathcal{E}}(\mathbf{r}) = 0 \tag{2.20}$$

where $k = |\mathbf{k}|$ is the wavenumber, and is defined as

$$k = n\frac{\omega}{c_0} = nk_0 \tag{2.21}$$

The equation for the magnetic field $\boldsymbol{\mathcal{H}}(\mathbf{r})$ is identical. For any component $U(\mathbf{r})$ of the electric or magnetic field, the Helmoltz equation becomes

$$\nabla^2 U(\mathbf{r}) + n^2 k_0^2 U(\mathbf{r}) = 0 \tag{2.22}$$

The simplest solution to (2.22) is a plane wave

$$U(\mathbf{r}) = U_0 e^{i(\omega t - \mathbf{k}\cdot\mathbf{r})} \tag{2.23}$$

where U_0 is a constant, complex amplitude.

Flow of electromagnetic power

The flow of electromagnetic power is governed by the Poynting vector

$$\mathbf{S} = \mathbf{E} \times \mathbf{H} \tag{2.24}$$

The unit of the Poynting vector is $[\mathbf{S}] = \mathrm{W/m^2}$, and the direction of energy flow is in the direction of $\mathbf{S}$. Since $\mathbf{S}$ oscillates at optical frequencies, what one would effectively measure is the magnitude of the time average $\langle \mathbf{S} \rangle$, where the averaging is done over a large time compared to an optical period $T = \frac{1}{f}$.

One can show that $\langle \mathbf{S} \rangle = \mathrm{Re}\,\{\boldsymbol{\mathcal{S}}\}$, where $\boldsymbol{\mathcal{S}}$ is the complex Poynting vector

$$\boldsymbol{\mathcal{S}} = \frac{1}{2} \boldsymbol{\mathcal{E}} \times \boldsymbol{\mathcal{H}}^* \tag{2.25}$$

The optical intensity may then be defined as

$$I(\mathbf{r}) = \frac{1}{2} \left| \text{Re}\{\boldsymbol{\mathcal{S}}\} \right| \tag{2.26}$$

Consider a transverse electromagnetic plane wave (TEM-wave) that satisfies (2.20) for both the electric and magnetic field

$$\boldsymbol{\mathcal{E}}(\mathbf{r}) = \boldsymbol{\mathcal{E}}_0 e^{-i\mathbf{kr}} \tag{2.27}$$

$$\boldsymbol{\mathcal{H}}(\mathbf{r}) = \boldsymbol{\mathcal{H}}_0 e^{-i\mathbf{kr}} \tag{2.28}$$

where $\boldsymbol{\mathcal{E}}_0$ and $\boldsymbol{\mathcal{H}}_0$ are complex amplitudes. Insertion of (2.18) and (2.19) into (2.11) and (2.12) yields

$$\mathbf{k} \times \boldsymbol{\mathcal{E}}_0 = \epsilon\omega\boldsymbol{\mathcal{H}}_0 \tag{2.29}$$

$$\mathbf{k} \times \boldsymbol{\mathcal{H}}_0 = -\mu\omega\boldsymbol{\mathcal{E}}_0 \tag{2.30}$$

which means that the electric and magnetic fields are orthogonal to each other and to the wave vector. Since the Poynting vector is orthogonal to both the fields, the flow of power is in the direction of the wave vector. Inserting (2.29) and (2.30) into (2.25) results in

$$\boldsymbol{\mathcal{S}} = \frac{1}{2}\boldsymbol{\mathcal{E}}_0 \times \boldsymbol{\mathcal{H}}_0^* = \frac{1}{2\eta} \left| \boldsymbol{\mathcal{E}}_0 \right|^2 \hat{\mathbf{k}} \tag{2.31}$$

where η is the impedance, and is defined as $\eta = \sqrt{\frac{\mu}{\epsilon}}$. The intensity of a TEM-wave in the direction of propagation is thus

$$I = \frac{1}{2\eta} \left| \boldsymbol{\mathcal{E}}_0 \right|^2 = \text{const} \tag{2.32}$$

So far it has been assumed that the media are transparent, and that there is no loss of electromagnetic power. Loss of power of an electromagnetic wave may be incorporated by letting the refractive index be complex. The wavenumber is then complex

$$k = nk_0 = \beta + \frac{1}{2}i\alpha \tag{2.33}$$

Here both the propagation constant β and the attenuation coefficient α are real numbers. Assuming that $\mathbf{k} = k\hat{\mathbf{z}}$, and a medium that exists for $z \geq 0$, insertion of the new value of k into (2.27) yields

$$\boldsymbol{\mathcal{E}}(z) = \boldsymbol{\mathcal{E}}_0 e^{-i\beta z - \frac{1}{2}\alpha z} \tag{2.34}$$

with corresponding intensity

$$I = I_0 e^{-\alpha z} \tag{2.35}$$

where $I_0 = \frac{1}{2\eta} \left| \boldsymbol{\mathcal{E}}_0 \right|^2$. The intensity of the wave decays exponentially as it travels through the medium, with the attenuation coefficient determining the strength of the decay with distance.

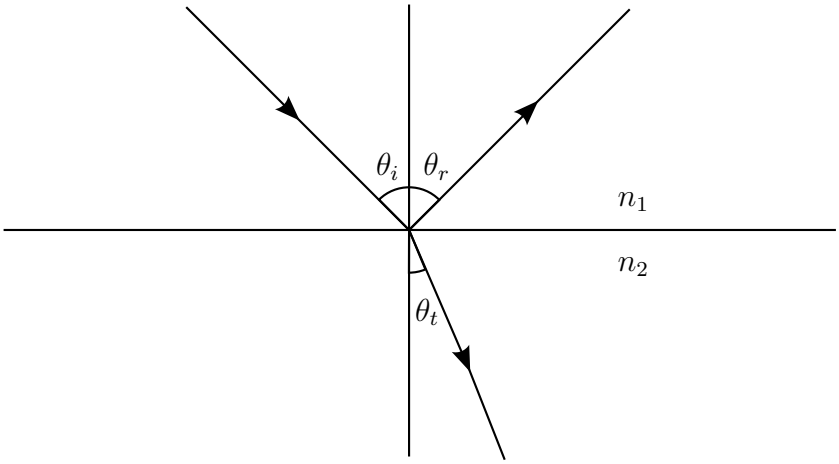

Figure 2.2: Reflection and transmission of a plane wave incident on boundary. The angle of incidence is θ_i, the reflection angle is θ_r and the transmission angle is θ_t. The boundary is defined by two refractive indices, n_1 and n_2.

Specular and diffuse reflection

Reflection of light at boundaries may be divided into two categories: specular and diffuse reflection. In specular reflection the light is reflected into a single direction, while in diffuse reflection the light is reflected into several directions.

An analysis of specular reflection may be done by considering a monochromatic plane wave incident on a boundary between media of refractive indices n_1 and n_2. Ignoring any absorption effects, a part of the wave will be reflected into the angle θ_r, and another part will be transmitted into the angle θ_t, as seen in figure 2.2. By applying the boundary conditions presented in figure 2.1, one can show that

$$\theta_i = \theta_r \tag{2.36}$$

and

$$n_1 \sin\theta_i = n_2 \sin\theta_t \tag{2.37}$$

Specular reflection is characterized by (2.36), while refraction is characterized by (2.37), which is commonly called Snell's law. Total internal reflection is obtained by letting $\theta_t = \pi/2$, which results in

$$\sin\theta_c = \frac{n_2}{n_1} \tag{2.38}$$

where θ_c is the critical angle. A necessary condition for total internal reflection is that $n_2 < n_1$.

For diffuse reflection, (2.36) does not hold. Light coming in at an angle is not scattered in a particular direction, but is instead diffused into a distribution of directions as shown in figure 2.3. Reflection from an ideal diffuse surface is said to be Lambertian. The flux emitted per surface area dA of a Lambertian surface and into the solid angle $d\Omega = \sin\theta d\theta d\phi$ is [9]

$$\frac{d\Phi(\theta)}{dA} = L_0 \cos\theta d\Omega \tag{2.39}$$

where L_0 is the radiance in units of $\mathrm{W\,m^{-2}\,sr^{-1}}$ in the direction normal to dA, ϕ is the azimuthal angle in the plane of the surface and θ is the polar angle. The flux is rotationally symmetric about

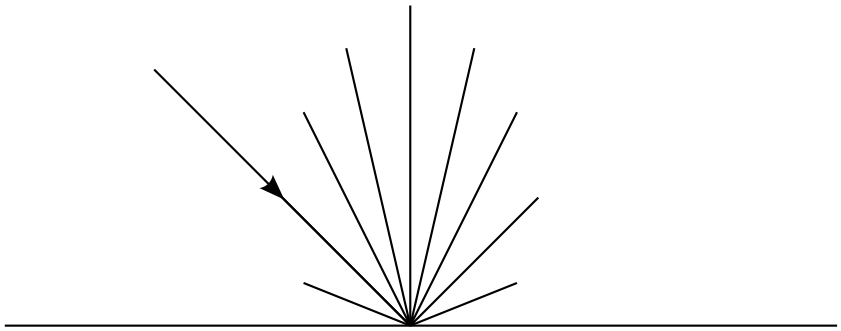

Figure 2.3: A diffuse surface scatters incoming light into a distribution of directions.

the axis normal to dA.

2.2 Optical fibers

An optical fiber is a waveguide that guides light by total internal reflection. Figure 2.4 shows a typical step-index fiber. A core of diameter d_1 and refractive index n_1 is surrounded by a cladding of diameter d_2 and refractive index n_2. Assuming linear, homogeneous and isotropic media, the equation that governs each of the components of the electric field in the fiber is the Helmholtz equation (2.22). Letting U be a component of the electric field, the equation can be written in cylindrical coordinates

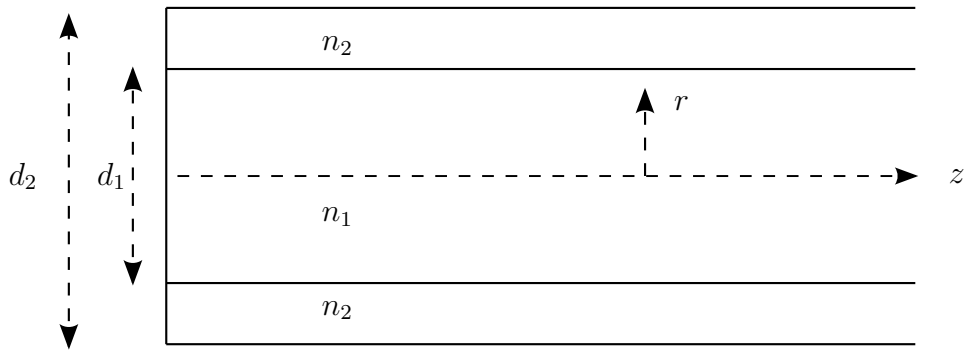

Figure 2.4: A typical step index optical fiber. The core has diameter d_1 and refractive index n_1. The cladding has diameter d_2 and refractive index n_2. r and z are part of a cylindrical coordinate system.

$$\frac{\partial^2 U}{\partial r^2} + \frac{1}{r}\frac{\partial U}{\partial r} + \frac{1}{r^2}\frac{\partial^2 U}{\partial \phi^2} + \frac{\partial^2 U}{\partial z^2} + n^2 k_0^2 U = 0 \tag{2.40}$$

Here ϕ is the azimuthal angle in the plane normal to z. By demanding that the field propagates in the z direction and that there is periodicity of 2π in ϕ, one can write

$$U(r, \phi, z) = u(r) e^{-il\phi} e^{-i\beta z} \tag{2.41}$$

where $u(r)$ is the radial field distribution, β is the propagation constant and l is an integer. Inserting (2.41) into (2.40) results in a set of equations for the radial function $u(r)$

$$\frac{d^2u}{dr^2} + \frac{1}{r}\frac{du}{dr} + \left(n_1^2k_0^2 - \beta^2 - \frac{l^2}{r^2}\right)u = 0, \quad 2r \leq d_1 \tag{2.42}$$

$$\frac{d^2u}{dr^2} + \frac{1}{r}\frac{du}{dr} + \left(n_2^2k_0^2 - \beta^2 - \frac{l^2}{r^2}\right)u = 0, \quad 2r > d_1 \tag{2.43}$$

Solving (2.42) and (2.43) can be done by recognising that the equations are of the Bessel family, and that the field should decay exponentially in the cladding. By application of tangential and normal boundary conditions of the electric and magnetic fields at the interface between the core and the cladding, the shape of $u(r)$ and β can be determined. An overview of the process can be found in [8]. The main result is a quantization of allowable solutions to (2.42) and (2.43), which are called modes

$$u(r) \rightarrow u(r)_{l,m} \tag{2.44}$$

Here l and m are indices that characterize the angular and radial dependence of $u(r)$. Each mode will propagate with a propagation constant $\beta_{l,m}$. The number of modes is characterized by the V-number, defined by

$$V = \pi\frac{d_1}{\lambda}\text{NA} \tag{2.45}$$

where NA is the numerical aperture, defined by

$$\text{NA} = \sqrt{n_1^2 - n_2^2} \tag{2.46}$$

It can be shown that there exists only a single mode if $V < 2.405$, and the fibers that satisfy this condidtion are called single mode fibers (SMF). The fibers that supports several modes are called multimode fibers (MMF). The number of modes M in a multimode fiber is approximately

$$M \approx \frac{4}{\pi^2}V^2, \quad V \gg 1 \tag{2.47}$$

The number of modes of a fiber is important when light is to be coupled into the fiber. The field distribution of the light must match the distribution defined by the modes in order to achieve efficient coupling. Fibers with a large number of modes are easier to couple light into, because there will be a large overlap between the light distribution and the modes. A multimode fiber with a large core and a large numerical aperture will have the potential to collect more light than a smaller fiber.

The acceptance angle θ_0 of a fiber puts a constraint on the directions of incoming light that will be guided by a fiber. Incoming light with angles greater than θ_0 will decay in the cladding. The geometry can be seen in figure 2.5. By applying (2.37) at the medium-core boundary and demanding total internal reflection at the core-cladding boundary, the acceptance angle is given by

$$n_0 \sin\theta_0 = \text{NA} \tag{2.48}$$

where n_0 is the refractive index of the surrounding medium. The exit angle of the fiber is also given by (2.48). The solid angle subtended by the fiber is

$$\Omega = \int_0^{\theta_0} \sin\theta d\theta d\phi = 2\pi(1 - \cos\theta_0) \tag{2.49}$$

By using (2.48), the solid angle may be represented in terms of the numerical aperture

$$\Omega = 2\pi \left[1 - \sqrt{1 - (\mathrm{NA}/n_0)^2}\right] \tag{2.50}$$

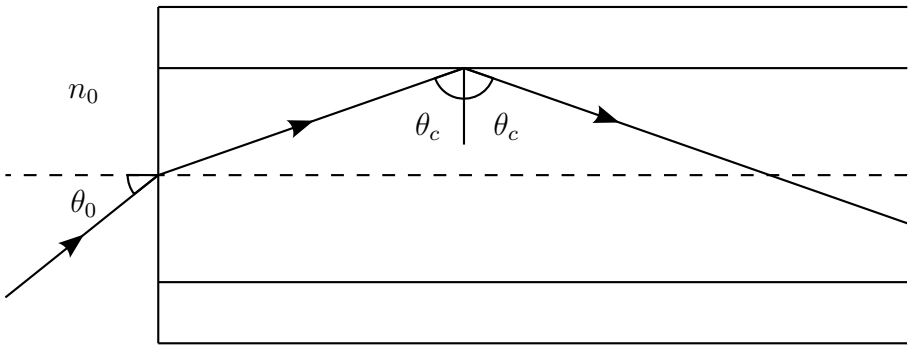

Figure 2.5: The maximum angle of incidence θ_0 of incoming light that allows for total internal reflection in a step index fiber. θ_c is the critical angle and n_0 is the refractive index of the medium surrounding the fiber.

2.3 Optical absorption and scattering

Photons travelling through a medium interacts with the medium through processes such as scattering and absorption. These interactions are in general complex. In many cases, a system may be analysed in which the interactions between photons and the medium are reduced to a set of coefficients.

2.3.1 Absorption and scattering coefficients

Consider a narrow, uniform beam of photons of flux $\Phi(0)$ incident on a medium. The beam is confined to a cross sectional area a, and $\Phi(z)$ is the amount of photons passing through a a distance z into the medium per unit time. Let the medium first be purely absorbing. Each photon incident on a particle in the medium has a chance of being absorbed, quantified by the absorption cross section σ_a of the particle. As the beam of photons propagate through the medium, photons are lost due to absorption. In a slice of thickness dz at position z, a flux $d\Phi$ is lost. This flux is proportional to the amount of photons in the slice and to the total chance of absorption by all the particles in the slice. The change in flux is thus

$$d\Phi(z) = -\eta\sigma_a\Phi(z)dz \tag{2.51}$$

where η is the number density of the absorbing particles. Assuming that the medium is homogeneous, the solution to (2.51) is

$$\Phi(z) = \Phi(0)e^{-\alpha_a z} \tag{2.52}$$

where $\alpha_a = \eta\sigma_a$ has been defined as the absorption coefficient of the medium.

For a purely scattering medium, the photons are not absorbed but scattered out of the beam path as seen in figure 2.6. The resulting flux is equal to (2.52), with the absorption coefficient replaced by the scattering coefficient $\alpha_s = \eta\sigma_s$, where σ_s is the scattering cross section of the particles.

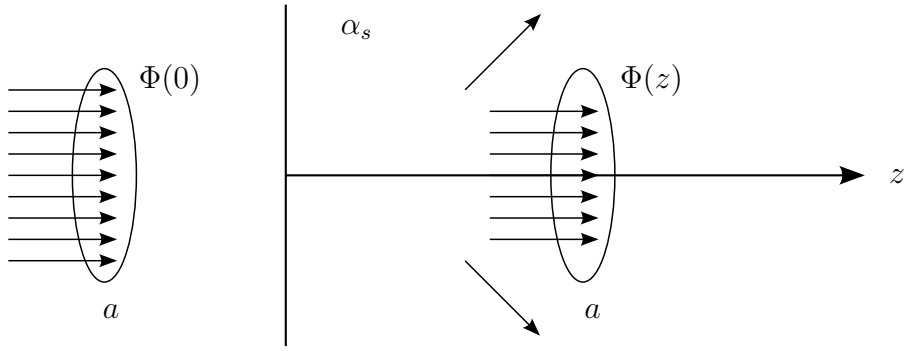

Figure 2.6: Attenuation of a beam of photons in the z-direction due to photons being scattered out of the beam path. The medium has scattering coefficient α_s.

The combined effect of absorption and scattering yields

$$\Phi(z) = \Phi(0)e^{-\alpha_t z} \tag{2.53}$$

where

$$\alpha_t = \alpha_a + \alpha_s \tag{2.54}$$

is the attenuation coefficient. This result is similar to what was obtained in (2.35), where a plane monochromatic wave is attenuated as it propagates through a medium. The simple relation in (2.53) typically breaks down when the particles in the medium interacts strongly with each other and if photons are scattered multiple times.

2.3.2 Absorption spectroscopy

Absorption spectroscopy is based on the principle of relating loss of detected light to a concentration of absorbing particles. Consider a classical single pass absorption cell of thickness L filled with, for instance, water. A beam of light is passed through the cell, and a flux Φ_0 is detected. Some absorbing particles are then added to the cell, yielding an unknown number density η of absorbing parcticles, and a flux $\Phi(\eta)$ is detected. The process is illustrated in figure 2.7. One can then define the transmission as

$$T(\eta) = \frac{\Phi(\eta)}{\Phi_0} \tag{2.55}$$

From (2.52) one expect

$$T(\eta) = e^{-\eta\sigma_a L} \tag{2.56}$$

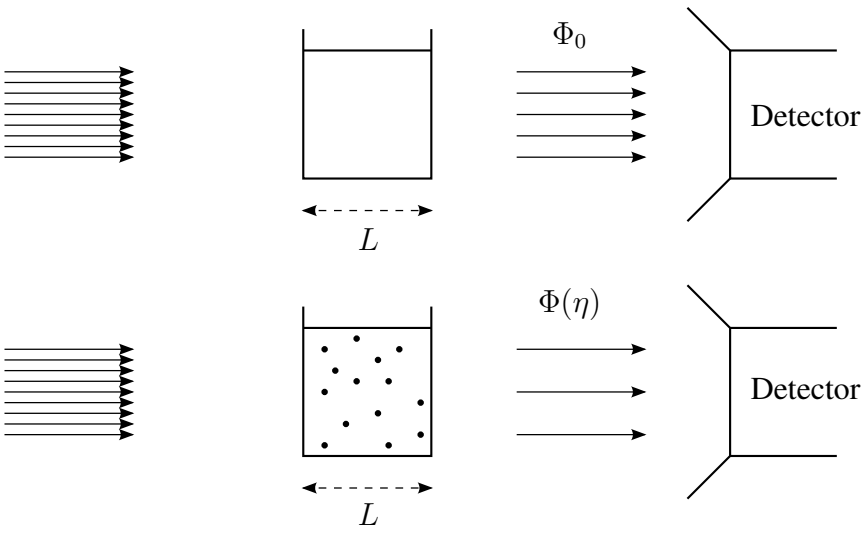

Figure 2.7: A typical absorption spectroscopy experiment. A reference measurement is done before the cell is filled with absorbing particles. The resulting change in flux Φ is related to the amount of absorbing particles present η. The path length of the light is L.

where σ_a is the cross section of the absorbing particles. Taking the negative logarithm of T, one can define the absorbance as

$$A(\eta) = -\ln T(\eta) = \eta \sigma_a L \tag{2.57}$$

Knowing the path length L and σ_a, one can then estimate how many particles is inside the cell.

Note that the absorbance is here defined with the natural logarithm. In the field of chemistry it is customary to define the absorbance in base 10. In addition, one operates with molar absorptivities ϵ_a and molar concentrations of particles instead of number densities and cross sections. The molar absorptivity is defined as

$$\epsilon_a = \frac{N_a \sigma_a}{\ln 10} \tag{2.58}$$

where N_a is Avogadro's number.

2.3.3 Glucose prediction

When light of certain wavelengths are incident on a glucose molecule the light may induce atomic vibrations in the molecule. The molecule will absorb a photon and be excited to a higher energy state. Fundamental vibrations of the glucose molecule correspond to wavelengths in the mid-infrared region, while higher order vibrations correspond to wavelengths in the NIR region. The wavelength regions where glucose absorbs the strongest in the NIR are the first overtone band at $1500-1800$ nm and the combination band at $2050-2300$ nm [10]. The second overtone band, in which glucose absorbs considerably less, is located at $1100 - 1300$ nm [10].

The water spectrum is of importance due to water being the main component of biofluids. In figure 2.8 the absorption coefficient of water is shown as a function of wavelength over the near-infrared range. For a typical physiological blood glucose concentration, the absorption coefficient of glucose is several orders of magnitude smaller than the absorption coefficient of

water. Figure 2.9 shows the absorption coefficients of aqueous glucose at a concentration of 5 $\mathrm{mmol\,L^{-1}}$ in the overtone band.

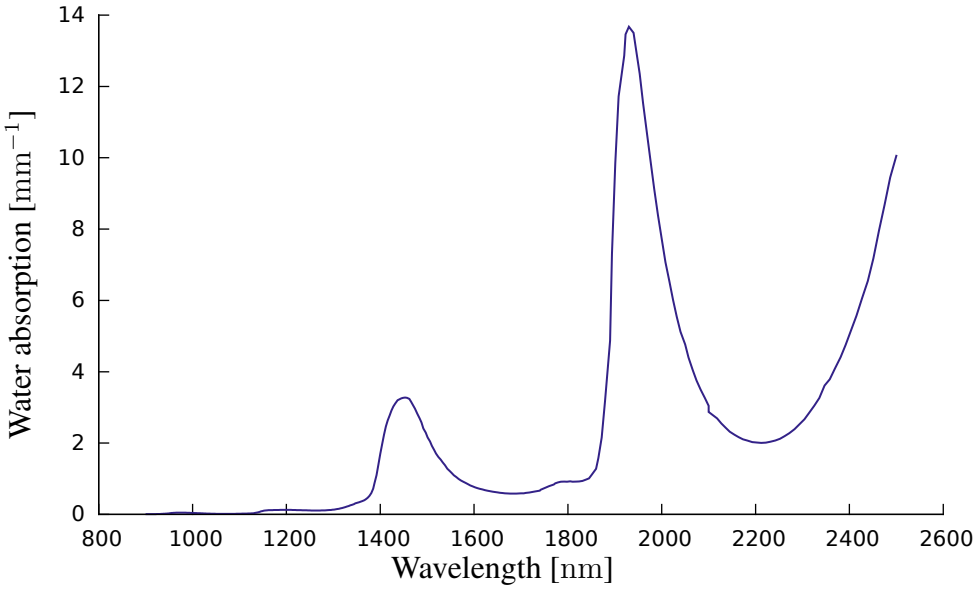

Figure 2.8: The absorption coefficient of water as a function of wavelength in the NIR region. The data is adapted from [11].

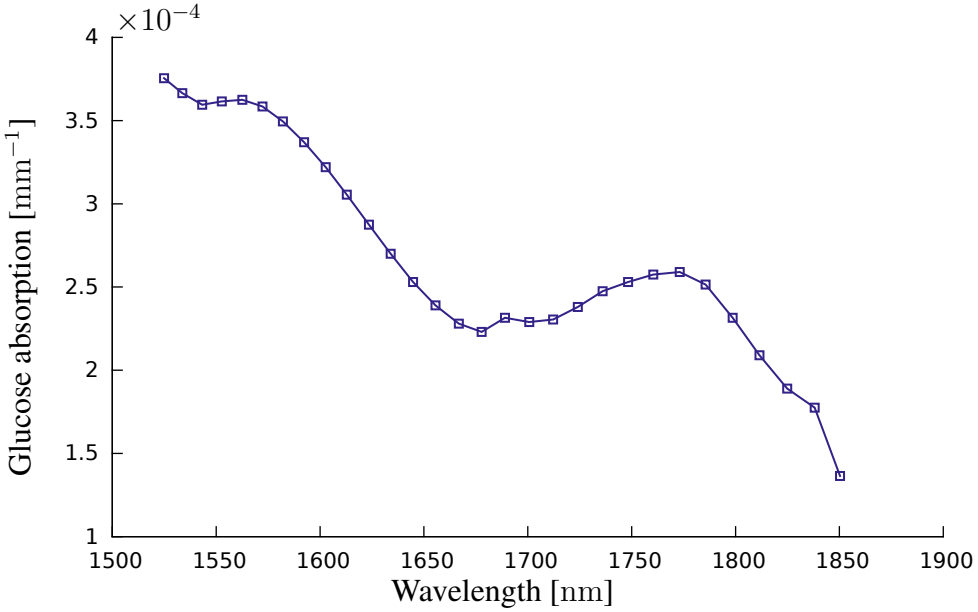

Figure 2.9: The absorption coefficient of a $5\mathrm{mmol\,L^{-1}}$ aqueous glucose solution in the overtone band. The data is adapted from [12].

As the absorption of glucose is so weak, the simple procedure presented in 2.3.2 is generally not adequate. Instead one turns to multivariate calibration techniques [13]. These techniques seek to build prediction models based on a set of spectral measurements of known glucose concentrations. The spectral measurements are not limited to the bands where glucose absorbs

the strongest, as there may be information in other regions that can be correlated to the presence of glucose. Calibration models may thus be built on information from a large spectral range [13–16].

2.4 Integrating sphere

The integrating sphere is a hollow, spherical cavity with highly reflective walls, causing confinement of light that is passed into the sphere. The walls scatters the light diffusely, and so any spatial information from the light source is quickly destroyed. In idealized situations, the distribution of light flux inside the sphere is uniform and independent of direction. Integrating spheres may be used to measure physical quantities where no directional information is needed. Examples of these quantities may be the total power emitted from a light source, or the total amount of light reflected off a surface.

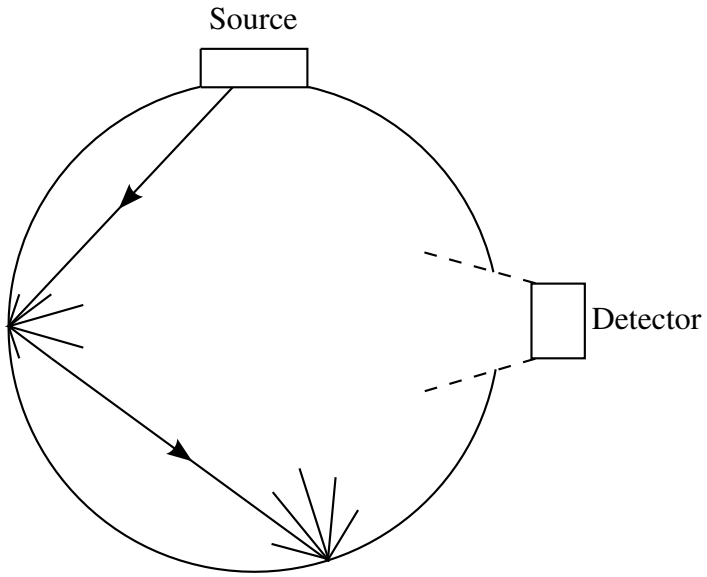

Figure 2.10: A typical integrating sphere. A source emits light that is diffused by the sphere wall. A detector collects light after multiple reflections.

The integrating sphere may be analyzed by first considering the exchange of flux between two differential areas, dA_1 and dA_2. The geometry is shown in figure 2.11. Let dA_1 emit a total flux $d\Phi_1$. If the walls are assumed to obey Lambertian reflectance, as defined in (2.39), the flux emitted from dA_1 into the solid angle $d\Omega$ is

$$d\Phi_1(\theta) = L_0 dA_1 \cos\theta d\Omega \tag{2.59}$$

where L_0 is the radiance in the direction normal to dA_1. The notation is such that when the flux is written with explicit dependence on θ, it is directional. An expression for L_0 can be found by integrating $d\Phi_1(\theta)$ in (2.59) over all angles

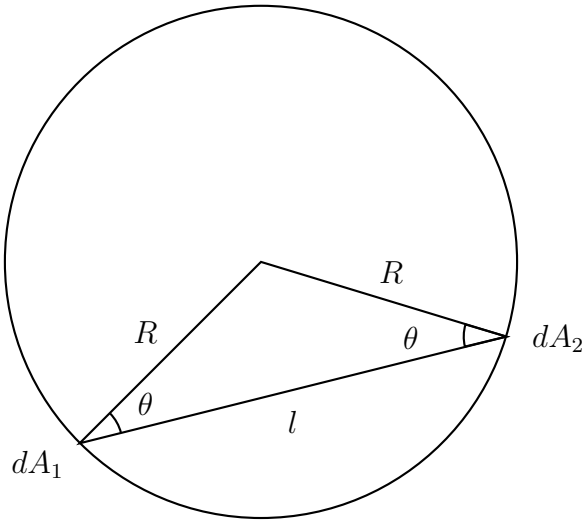

Figure 2.11: The geometry for exchange of flux between two differential areas dA_1 and dA_2 in an integrating sphere of radius R.

$$\begin{aligned} d\Phi_1 &= \int_0^{2\pi} \int_0^{\pi/2} d\Phi_1(\theta) \\ &= 2\pi L_0 dA \int_0^{\pi/2} \cos\theta \sin\theta d\theta \\ &= \pi L_0 dA \end{aligned} \tag{2.60}$$

Inserting the expression for L_0 into (2.59) results in

$$d\Phi_1(\theta) = \frac{d\Phi_1}{\pi} \cos\theta d\Omega \tag{2.61}$$

Let $d\Phi_{1-2}$ be the flux emitted by dA_1 which is received by dA_2. Using (2.61), this can be written

$$d\Phi_{1-2}(\theta) = \frac{d\Phi_1}{\pi} \cos\theta d\Omega_{1-2} \tag{2.62}$$

where $d\Omega_{1-2}$ is the solid angle subtended by dA_2. From the geometry in figure 2.11, this solid angle is

$$\begin{aligned} d\Omega_{1-2} &= \frac{dA_2 \cos\theta}{l^2} \\ &= \frac{dA_2}{4R^2 \cos\theta} \\ &= \frac{dA_2}{A} \frac{\pi}{\cos\theta} \end{aligned} \tag{2.63}$$

where A is the total area of the sphere. Insertion of (2.63) into (2.62) results in

$$d\Phi_{1-2}(\theta) = \frac{dA_2}{A} d\Phi_1 \tag{2.64}$$

Since the exchange of flux is independent of direction, and the surfaces dA_1 and dA_2 are arbitrary, the flux emitted from a surface is uniformly distributed on the sphere walls.

Assume now that there is a set of ports on the sphere. The ports take up a fraction f of the total surface area

$$f = \frac{1}{A}\sum_i A_i \tag{2.65}$$

where A_i is the area of port number i. The reflectivity of the wall is ρ, it is assumed that the ports reflects no light. Let an initial flux Φ_0 be directed uniformly onto the sphere surface. This flux will be reflected multiple times by the sphere wall. For each reflection, the strength of the reflected flux is decreased due to the reflectivity of the wall, but also due to the flux that is lost to the port areas. The flux inside the sphere Φ is thus a sum of reflected fluxes of decreasing strength.

$$\Phi = \rho(1-f)\Phi_0 + \rho^2(1-f)^2\Phi_0 + \rho^3(1-f)^3\Phi_0 + \dots \tag{2.66}$$

After k reflections, the flux is

$$\Phi = \Phi_0 \sum_{n=1}^{k} \rho^n (1-f)^n \tag{2.67}$$

Since $\rho(1-f) < 1$, the sum converges to

$$\Phi = \Phi_0 \rho(1-f)\frac{1-\rho^k(1-f)^k}{1-\rho(1-f)} \tag{2.68}$$

If the input flux is provided continuously, the flux inside the sphere is in a steady state, and can be found by letting $k \to \infty$ in (2.68). In this case the flux becomes

$$\Phi = \Phi_0 \frac{\rho(1-f)}{1-\rho(1-f)} \tag{2.69}$$

The radiance L on the surface of the sphere is thus

$$L = \frac{1}{\pi A(1-f)}\Phi = \frac{\Phi_0}{\pi A}\frac{\rho}{1-\rho(1-f)} \tag{2.70}$$

If a fiber is placed in a port for light collection, the flux that will be collected by the fiber is

$$\Phi_f = L A_{core} \Omega_f \tag{2.71}$$

where A_{core} is the area of the core of the fiber and Ω_f is the solid angle subtended by the fiber. By using (2.50) and (2.70), and assuming that the refractive index of the interior medium is $n = 1$, the collection efficiency of the integrating sphere, defined as $\epsilon_c = \Phi_f/\Phi_0$, is

$$\epsilon_c = \frac{A_{core}}{A}\frac{\rho}{1-\rho(1-f)} 2\left(1 - \sqrt{1-\mathrm{NA}^2}\right) \tag{2.72}$$

If $\mathrm{NA} \ll 1$, the collection efficiency in (2.72) simplifies to

$$\epsilon_c \approx \frac{A_{core}}{A}\frac{\rho}{1-\rho(1-f)}\mathrm{NA}^2, \quad \mathrm{NA} \ll 1 \tag{2.73}$$

2.5 Lock-in amplifier

A lock-in amplifier is a phase sensitive detector, capable of extracting a signal in extremely noisy environments. A lock-in amplifier can detect and amplify an incoming AC signal of a known frequency, and produce a DC signal which is proportional to the incoming signal. In general, one can think of a lock-in amplifier as a device which contains a filter with narrow bandwidth while at the same time providing amplification.

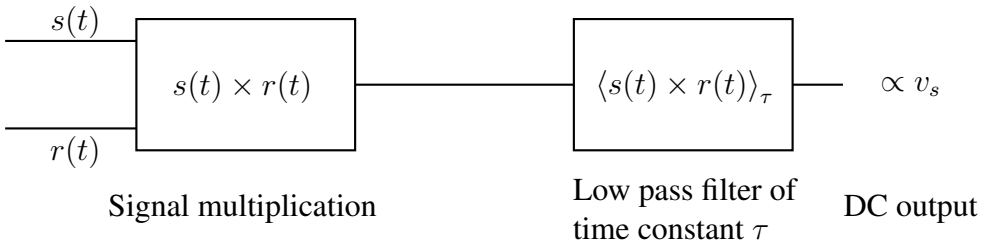

Figure 2.12: Two basic components of a lock-in amplifier. A reference signal $r(t)$ is multiplied by an incoming signal $s(t)$, and the DC term of the resulting signal is extracted by a low pass filter of time constant τ.

A simplified diagram showing basic components of a lock-in amplifier is shown in figure 2.12. Let the input signal $s(t)$ consist of two parts. The first part, the signal of interest, one can for simplicity assume is sinusoidal. The second part is noise at frequencies that differ from the sinusoidal signal. The input signal can then be written

$$s(t) = v(t) + \psi(t) \tag{2.74}$$

where

$$v(t) = v_s \sin(\omega_s t + \phi_s) \tag{2.75}$$

Here v_s is the amplitude, ω_s the frequency and ϕ_s the phase of the signal of interest. The noise term is $\psi(t)$, and t is time. A lock-in amplifier will generate a reference signal $r(t)$ which is also assumed to be sinusoidal

$$r(t) = v_r \sin(\omega_r t + \phi_r) \tag{2.76}$$

Here v_r is the amplitude, ω_r the frequency and ϕ_r the phase of the reference signal. A lock-in amplifier will effectively multiply the input signal with the reference signal, yielding

$$\begin{aligned} s(t)r(t) &= v_s v_r \sin(\omega_s t + \phi_s)\sin(\omega_r t + \phi_r) + r(t)\psi(t) \\ &= \frac{1}{2} v_s v_r \cos[(\omega_s - \omega_r)t + \phi_s - \phi_r] \\ &- \frac{1}{2} v_s v_r \cos[(\omega_s + \omega_r)t + \phi_s + \phi_r] + r(t)\psi(t) \end{aligned} \tag{2.77}$$

If the reference signal is driven at the same frequency as the input signal, $\omega_s = \omega_r$, there will be a DC term in (2.77). The two other terms both oscillate in time, and consequentially can be averaged out. The averaging process is essentially performed by a low-pass-filter of time constant τ. The output from the lock-in amplifier is thus

$$s(t)r(t)_{DC} \propto Gv_s \tag{2.78}$$

where G is some amplification. This amplification is often characterized by the sensitivity q of the instrument. A sensitivity of $q = 1$ µV means that one expects the incoming signal to have an amplitude of the order of 1 µV. This signal will then be amplified to the full scale of the instrument, which is typically on the order of 1 V.

To use a lock-in amplifier in an optical setup one must be able to modulate the light at a known frequency, and supply the lock-in with a reference signal of the same frequency. The modulation may be done by either modulating the output of a source directly, or by obstructing the beam path periodically.

2.6 Statistics

A random number ξ has an associated probability density function (PDF) $p(\xi)$ such that the probability of picking a number between ξ and $\xi + d\xi$ is $p(\xi)d\xi$. Conservation of probability is expressed as

$$\int_{-\infty}^{\infty} p(\xi)d\xi = 1 \tag{2.79}$$

The cumulative density function (CDF) is defined as

$$F(\xi) = \int_{-\infty}^{\xi} p(x)dx \tag{2.80}$$

where $F(\xi)$ is interpreted as the probability of picking a number that is less than ξ. $F(\xi)$ is a monotonically increasing function, and $F(1) = 1$ by use of (2.79). The average of ξ is

$$\bar{\xi} = \int_{-\infty}^{\infty} \xi p(\xi)d\xi \tag{2.81}$$

and the standard deviation is

$$\sigma_\xi = \int_{-\infty}^{\infty} \left(\xi - \bar{\xi}\right)^2 p(\xi)d\xi \tag{2.82}$$

Consider a sample of numbers ξ_i, $i = 1, 2, 3, \ldots, N$, collected from a population of numbers of unknown distribution. The mean of the distribution is estimated by the sample mean

$$\langle\xi\rangle = \frac{1}{N}\sum_{i=1}^{N} \xi_i \tag{2.83}$$

while the standard deviation of the distribution is estimated by the unbiased sample standard deviation s, defined by

$$s^2 = \frac{1}{N-1}\sum_{i=1}^{N} (\xi_i - \langle\xi\rangle)^2 \tag{2.84}$$

If one repeats the process of sampling from the population n times, one is left with n sample means and n sample standard deviations. The sample mean and sample standard deviation are then also random numbers. The deviation of the sample mean, often called the standard error, may be shown to be

$$\sigma_e = \frac{s}{\sqrt{n}} \tag{2.85}$$

The error in predicting the mean of the unknown population is thus reduced when increasing the number of samples drawn from the population.

Random numbers on a computer

Random numbers on a computer are usually provided by a pseudorandom number generator (PRNG). A PRNG contains an algorithm for generating seemingly random numbers. The sequence of random numbers is initiated with a seed, and the numbers that follow are deterministic. Each seed will therefore generate a different sequence of numbers. This is particularly important if one needs to reproduce some numerical calculation that rely on random numbers.

A PRNG will in general give out uniformly distributed numbers between 0 and 1. Usually it is wanted to sample numbers from a known distribution $p(\xi)$. If this distribution has an invertible cumulative distribution $F(\xi)$ one can use the method of inverse transform sampling. The PRNG will then be used to generate a number x between 0 and 1, and passing this to the inverted cumulative distribution function yields a number ξ which is distributed according to $p(\xi)$

$$\xi = F^{-1}(x), \quad x \in [0, 1] \tag{2.86}$$

Chapter 3

Probe design

This chapter will present some considerations that must be taken into account when designing a optical fiber probe for use in the peritoneal cavity. Some possible design principles will be presented, before the chosen design is detailed.

3.1 Design considerations

A number of considerations must be taken into account when designing an optical fiber probe that may be used in the peritoneal cavity. The amount of light collected and the optical path length are key design elements. There are restrictions to the physical size of the probe, both in terms of the available volume of PF and comfort of a person having a probe implanted. The exchange of fluid within the sampling volume of the probe is important, as this may affect the dynamic response of the whole sensing system. Lastly, for the probe to perform in the long term, it must be resistant to degradation.

The path length of the light in the probe decides to which degree the light is able to interact with the medium. For weakly absorbing fluids, a long path length is necessary to obtain a measurable absorption. For a strongly absorbing fluid, a short path length may be necessary in order to keep the measured signal above the noise level of the detection system. The absorption coefficients of water and glucose differ by several orders of magnitude, as seen in section 2.3.3. The low absorption of glucose indicates that a long path length is necessary, but the strong absorption of water in certain regions limits the amount of detectable light. The optimal path length is thus highly dependent on which spectral region one is interested in [10]. For detection of glucose by absorption spectroscopy, the main challenge is obtaining signals which contain glucose specific information. It is common to perform spectroscopic measurements across a large wavelength range in order to obtain more information that can be correlated to the presence of glucose. For in-vitro prediction of glucose, this may not be a problem as one can choose several path lengths for different wavelength regions [17]. The path length achievable with an optical fiber probe in an in-vivo situation is typically constant, and this presents a major design challenge. As an example, a minimum path length of $2\ \mathrm{mm}$ has been suggested for the detection of aqueous glucose at physiological concentrations in the first overtone band [18], while a path length on the order of $8\ \mathrm{mm}$ is suggested for the second overtone band [10].

For a given probe geometry, more collected light typically means that there is more information that can be used in processing of an acquired signal. The collection efficiency of the probe, defined as the fraction of power returned from the probe relative to the total power launched

into the probe, may be a limiting factor in the sensing system. If the collection efficiency is low, one may have to compensate by increasing the power output of the source. This might not be possible or feasible in the envisioned CGM system. The required collection efficiency is highly dependent on the detection system and the wavelength range of interest. For spectral regions where water absorbs strongly, one may typically be limited by detector noise [18, 19]. In this situation the noise is independent of the signal. This means that a higher throughput of light directly, i.e a higher collection efficiency, increases the signal to noise ratio, yielding an improved signal quality and improving the chances for building an accurate glucose prediction model.

The amount of peritoneal fluid available in the peritoneal cavity is assumed to be below $25\ \mathrm{mL}$ [20], and may be even be on the order of $1\ \mathrm{mL}$ [21]. This amount may also be divided over a large area. The probe should thus require a much smaller amount of fluid to function reliably. Volumes on the order of $1\ \mu\mathrm{L}$ may be necessary. A small sampling volume will also allow for faster sensing dynamics, as it takes less time for glucose to diffuse into the volume. Reducing the size of the probe while retaining a minimum path length and a large collection efficiency may be contradictory tasks. Increasing the amount of collected light may require multimode fibers of large core sizes or several smaller fibers placed in a bundle, but this results in reduced flexibility of the fibers connecting the probe to the rest of the system. This reduction in flexibility may be unacceptable as the CGM system must allow a patient to move and behave in a normal way.

To detect changing concentrations of glucose, there must be an exchange of fluid within the sample volume of the probe. This exchange may be either passive or active. In a passive design, one relies on glucose diffusing into the sample volume. In an active design, the exchange of fluid is facilitated. Purely diffusion driven dynamics in the peritoneal cavity is unlikely, as there will be convective terms due to the movement of the peritoneum. This movement may, for example, be caused by breathing. Apart from letting fluid into the sampling volume of the probe, the probe should also keep unwanted material, like tissue, separated from the optical path. This means that the sampling volume should be partly shielded. Increased shielding of the sample volume might result in a weakened fluid exchange, which will increase the detection latency of the sensor system.

For the probe to perform in the long term, it must be resistant to degradation. A probe implanted in the peritoneal cavity may induce a foreign body reaction [22]. Biofouling, formation of biofilms and fibrous encapsulation [23, 24] could severely affect the optical properties of the probe.

3.2 Possible designs

A few possible probe design principles have been considered. A short description of these are given in the following.

3.2.1 Coaxial transflectance probe

A general coaxial transflectance probe is based on a set of aligned fibers facing a mirror. The emitted light travels to the mirror, is reflected, and travels back to the fibers. The geometry of such a probe with two equal fibers is shown in figure 3.1. The distance between the fibers and the mirror is $L/2$, where L is the typical optical path length achievable with the probe. This design principle is commonly found in commercially available optical fiber probes for absorption spectroscopy. The two fibers are typically replaced by a bundle of fibers in order to increase the collection efficiency. Only the cores of the collection fibers will effectively collect and guide light, any other area may be considered dead space. The packing of fibers in such a bundle is thus of importance. With fibers of equal size and a circular bundle boundary, a common fiber configuration is a hexagonal geometry where one central source fiber is surrounded by six collection fibers. With the mirror removed, this design is commonly used in reflectance and Raman probes [25].

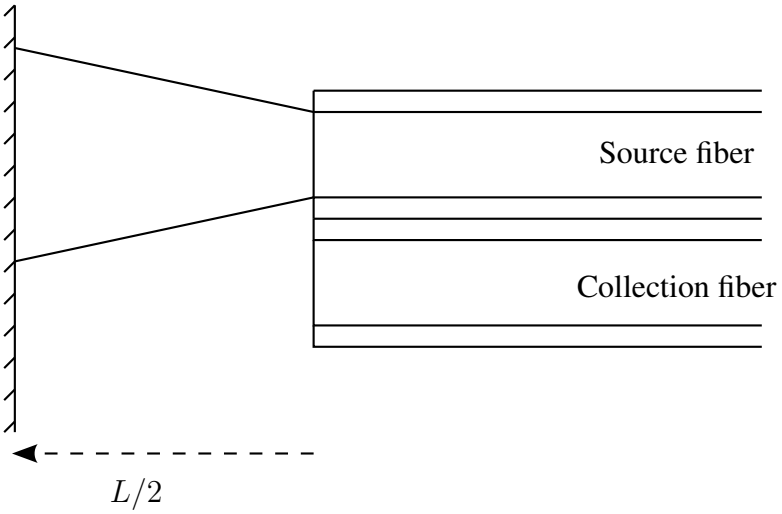

Figure 3.1: The basic design of a coaxial transflectance probe. Two fibers; a source fiber and a collection fiber, are directed towards a reflective surface. The distance between the surface and the fibers is $L/2$.

This design is simple, and it should in principle be easy to fabricate a miniature coaxial transflectance probe that could be used in a passive setup in the peritoneal cavity. One drawback of the coaxial design is the strong dependence on the performance of the mirror. There may be complications due to biofilms forming on the mirror, and the long term performance of such a probe is questionable. Long path lengths will also make the probe particularly susceptible to scattering of light, which will reduce the amount of light collected by the probe.

3.2.2 Fiber-to-fiber probe

A fiber-to-fiber probe is based on a design where the optical path is obtained by cutting off and removing a length of the fiber transmitting the light. The result of this is a fiber which emits light directly towards another fiber. Reversal of the direction of light may be done by a mirror which is not in contact with the surrounding medium. Figure 3.2 shows the principles of the design.

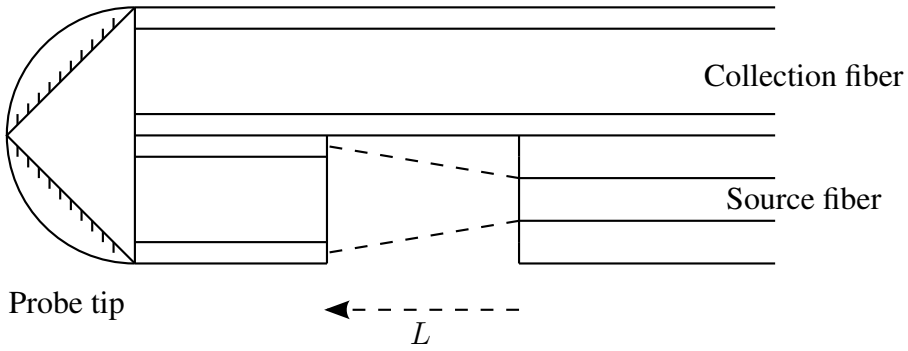

Figure 3.2: The design principles of a fiber-to-fiber probe. A source fiber is facing another fiber which collects emitted light. The distance between the facing fibers is L. Light is reflected in the probe tip.

The probe tip contains the mirror which reflects and couples the light into the second fiber. This tip could be made of a plastic or glass, and it could be cut at 45° and metalized. The fibers would be placed in a tube, with an opening where the fiber is cut off. This section would also have to be stiffened as to not let the fibers bend. The source fiber could have a core size much less than the core of the fiber collecting the light. The use of carefully constructed fiber lenses could also be used to provide focusing of the emitted light [26].

If one assumes that it is possible to reflect a large amount of light at the probe tip, the performance of the fiber-to-fiber probe is governed by the amount of light transmitted and collected in the open part of the probe. This is essentially a coupling efficiency problem. With perfectly aligned fibers, this coupling efficiency may be large when the distance between the fibers is on the order of a few core diameters. For two equal fibers with core diameters of $100\ \mu\mathrm{m}$ facing each other, the coupling efficiency could be as high as 30% at a separation of $L \simeq 0.5\ \mathrm{mm}$ [26]. However, further increase of the separation would result in a drastically lowered coupling efficiency.

The fiber-to-fiber design can be made very compact, requiring little fluid volume. If the limited path length of the probe can be made acceptable, this design could be appropriate for in-vivo use. However, the manufacturing of this probe is more complicated than for the coaxial probe. Fiber alignment is crucial, and the design is also subject to losses due to light scattering when the path length is increased.

3.2.3 Closed cavities

A closed-cavity probe is based on a design where the fluid volume is kept in a cavity with highly reflective walls. Light passed into the cavity will be confined, increasing the possibility of interaction with the fluid. Some of the light will eventually be collected by a collection fiber. The main idea of this kind of design is to make the probe less sensitive to losses due to light scattering, as the scattered light is not removed from the sampling volume. A second idea is to increase the path length of the light, while retaining a small probe size. While the previously discussed designs have a relatively well defined path length, a closed cavity design may not. The path length in a multiple scattering and reflecting cavity will be replaced by a distribution of path lengths. A closed cavity may thus act as a multipass absorption cell, a cell in which the light travels across the cavity several times before being collected. If a pulse of light is emitted into such a cavity, the light would be detected at different times.

A closed-cavity probe cannot be completely closed, as peritoneal fluid would have to enter the probe from somewhere. Fluid dynamics is the major problem with such a design. Opening up the cavity to allow fluid to flow through the probe reduces the light confinement properties of the probe. A solution could be active fluid control, where the fluid is pumped in and out of the cavity. By moving to an active design, numerous possibilities of probe design emerge. There are examples of probes that combine fiber-optics with microfluidic flows in an in-vivo setting [27]. While it is possible to create a probe with active fluid control, the system quickly becomes more complex. However, this may not be entirely the case in the proposed CGM system. This system will eventually have to include a pump for insulin delivery to the peritoneal cavity. This pump could also be coupled to close-cavity probe with an integrated microfluidic channel.

3.3 Spherical cavity probe

A probe design based on a closed cavity has been chosen for further investigation. The cavity is spherical with source and collection fibers entering through a single opening port. The design principle is illustrated in figure 3.3. The light emitted by the collection fiber hits the sphere wall and may reflect multiple times before being collected by the collection fiber. The wall reflection could be diffuse in order to randomize the distribution of light inside the cavity and increase the path length.

The source and collection fibers coming into the cavity would be encased in a microfluidic tube. The space not taken up by the fibers could be used directly for pumping fluid in and out of the cavity. Another option is to add additional tubing for pumping of peritoneal fluid, but also for rinsing of the probe. This second tube could be used to flush the cavity with a biocompatible solution. Rinsing the cavity walls and fiber end faces could prevent degradation effects such as formation of biofilms. If possible, this would increase the lifetime of the probe.

This probe design is essentially a miniature integrating sphere mounted at the end of a set of fibers. The general integrating sphere has been analyzed rigorously [28], and the use of integrating spheres for measuring absorption coefficients of scattering fluids and gases has been investigated [29–31]. However, the sizes of the cavities used in these works are several orders of magnitude larger than the size of the cavity considered here. Here, a typical cavity would have an inner diameter of $1\ \mathrm{mm}$, yielding a sample volume of the order of $1\ \mu\mathrm{L}$.

Some design considerations can be learned from the discussion of the ideal integrating sphere in section 2.4. The amount of ports on the sphere wall should be minimized. Any port area that absorbs light, and is not a part of collection optics, will result in a reduced collec-

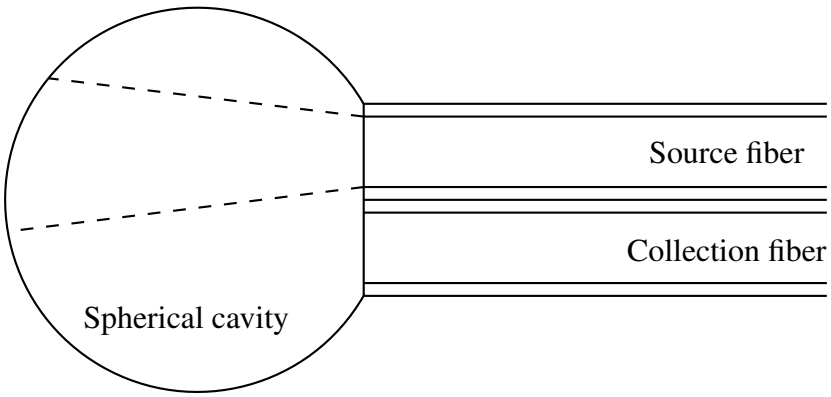

Figure 3.3: The basic design of a spherical cavity probe. The source and collection fibers enter the cavity through a port.

tion efficiency. A high reflectivity of the interior wall is crucial to confine the light and increase the path length. Increasing the sphere diameter results in longer path lengths, but also reduces the collection efficiency. For a given port fraction, the collection efficiency should increase linearly with increased core area of the collection fiber. Lastly, the numerical aperture NA of the collection fiber should be as large as possible as it is expected that the collection efficiency scales as NA^2.

An order of magnitude estimate of the collection efficiency of a closed-cavity probe may be acquired by considering the expression for the collection efficiency of an ideal integrating sphere in (2.72). Consider two equal fibers with core diameters of $100\ \mu\mathrm{m}$, cladding diameters of $125\ \mu\mathrm{m}$ and numerical apertures of 0.22. If these fibers enter a cavity of radius $0.5\ \mathrm{mm}$ through a circular port, the collection efficiency is on the order of 0.5% when the reflectivity of the cavity wall is approximately 93%. This may seem like a low number, but it is important to consider that the optical path length may be much larger than the size of the probe due to multiple reflections of the light within the cavity.

The response of the probe when filled with fluids of variable absorption and scattering coefficients is important. If the probe is to be used over a large wavelength range, which may be required for glucose prediction, it is evident that the attenuation coefficient may vary over several degrees of magnitude. In addition, the path length is not well defined, and the reflectivity of the internal wall will depend on wavelength. The spherical cavity probe may thus behave radically different than a more conventional probe.

Chapter 4

Modeling of a spherical cavity probe

This chapter introduces and details the model used to investigate the proposed spherical cavity probe. The aim of the modeling is to investigate some of the properties of the probe that may help to guide an eventual future design.

The chapter starts with an introduction to Monte Carlo techniques for propagation of photons in various media. Following this, attention will be given to the geometry of the modeled probe, the emitted intensity of a multimode fiber and how a photon interacts with boundaries in the probe. The process of estimating physical quantities is then detailed, along with examples of how parts of the model have been verified. Lastly, simulations are detailed.

4.1 Monte Carlo photon transport

Monte Carlo photon transport is a technique in which the interaction between light and media are modeled by tracing a statistical ensemble of what is here called photons. These photons move throughout a medium in a random fashion, and they are absorbed and scattered along the way. The movement of a photon is decided by the absorption and scattering coefficients of the medium, along with a PDF that models how photons are scattered. Estimates of physical quantities are done by recording events such as scattering, absorption and interactions with geometrical boundaries. The process is essentially based on counting events and averaging. This modeling technique is commonly used for investigating the propagation of radiation in turbid media like tissue [32].

4.1.1 Coordinate systems and definitions

The origin of the global coordinate system used in the model is in the center of the spherical cavity as shown in figure 4.1. The position of a photon inside the cavity is

$$\mathbf{r} = x\hat{\mathbf{x}} + y\hat{\mathbf{y}} + z\hat{\mathbf{z}} \tag{4.1}$$

The photon travels in a direction

$$\hat{\boldsymbol{\mu}} = \mu_x\hat{\mathbf{x}} + \mu_y\hat{\mathbf{y}} + \mu_z\hat{\mathbf{z}} \tag{4.2}$$

where the components of the direction are the directional cosines defined by

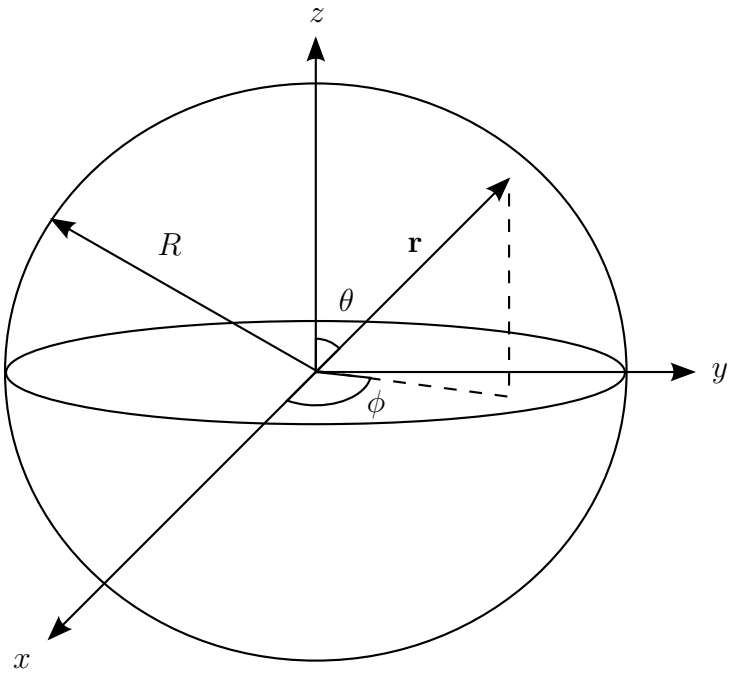

Figure 4.1: The coordinate system used in the modeling of a spherical cavity probe.

$$\begin{aligned} \mu_x &= \cos\phi \sin\theta \\ \mu_y &= \sin\phi \sin\theta \\ \mu_z &= \cos\theta \end{aligned} \tag{4.3}$$

Here ϕ is the azimuthal angle and θ is the polar angle. R is the radius of the cavity. When a photon is scattered or reflected, the scattering and reflection directions are first computed in a local coordinate system. The notation for positions in the local coordinate system is

$$\mathbf{r}' = x'\hat{\mathbf{x}}' + y'\hat{\mathbf{y}}' + z'\hat{\mathbf{z}}' \tag{4.4}$$

and the notation for directions is

$$\hat{\boldsymbol{\mu}}' = \mu_x'\hat{\mathbf{x}}' + \mu_y'\hat{\mathbf{y}}' + \mu_z'\hat{\mathbf{z}}' \tag{4.5}$$

where

$$\begin{aligned} \mu_x' &= \cos\phi' \sin\theta' \\ \mu_y' &= \sin\phi' \sin\theta' \\ \mu_z' &= \cos\theta' \end{aligned} \tag{4.6}$$

A photon is attributed a quantity w, which will be called the weight of the photon. In a turbid medium, it is more convenient to treat a photon as a collection of photons, a photon packet, that are traced at the same time. The weight of the collection of photons may be thought of as the number of photons in the photon packet. A weight of $w = 1$ is a full packet, while a weight of $w = 0$ is an empty packet. Tracing of photons in a turbid medium is thus not done in a quantum fashion. In the following a photon packet will simply be called a photon.

4.1.2 Rules of propagation

The basics steps of propagating a photon is as follows. First, a photon is given an initial position and direction. A step size is chosen, and the photon is moved to a new location. At this new location, a part of the photon is absorbed. After absorption, a new direction of propagation is chosen based on a scattering PDF. With a new direction, a new step size must be chosen, and this completes the loop. This procedure continues, and is only interrupted by collisions with boundaries and when the weight of the photon falls below a threshold. Details of the basic steps for propagation are given in the following. The procedures and methods follow closely what is done in [33].

Choosing a step size

For a medium with scattering coefficient α_s and absorption coefficient α_a, the CDF of the free path l of the photon is

$$F_l(l) = 1 - e^{-\alpha_t l} \tag{4.7}$$

where $\alpha_t = \alpha_a + \alpha_s$. The free path of the photon is the distance a photon will travel before it interacts with the medium. The PDF corresponding to (4.7) is

$$p_l(l) = \alpha_t e^{-\alpha_t l} \tag{4.8}$$

The mean free path $\langle l \rangle$ is

$$\langle l \rangle = \int_0^\infty l p_l(l) dl = \frac{1}{\alpha_t} \tag{4.9}$$

A medium with increased turbidity will thus result in a photon propagating a shorter distance before it interacts with the medium. The step size s of the photon is taken to be equal to the free path, i.e. $s = l$. By using the inverse sampling method, sampling of the step size of the photon is done by

$$s = -\frac{1}{\alpha_t} \ln(1 - \xi_s) \tag{4.10}$$

where ξ_s is a random number between 0 and 1, generated by a PRNG.

Moving the photon

After a step size has been chosen, the photon is ready to move. The coordinates of the photon is updated by

$$\begin{aligned} x &\to x + s\mu_x \\ y &\to y + s\mu_y \\ z &\to z + s\mu_z \end{aligned} \tag{4.11}$$

If the new position is such that the photon has crossed a boundary, the step size is split into two

$$s = s_- + s_+ \tag{4.12}$$

where s_- is the distance from the original point to the boundary, and s_+ is the remaining distance the photon will travel if it survives the interaction with the boundary.

Absorption

After the photon has been moved, a part of it must be absorbed by the media. The weight absorbed by the media at the current position is

$$\Delta w = w\frac{\alpha_a}{\alpha_t} \tag{4.13}$$

and the new photon weight is updated by

$$w \to w - \Delta w \tag{4.14}$$

If the media is non-absorbing, that is $\alpha_a = 0$, the weight is always $w = 1$. In this case the photon weight is only lost through interactions with the boundary. If $\alpha_s = 0$ the media is non-scattering, and only one step size is sampled. In this scenario the total photon weight is deposited only once.

Continued propagation of a photon with a minuscule weight yields little information, and so the photon must be terminated at some point. If the photon weight falls below a threshold w_t, the photon is given a $1/p$ chance to survive. A random number is drawn, and if it is less than $1/p$ the photon weight is updated by

$$w \to wp \tag{4.15}$$

If the number is larger than $1/p$ the photon is terminated.

Scattering

A photon is scattered by selecting a new direction $\hat{\boldsymbol{\mu}}$ based on a scattering PDF. The local coordinate system is such that

$$\hat{\mathbf{z}}' = \hat{\boldsymbol{\mu}} \tag{4.16}$$

The $\hat{\mathbf{x}}'$ and $\hat{\mathbf{y}}'$ unit vectors are in the plane normal to $\hat{\mathbf{z}}'$. The Henyey-Greenstein scattering PDF [34] is here used to model scattering due to its simplicity. This distribution can range from being backscattering to isotropic to forward scattering with a single parameter g, which will be called the anisotropy factor. The distribution is rotationally symmetric, and is defined by

$$p(\theta') = \frac{1}{4\pi}\frac{1-g^2}{(1+g^2-2g\cos\theta')^{3/2}} \tag{4.17}$$

It can be shown that the anisotropy factor is the average cosine of the scattering angle

$$g = \langle\cos\theta'\rangle \tag{4.18}$$

Sampling of the scattering angle θ' is done by

$$\cos\theta' = \mu'_z = \frac{1}{2g}\left[1+g^2-\left(\frac{1-g^2}{1+g-2g\xi_{\theta'}}\right)^2\right], \quad g > 0 \tag{4.19}$$

where $\xi_{\theta'}$ is a random number of uniform distribution. As the scattering is rotationally symmetric around the z' - axis, the azimuthal scattering angle ϕ' is set to

$$\phi' = 2\pi\xi_{\phi'} \tag{4.20}$$

where $\xi_{\phi'}$ is a random number of uniform distribution. The directional cosines of the new direction in the global coordinate system are

$$\begin{aligned}
\mu_x &= \frac{\sin\theta'}{\sqrt{1-\mu_{z_0}^2}}\left(\mu_{x_0}\mu_{z_0}\cos\phi' - \mu_{y_0}\sin\phi'\right) + \mu_{x_0}\cos\theta' \\
\mu_y &= \frac{\sin\theta'}{\sqrt{1-\mu_{z_0}^2}}\left(\mu_{y_0}\mu_{z_0}\cos\phi' + \mu_{x_0}\sin\phi'\right) + \mu_{y_0}\cos\theta' \\
\mu_z &= -\sin\theta'\cos\phi'\sqrt{1-\mu_{z_0}^2} + \mu_{z_0}\cos\theta'
\end{aligned} \tag{4.21}$$

where μ_{x_0}, μ_{y_0} and μ_{z_0} are the directional cosines prior to the scattering event.

4.2 Probe and fiber geometry

Figure 4.2 shows how the fibers enter the modeled cavity.

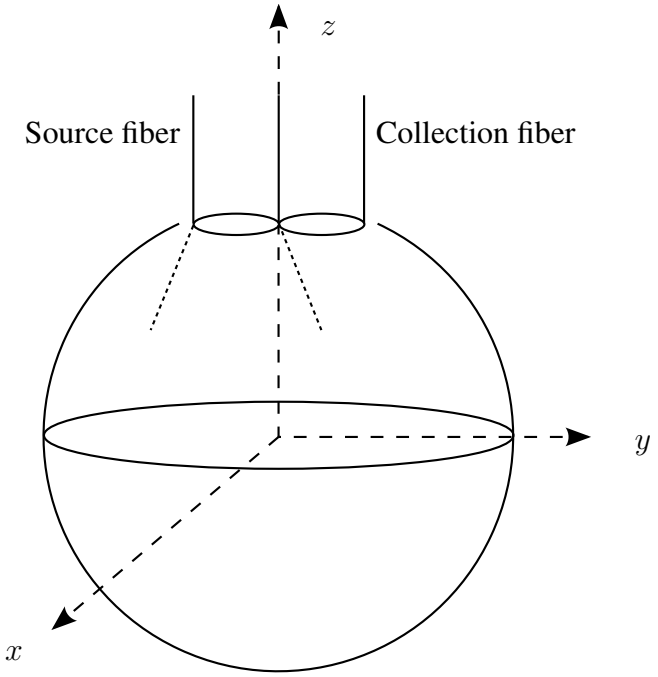

Figure 4.2: The geometry of the cavity with fibers inserted through an entrance port.

The fibers are inserted into the cavity through a circular entrance port. The coordinate of the center of the circular port is

$$\mathbf{r_c} = z_e\hat{\mathbf{z}} = \sqrt{R^2 - r_e^2}\hat{\mathbf{z}} \tag{4.22}$$

where r_e is the radius of the entrance port. Two fibers, a source fiber and a collection fiber, are placed in the entrance port such that their distal ends are located at $z = z_e$. A cross section of the entrance port with the geometry of the fibers is shown in figure 4.3. a_1 and a_2 are the core and cladding radii the source fiber, while b_1 and b_2 are the core and cladding radii of the collection fiber. All simulations have been done with the source and collection fiber being equal

in size. A common cladding radius of $a_2 = b_2 = 62.5$ µm was selected. The core radii were set to $a_1 = b_1 = 52.5$ µm. The size of the entrance port was set to $r_e = 2a_2 = 2b_2 = 125$ µm, yielding the geometry shown in figure 4.4.

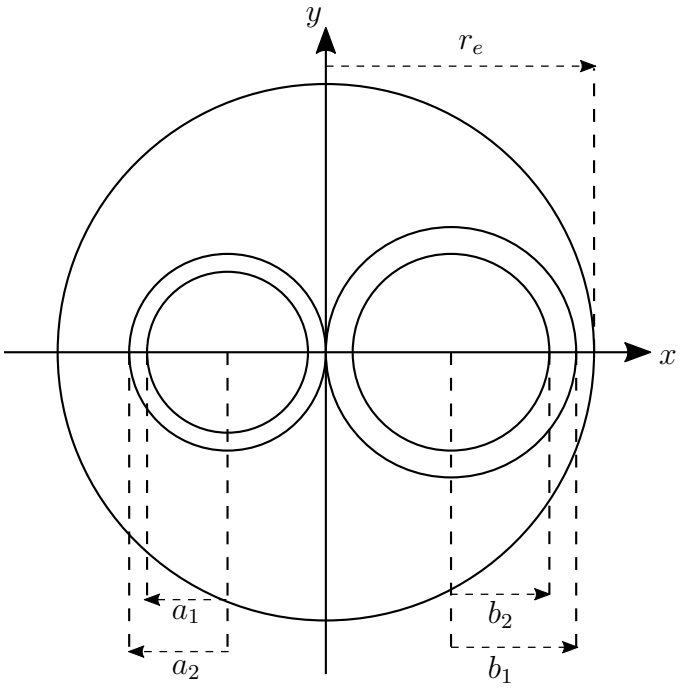

Figure 4.3: A cross section of the circular entrance port at $z = z_e$. The radius of the port is r_e. The fiber to the left is the source fiber, while the fiber to the right is the collection fiber. The core and cladding radii of the source fiber are a_1 and a_2, respectively. The core and cladding radii of the collection fiber are b_1 and b_2, respectively.

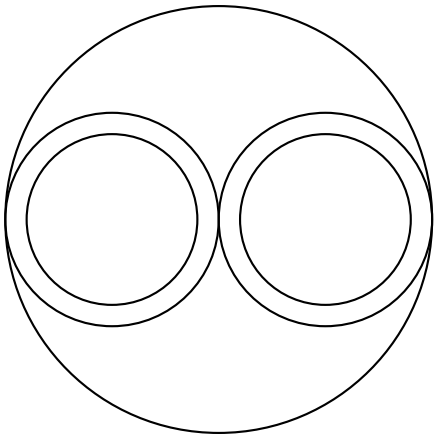

Figure 4.4: The fiber geometry used in the majority of the simulations. $a_1 = b_1 = 52.5$ µm, $a_2 = b_2 = 62.5$ µm and $r_e = 2b_1 = 125$ µm.

4.3 Fiber output intensity

The distribution of light emitted by a multimode fiber is in general dependent on the distribution of excited modes. As the number of modes may be extremely large, a model of the emitted light quickly becomes complex. A simple model is here considered. Basically, it is assumed that each mode carries the same amount of energy. There is equal amounts of energy propagating in every angle. Such a situation might be similar to what one obtains when a multimode fiber is overfilled by a source [35]. The emitted light is obtained by selecting source points uniformly on the core are of the fiber, and emitting light in directions that are restricted by the numerical aperture of the fiber. The concept is shown in figure 4.5.

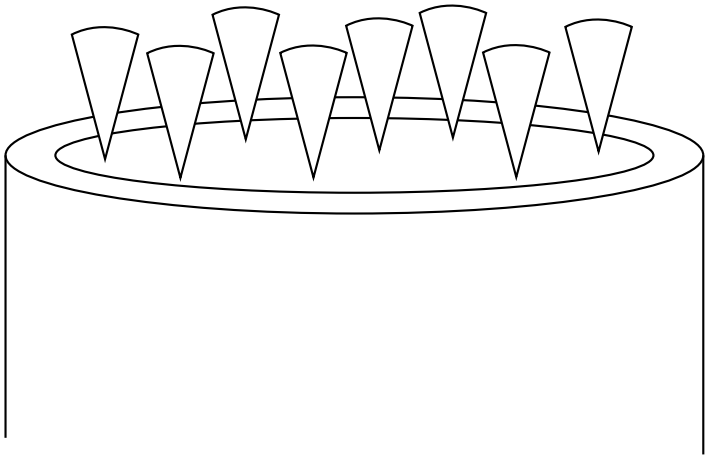

Figure 4.5: The principle used for generating the output light distribution of a MMF. Source points are generated uniformly on the core area, and directions are generated within solid angles confined by the numerical aperture of the MMF.

A source point is defined as

$$\mathbf{r_s} = x_s\hat{\mathbf{x}} + y_s\hat{\mathbf{y}} + z_e\hat{\mathbf{z}} \tag{4.23}$$

where

$$x_s^2 + y_s^2 \leq a_1^2 \tag{4.24}$$

Selecting source points that are distributed uniformly on the core area of the fiber is done by a rejection method. Two random numbers of uniform distribution ξ_x and ξ_y, are generated, and the coordinates of the source point are set to

$$\begin{aligned} x_s &= a_1(2\xi_x - 1) \\ y_s &= a_1(2\xi_y - 1) \end{aligned} \tag{4.25}$$

If $r_s > a_1$ the source point is rejected, and a new one is generated. This goes on until a valid source point is obtained. The probability that a selected source point is on the core area is $\pi/4 \approx 0.79$, which is large enough to quickly yield a desired source point. The distribution of light emitted by the fiber is assumed to only depend on the polar angle θ, and so the azimuthal angle of the direction of an emitted photon is set to

$$\phi = 2\pi\xi_\phi \tag{4.26}$$

where ξ_ϕ is a random number of uniform distribution. The polar angle must be sampled such that the number of photons emitted per unit solid angle is constant. This is equivalent to picking points on the unit sphere, under the constraint that $\theta < \theta_0$. Here θ_0 is the exit angle of the fiber as defined in (2.48). Using a rejection method will in this case be slow, and one must sample from an explicit distribution. The desired result is achieved by sampling $\cos\theta$ uniformly in the range $[\cos\theta_0, 1]$

$$\cos\theta = \cos\theta_0 + (1 - \cos\theta_0)\xi_\theta \tag{4.27}$$

Here ξ_θ is a random number of uniform distribution. The direction of a photon emitted from a source point $\mathbf{r_s}$ is thus

$$\begin{aligned} \mu_x &= \cos 2\pi\xi_\phi \sqrt{1-\mu_z^2} \\ \mu_y &= \sin 2\pi\xi_\phi \sqrt{1-\mu_z^2} \\ \mu_z &= -\left(\cos\theta_0 + (1-\cos\theta_0)\xi_\theta\right) \end{aligned} \tag{4.28}$$

4.4 Reflection and transmission at cavity walls

When a photon hits the walls of the sphere, it can either be transmitted or reflected. The reflectivity of the wall is ρ, which is here assumed to be independent of incident direction. The values of ρ range from 0 to 1, where $\rho = 0$ means that nothing is reflected, and $\rho = 1$ means that everything is reflected. Determining if the photon is reflected or not is done by first sampling a number ξ_ρ. If $\xi_\rho \leq \rho$ the photon is reflected. If the photon is not reflected, it is transmitted through the boundary, and it is no longer traced.

The local coordinate system at a point $\mathbf{r}$ on the sphere wall is defined by

$$\begin{aligned} \hat{\mathbf{x}}' &= -\hat{\boldsymbol{\theta}} = -\cos\phi\cos\theta\hat{\mathbf{x}} - \sin\phi\cos\theta\hat{\mathbf{y}} + \sin\theta\hat{\mathbf{z}} \\ \hat{\mathbf{y}}' &= \hat{\boldsymbol{\phi}} = -\sin\phi\hat{\mathbf{x}} + \cos\phi\hat{\mathbf{y}} \\ \hat{\mathbf{z}}' &= -\hat{\mathbf{r}} = -\cos\phi\sin\theta\hat{\mathbf{x}} - \sin\phi\sin\theta\hat{\mathbf{y}} - \cos\theta\hat{\mathbf{z}} \end{aligned} \tag{4.29}$$

The local reflection direction $\hat{\boldsymbol{\mu}}'$ is computed in the local coordinates, and transformed into the global coordinates by

$$\begin{aligned} \mu_x &= \mu_x'\hat{\mathbf{x}}'\cdot\hat{\mathbf{x}} + \mu_y'\hat{\mathbf{y}}'\cdot\hat{\mathbf{x}} + \mu_y'\hat{\mathbf{z}}'\cdot\hat{\mathbf{x}} \\ \mu_y &= \mu_x'\hat{\mathbf{x}}'\cdot\hat{\mathbf{y}} + \mu_y'\hat{\mathbf{y}}'\cdot\hat{\mathbf{y}} + \mu_y'\hat{\mathbf{z}}'\cdot\hat{\mathbf{y}} \\ \mu_z &= \mu_x'\hat{\mathbf{x}}'\cdot\hat{\mathbf{z}} + \mu_y'\hat{\mathbf{y}}'\cdot\hat{\mathbf{z}} + \mu_y'\hat{\mathbf{z}}'\cdot\hat{\mathbf{z}} \end{aligned} \tag{4.30}$$

The sphere walls are assumed to be Lambertian. From (2.39) one has that the flux per surface area, emitted into all angles that are less than θ', is

$$\begin{aligned} \frac{d\Phi(\theta')}{dA} &= 2\pi L_0 \int_0^{\theta'} \cos\gamma\sin\gamma d\gamma \\ &= \pi L_0 \sin^2\theta' \end{aligned} \tag{4.31}$$

Normalizing (4.31) to the total flux emitted by the source area $d\Phi$ results in

$$\frac{d\Phi(\theta)}{d\Phi} = F(\theta) = \sin^2\theta \tag{4.32}$$

If a photon is to be reflected from a diffuse, Lambertian surface, $F(\theta')$ is interpreted as the CDF of the reflection angle θ' [36]. Sampling of θ' is then done by

$$\theta' = \arcsin\sqrt{\xi_{\theta'}} \tag{4.33}$$

where $\xi_{\theta'}$ is a random number of uniform distribution. The directional cosine in the z'-direction is thus

$$\mu'_z = \cos\left[\arcsin\sqrt{\xi_{\theta'}}\right] = \sqrt{1-\xi_{\theta'}} \tag{4.34}$$

Ideal diffuse reflection is rotationally symmetric about the z'-axis, and so the azimuthal angle is sampled as in (4.26). The directional cosines for diffuse reflection are then

$$\begin{aligned} \mu'_x &= \cos 2\pi\xi_{\phi'}\sqrt{\xi_{\theta'}} \\ \mu'_y &= \sin 2\pi\xi_{\phi'}\sqrt{\xi_{\theta'}} \\ \mu'_z &= \sqrt{1-\xi_{\theta'}} \end{aligned} \tag{4.35}$$

4.5 Physical quantities

The amount of photons emitted from the source fiber is N, which is equivalent to a total photon weight of W_{tot}. The amount of photon weight collected by the collection fiber is W_c, and the amount of weight lost to the entrance port, walls and interior media is W_e, W_w and W_i, respectively. Conservation of photons, or probability, requires

$$W_{tot} = W_c + W_e + W_w + W_i \tag{4.36}$$

The fraction of weight collected by the collection fiber is the collection efficiency

$$\epsilon_c = \frac{W_c}{W_{tot}} \tag{4.37}$$

The collection efficiency ϵ_c is the amount of light collected by the collection fiber relative to the total amount of light emitted into the cavity. One can similarly define the fraction of weight lost to the entrance port, walls and interior media as

$$\begin{aligned} \epsilon_e &= \frac{W_e}{W_{tot}} \\ \epsilon_w &= \frac{W_w}{W_{tot}} \\ \epsilon_i &= \frac{W_i}{W_{tot}} \end{aligned} \tag{4.38}$$

This turns (4.36) into

$$1 = \epsilon_c + \epsilon_e + \epsilon_w + \epsilon_i \tag{4.39}$$

A photon is collected if two criteria are met. First, it has to hit the core of the collection fiber. Second, it must have a propagation direction that lies within the angles accepted by the

collection fiber. If these conditions are met, the weight of the photon is added to W_c. If the photon travels past the plane at $z = z_e$, and one of these conditions are not met, it is considered to be lost to the entrance port. In this case the photon weight is added to W_e. Similarly, the weight W_w is updated if the photon is transmitted through the sphere walls, and W_i is updated if the photon is absorbed in the interior of the sphere.

The path length travelled by photon number n that is collected by the collection fiber is defined as

$$L_n = \sum_k s_k \tag{4.40}$$

where the summation is done over all step sizes s_k. To get reliable statistics, N photons must be launched into the sphere many times, followed by an averaging process. The number of realizations of the system is M. That is, N photons are launched into the sphere M times. The path length is assigned a PDF $p_L(L)$. The mean of this distribution, at realization number m, is estimated by

$$\langle L_m \rangle = \frac{1}{W_c} \sum_{n=1}^{N_c} w_n L_n \tag{4.41}$$

where

$$W_c = \sum_{n=1}^{N_c} w_n \tag{4.42}$$

Here the summation is done over all the N_c collected photons, and w_n is the weight of the n'th collected photon. The sample standard deviation at the m'th realization of the system, σ_{L_m}, is defined by

$$\sigma_{L_m}^2 = \frac{1}{W_c} \frac{N_c}{N_c - 1} \sum_{n=1}^{N_c} w_n (L_n - \langle L_n \rangle)^2 \tag{4.43}$$

After M realizations, the sample mean of the path length is defined as

$$\langle L \rangle = \frac{1}{M} \sum_{m=1}^{M} \langle L_m \rangle \tag{4.44}$$

and the mean of the sample standard deviation, $\langle \sigma_L \rangle$, is defined by

$$\langle \sigma_L \rangle = \frac{1}{M} \sum_{m=1}^{M} \sigma_{L_m} \tag{4.45}$$

The quantities defined in (4.37) and (4.38) are also averaged M times. For an absorbing or turbid medium, the transmission of the probe is defined as

$$T = \frac{\epsilon_c(\alpha_t)}{\epsilon_c(0)} \tag{4.46}$$

The transmission is thus referenced to an empty cavity. The absorbance is, in accordance with (2.57), defined as

$$A = -\ln T \tag{4.47}$$

4.6 Verification of tracing algorithm

The tracing algorithm has been verified to work by applying the algorithm to simpler systems, and comparing the results to known analytical solutions. The most simple system is a perfect hollow sphere. If one considers a photon bouncing around inside this cavity, it can be shown that the mean path length of the photon is [37]

$$\langle L \rangle_1 = \frac{4R}{3} \frac{1}{1-\rho} \tag{4.48}$$

For a hollow sphere filled with an absorbing medium with absorption coefficient α_a, the mean path length can be shown to be [37]

$$\langle L \rangle_2 = \frac{1}{\alpha_a} \frac{1-P_s}{1-\rho P_s} \tag{4.49}$$

where

$$P_s = \frac{1}{2\alpha_a^2 R^2} \left[1 - (1 + 2\alpha_a R) e^{-2\alpha_a R}\right] \tag{4.50}$$

(4.48) and (4.49) are easily reproduced by the model.

The tracing algorithm was also verified by considering limiting situations with the fibers connected to the spherical cavity. If one lets the numerical aperture of the collection fiber approach 1, every photon incident on the core of the collection fiber is collected. When the ratio of sphere radius to entrance port radius becomes large, $R/r_e \gg 1$, the distribution of light within the cavity should be close to uniform. By letting $\rho \to 1$, the collection efficiency should in this situation be equal to the fraction of area taken up by the core of the collection fiber, relative to the total entrance port area

$$\epsilon_c \to \frac{A_{core}}{A_e} = \left(\frac{b_1}{r_e}\right)^2 \tag{4.51}$$

This situation is reproducible with the model.

4.7 Simulations

The simulations were focused on how the estimated physical quantities vary in the parameter space. The probe was investigated with four different kinds of interior media. These media are defined by their scattering and absorption coefficients, and are listed in table 4.1

Table 4.1: The table lists the types of media that were used in simulations.

Medium	α_a	α_s
Transparent	$= 0$	$= 0$
Absorbing	$\neq 0$	$= 0$
Scattering	$= 0$	$\neq 0$
Turbid	$\neq 0$	$\neq 0$

All simulations were, unless stated otherwise, done with the number of photons set to $N = 10^6$ and the number of system realizations set to $M = 10^2$. The weight threshold was set to

$w_t = 10^{-5}$, and the survival rate was set to $1/p = 0.1$. The diameter $D = 2R$ of the cavity was varied only for the transparent medium, while it was kept at $D = 1\ \mathrm{mm}$ for the rest of the media. The geometrical properties of the fibers and entrance port were as described in section 4.2, except for simulations that were to be compared to experimental data. The numerical apertures of the fibers were set to $\mathrm{NA}_0 = 0.22$, unless stated otherwise. The refractive index of the interior medium was always set to $n_0 = 1$. A general medium will have a refractive index $n > 1$, but this may be incorporated in a rescaled NA. If the medium had refractive index n, the simulations were done as if the numerical aperture of the fibers were

$$\mathrm{NA}(n) = \mathrm{NA}_0 n = 0.22n \tag{4.52}$$

The reflectivity ρ of the sphere walls were varied for most simulations in order to highlight how a wavelength dependency of ρ changes the properties of the probe.

Chapter 5

Experimental

This chapter details parts of the experimental work that has been done. The design and fabrication of early prototypes of spherical cavities will be presented. The preparation of optical fibers for measurements will then be detailed. Following this, the experimental setups and relevant instrumentation will be presented. Details on the measurements performed with the fabricated cavities are given last.

5.1 Spherical cavity prototypes

Spherical cavities with diameters ranging from $D = 0.75$ mm to $D = 1.75$ mm have been designed and fabricated. A cross section of the design of the cavities is shown in figure 5.1. The cavities were essentially two half spheres that were aligned and clamped together. One of the half spheres had an entrance port for fiber insertion. The larger hole leading to the entrance port was designed to fit standard FC fiber ferrules with outer diameters of $D_f = 2.5$ mm. The distance between the entrance port to the ferrule hole was $h = 0.425$ mm for all cavity sizes, and the diameter of the entrance port was $D_e = 2r_e = 0.5$ mm. The cavities were hollowed out on two plates, and alignment was achieved by four locating pins. The thickness of the plates were $H = 6$ mm. Four screws were used to clamp the plates together.

Eight cavities were placed next to each other. Five cavities were fully closed, while three cavities had an additional port oriented perpendicular to the entrance port. The diameters of the closed cavities were $D = 0.75, 1.0, 1.25, 1.50, 1.75$ mm, while the diameters of the cavities with the additional port were $D = 0.75, 1.25, 1.75$. This additional port were made of two half-cylindrical grooves, with a resulting diameter of 0.4 mm, and was designed to fit an insulin syringe. All the cavities were made such that a single FC ferrule holding the source and collection fibers could be used for the cavities, without the need for coaxial realignment. Figure 5.2 shows the principle of how fibers were inserted into the cavities.

The materials used in fabrication of the cavities were aluminium and polytetrafluoroethylene (PTFE). The type of PTFE used (Zenith Polymer, Sphereoptics) has diffuse properties, and it is quoted to have a reflectivity of $\rho > 99$ in the wavelength range $350 - 1500$ nm and $\rho > 95\%$ in the range $1500 - 2500$ nm. The material is porous, and a mean pore size of 6 μm is quoted. The required thickness of the material to achieve the quoted reflectivities are not detailed. After comparing a few slices of the material of different thickness, the required thickness was assumed to be well above 2 mm. The cavities were spaced out on the plates

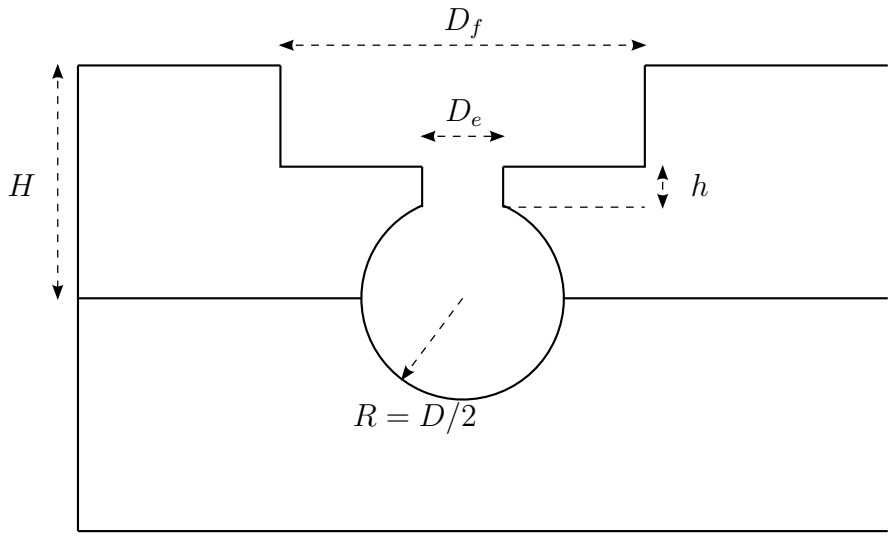

Figure 5.1: A cross section of the designed and fabricated cavities. $D_f = 2.5$ mm, $D_e = 0.5$ mm, $H = 6$ mm and $h = 0.425$ mm. The sphere diameters D varied in size.

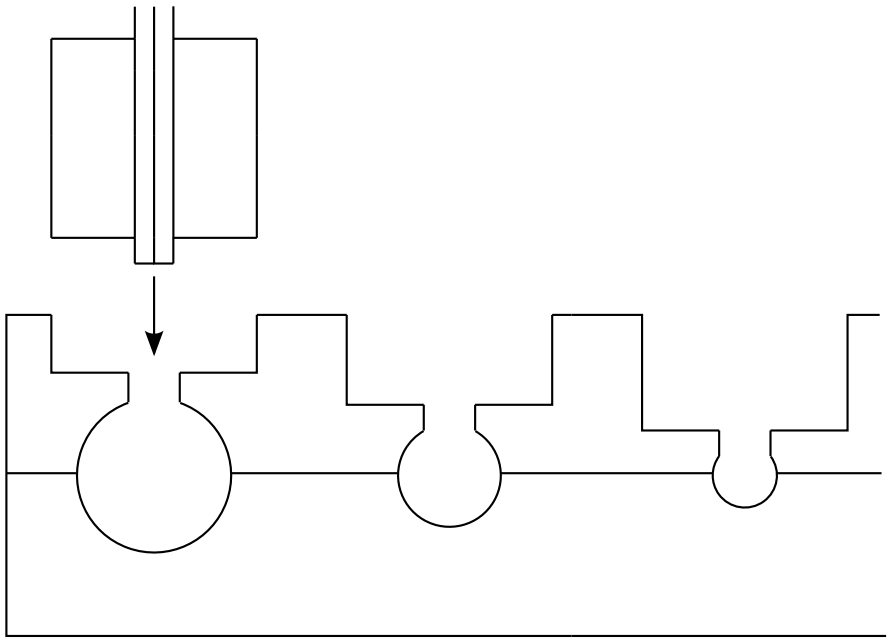

Figure 5.2: A ferrule holding the source and collection fiber being inserted into a cavity. The ferrule was lowered until it came in contact with the upper plate.

such that they were surrounded by a large amount of material, with exception of the the region around the entrance port.

Fabrication of the cavities were carried out by the Fine Mechanical Workshop at the Faculty of Natural Sciences and Technology at NTNU. The plates made of PTFE are shown in figure 5.3. Difficulties in fabrication of the PTFE cavities arose because the material was soft and flexible. Clamping of the two plates was a particular issue, as the material tended to bend.

Figure 5.3: The image shows the cavities made of PTFE.

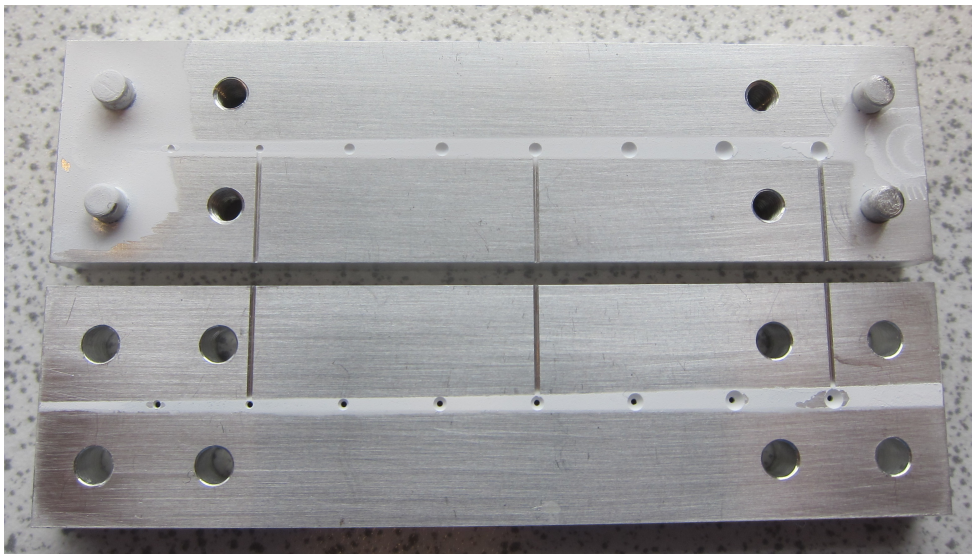

Figure 5.4: The image shows the cavities made of aluminium after they were coated with diffuse paint.

The cavities made of aluminium were only used for a few measurements before they were coated with a white diffuse paint (Labsphere 6080). The paint is barium sulfate based and dissolves in water. The quoted reflectivity of the paint around the wavelength $\lambda = 1550$ is $\rho \approx 90\%$. The recommended thickness of the paint is of order 0.5 mm, but such a thickness would be too large for the cavities. A much thinner coating was applied, and it is assumed that this was enough to provide diffuse reflection and that one could rely on the underlying aluminium for a high reflectivity. The paint was applied by use of an airbrush. The results are shown in figure 5.4.

5.2 Fiber preparation

The cavities were tested with several fiber configurations. All fiber configurations had one source fiber and one collection fiber, with ends attached to standard FC ferrules. Figure 5.5 shows the geometry. Two types of multimode step index silica fibers were used. Details of the fibers are listed in table 5.1.

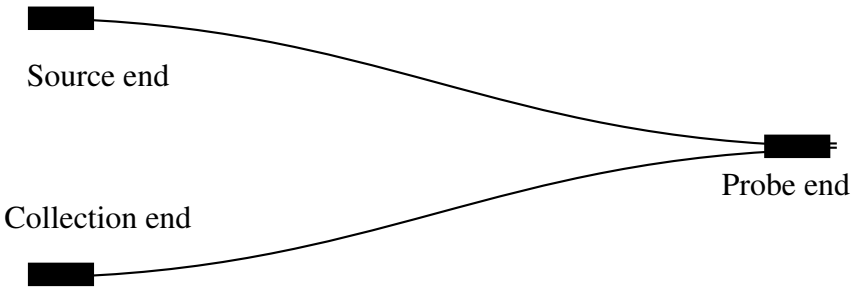

Figure 5.5: The source fiber and the collection fiber with ends attached to ferrules.

Table 5.1: The table lists the properties of the optical fibers used in the experiments.

Fiber number	Core diameter [μm]	Cladding diameter [μm]	NA
1	105 ± 2.1	125 ± 1	0.22 ± 0.02
2	200 ± 4	220 ± 2	0.22 ± 0.02

The source fibers were, in all cases, the 105 μm core fibers (Thorlabs FG105LCA). These fibers were cleaved with a fiber cleaver. The cleaver, shown in figure 5.6, locked the fiber in place and applied longitudinal tension. A blade was then moved towards the fiber, and upon contact the fiber split in two. The result was a clean, flat cut, perpendicular to the longitudinal axis of the fiber.

The fiber cleaver only accepted fibers with a standard cladding size of 125 μm, and so the thicker 200 μm core fibers (Thorlabs FG200LEA) fibers were polished. The polishing process was initiated with the fibers being temporarily glued to a FC ferrule with standard nail polish. Excess fiber was cut away, and the fiber was polished down until it was flush with the ferrule. The polishing was done manually, with polishing paper of grit sizes 30 μm (Thorlabs LF30D), 3 μm (Thorlabs LF3D) and 1 μm (Thorlabs LF1D). If the polished fiber was to be inserted into a cavity, the polished fiber and the ferrule was soaked in acetone until the nail polish had dissolved. The fiber was then carefully removed from the ferrule.

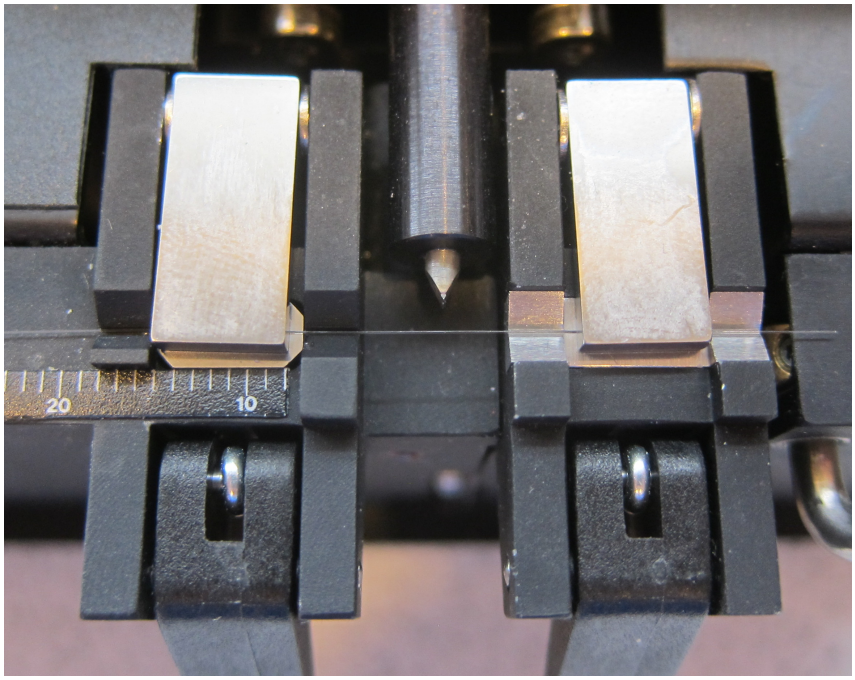

Figure 5.6: The picture shows the fiber cleaver used for preparing the source fibers. Tension was applied to the fiber, and the blade, seen in the center of the image, was moved towards the fiber. Upon contact the fiber was cut in two.

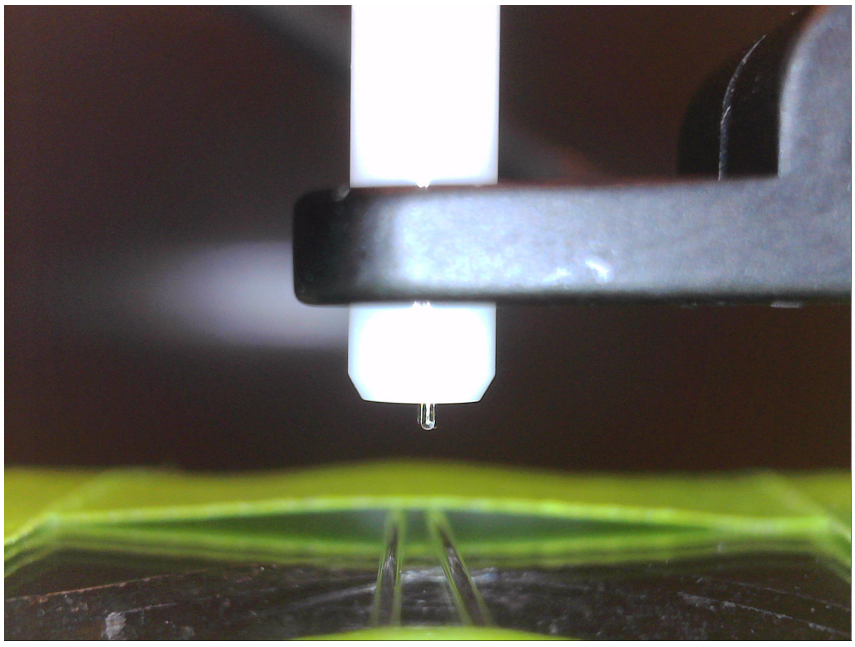

Figure 5.7: The picture shows the spacer used for protruding the fibers out of ferrules. The ferrule, in white, was clamped by a ferrule holder and lowered down towards the spacer by use of an xyz-stage.

The fibers that were to be inserted into the cavities had to protrude $0.425\ \mathrm{mm}$ out from the probe ferrule in order to be flush with the cavity wall. A spacer was created by attaching two optical fibers with cladding diameters of $425 \pm 10\ \mu\mathrm{m}$ to a glass slide. A ferrule holder was

fastened to an xyz-stage, clasping a ferrule. The source and collection fibers were run through the ferrule. A microscope was directed towards the spacer, and the ferrule was lowered towards the glass. Right before the ferrule hit the large core fibers, nail polish was applied to the top of the ferrule. The fibers were then pushed gently through the ferrule until they hit the glass slide. The ferrule was then lowered down until it hit the large core fibers, and the nail polish was allowed to dry. An image of the ferrule and spacer is shown in figure 5.7.

In addition to the flat ended fibers, two fibers with hemispherical ends were prepared. These fibers were of the same type as the ones presented in table 5.1. The hemispherical ended fibers were prepared as they might have a higher light collection capability, i.e larger numerical aperture, than the flat ended fibers [38–40]. Images of the hemispherical fibers with accompanying source fibers attached to ferrules are shown in figures 5.8 and 5.9. A list of the different fiber configurations are given in table 5.2. The bore diameters of the ferrules were $270\ \mu\mathrm{m}$ for fiber configuration A and C, and $440\ \mu\mathrm{m}$ for fiber configurations B and D. The length of all fibers were approximately $1\ \mathrm{m}$.

Table 5.2: The table lists the fiber configurations used in the experiments.

Configuration	Source fiber	Collection fiber	Collection surface
A	1	1	Flat
B	1	2	Flat
C	1	1	Hemispherical
D	1	2	Hemispherical

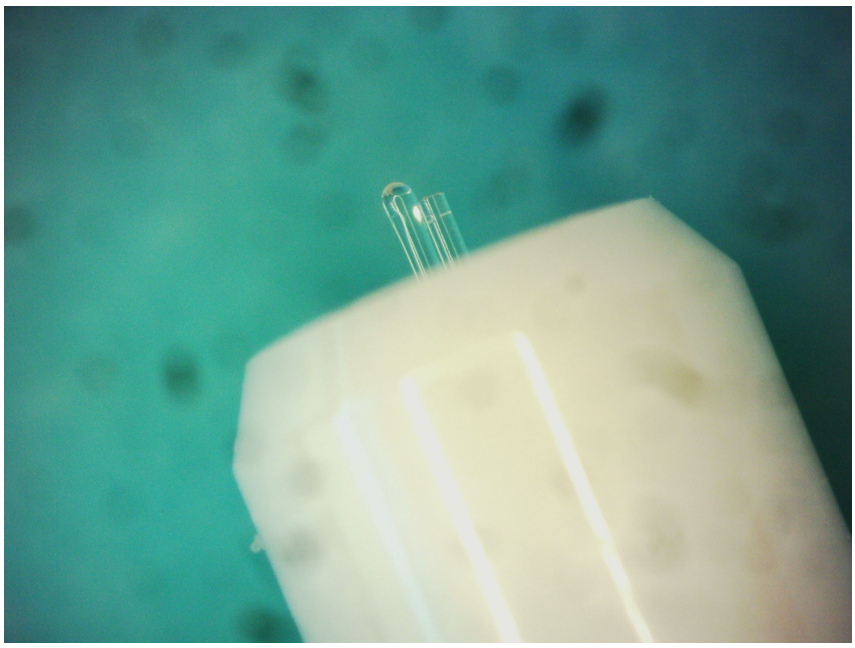

Figure 5.8: The image shows the hemispherical fiber of core diameter $105\ \mu\mathrm{m}$ next to the source fiber of core diameter $105\ \mu\mathrm{m}$, fastened to a ferrule.

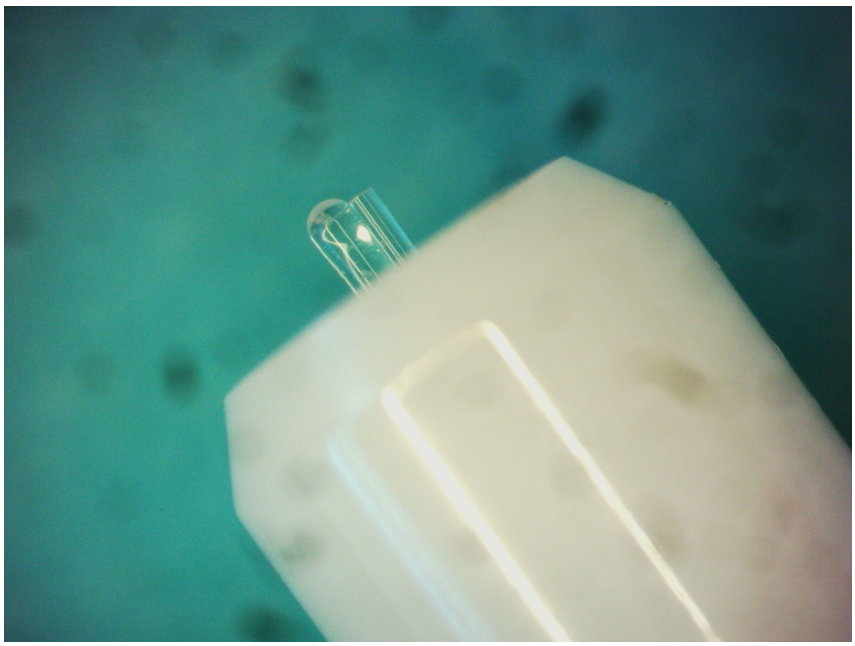

Figure 5.9: The image shows the hemispherical fiber of core diameter 200 µm next to the source fiber of core diameter 105 µm, fastened to a ferrule.

5.3 Experimental setup and instruments

Two experimental setups were prepared and used. The first setup was based on a coherent source, while the second was based on a broadband source. Details of the setups are given in the following.

5.3.1 Coherent setup

A representation of the coherent setup is shown in figure 5.10. The source was a fiber-coupled laser diode (Qphotonics QFLD-1550-10S) operating at a center wavelength of $\lambda = 1550$ nm. A sinusoidal reference signal was generated by the internal oscillator of a lock-in amplifier (Princeton Applied Research model 5210, lock-in 1 in figure 5.10). This signal was provided to a laser diode driver (Light Control Instruments 502) and to a second lock-in amplifier (Stanford Research Systems SR510, lock-in 2 in figure 5.10). The reference signal was driven at a frequency of 1.859 kHz. The laser diode driver modulated the output of the diode at the reference frequency. A modulation current of 44 mA yielded an approximate optical output power of 5 mW.

A single mode fiber (Thorlabs P1-SMF28E-FC-1, SMF2 in figure 5.10) was coupled to the laser fiber (SMF1 in figure 5.10) by use of a FC mating sleeve (Thorlabs ADAF1). The 105 µm core source fibers were connected to this single mode fiber in a similar fashion. This was done to prevent potential damage to the laser fiber due to improper surface finishes of the cleaved 105 µm fibers.

The detector was a germanium photodetector (Thorlabs PDA50B-EC) sensitive to light in the wavelength range $800 - 1800$ nm. The detector had an integrated amplifier with adjustable voltage amplifications in the range of $10 - 70$ dB. The detector had threaded mounts that accepted standard FC ferrules. Fibers were thus inserted directly into the detector, without any

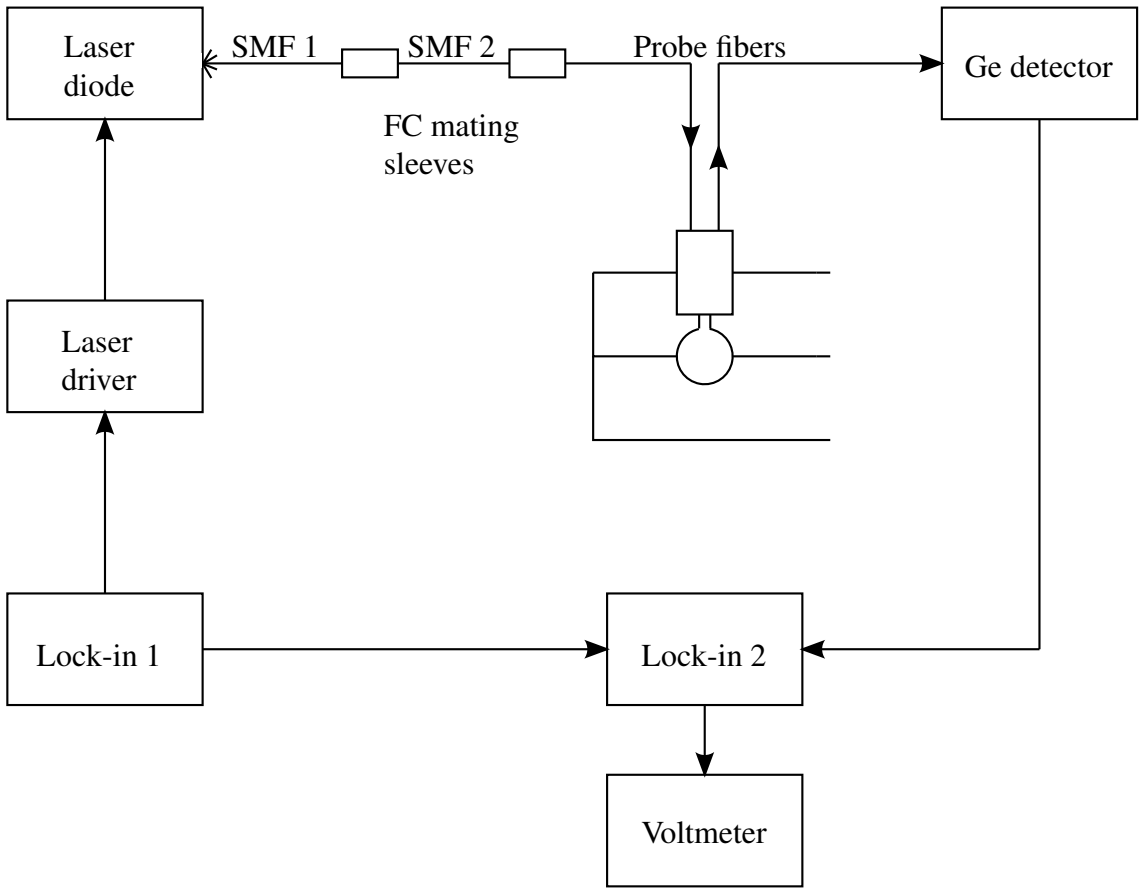

Figure 5.10: A representation of the coherent experimental setup.

need for alignment. The output of the detector was connected to the second lock-in amplifier. The full scale range of the second lock-in amplifier was $1 - 10$ V, and the analog output was digitized by a voltmeter (Fluke 45).

5.3.2 Broadband setup

A modified spectrophotometer (Zeiss M4 QIII) was used for spectral measurements. The spectrophotometer had a white light source capable of covering the wavelength range of the germanium detector and a monochromator for wavelength separation. The center wavelength and the bandwidth of the emitted light could be adjusted by mechanical rotation of two disks on the exterior of the spectrometer. A stepper motor was connected to the disk that controlled the center wavelength. This stepper motor was driven by a microcontroller (Arduino Uno).

The output beam of the spectrophotometer was modulated at a frequency of 500 Hz by an optical chopper (Thorlabs MC1F10). The chopper was controlled by a chopper driver (Thorlabs MC2000). The beam was focused into a 550 µm core multimode fiber (Thorlabs M37L01), and the source fibers were coupled to this fiber by use of a SMA to FC adapter (Thorlabs ADAFCSMAB1).

The detector and lock-in amplifier were the same as in the coherent setup. The analog output

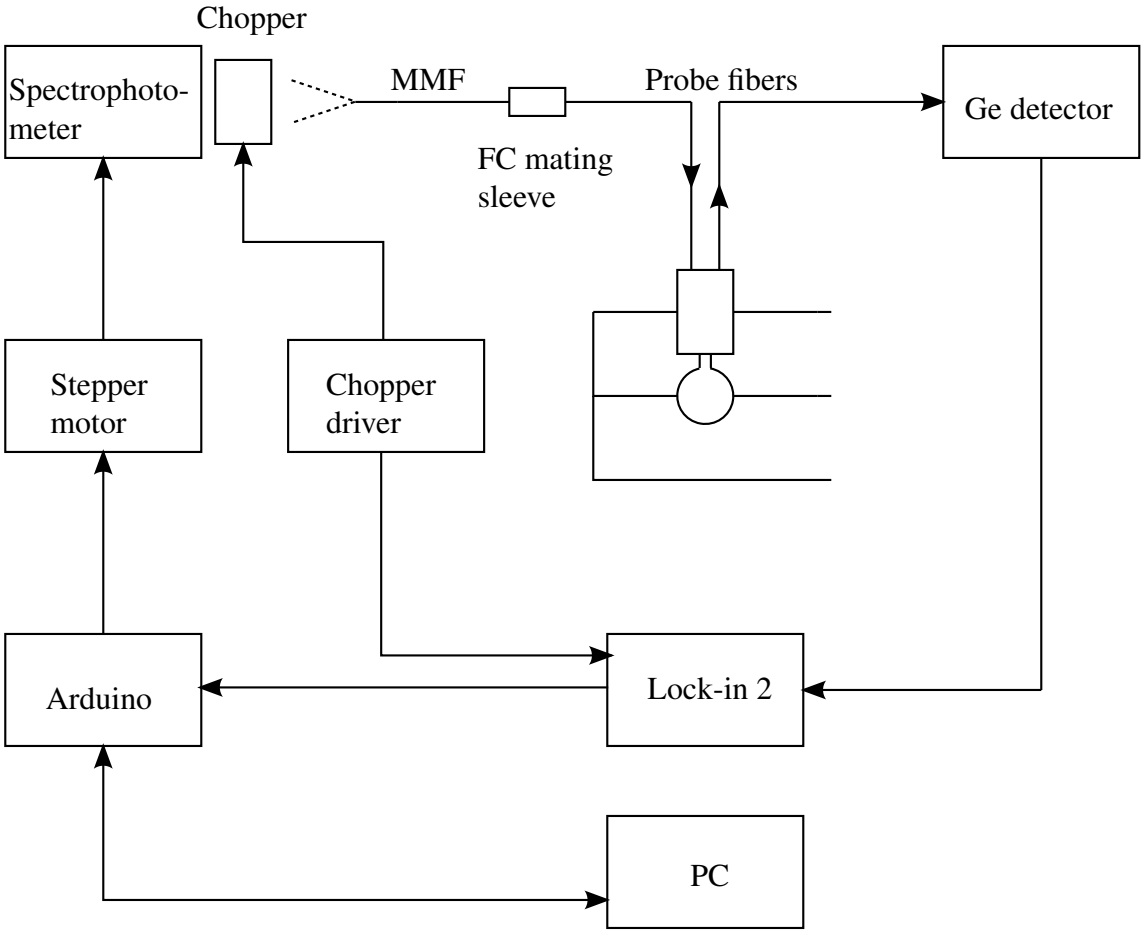

Figure 5.11: A representation of the broadband experimental setup.

from the lock-in amplifier was digitized by the Arduino. The resolution of the analog to digital converter on the Arduino was limited to 10 bits, yielding an effective resolution of $4.9\ \mathrm{mV}$. The Arduino was connected to a PC, and was run by in-house software. This software allowed for automated wavelength selection and data collection. The user selects a wavelength interval and the separation between subsequent wavelengths, effectively deciding how many data points is recorded within the interval. The dwell time on each wavelength is also set. This must be large enough to allow the output from the lock-in to settle. Calibration of the wavelength selection was done by relating an integer representing the stepper position of the motor to a wavelength value shown by the internal display of the instrument. A spline interpolation was used for wavelengths in which no stepper position was recorded. The Arduino would sample voltages at a given rate, and the last value before the wavelength was changed was recorded to a file.

5.4 Measurements

Measurements have been done to investigate the properties of the proposed spherical cavity probe design. The measured physical quantities are the collection efficiencies of the fabricated cavities.

As the bore sizes of the ferrules were larger than the combined size of the source and col-

lection fibers, the fibers were not oriented equally inside the ferrule for the different fiber configurations. There was thus a lack of symmetry, and one could not simply place the ferrule into the ferrule hole in an arbitrary position and expect reproducible results. To compensate for this, the ferrules were marked such that the fibers entering through the entrance port were, approximately, in the same orientation. Figure 5.12 shows a ferrule placed into a PTFE cavity. The red marks were used for alignment.

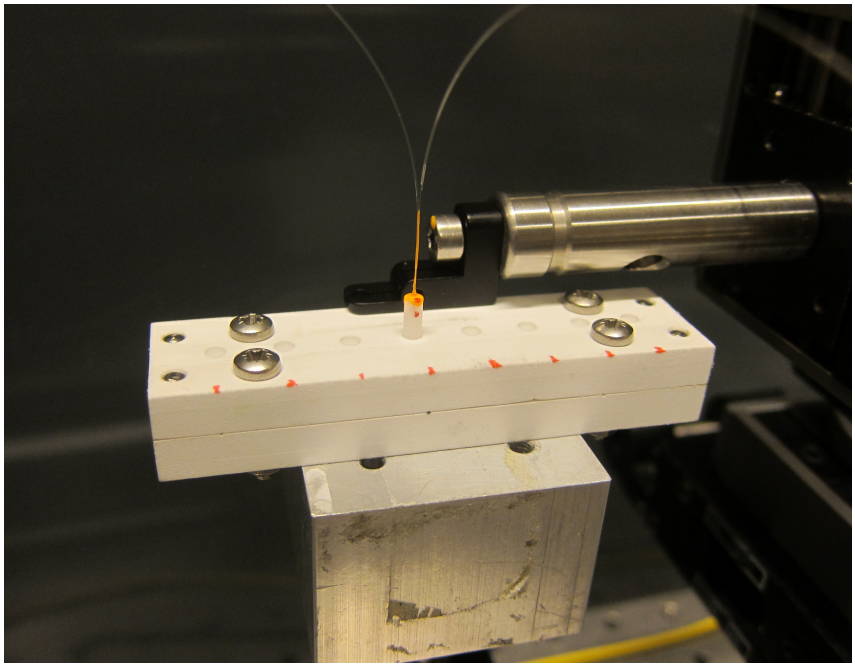

Figure 5.12: The picture shows a ferrule with source and collection fibers placed into a PTFE cavity. The red marks were used for alignment.

To get a sense of the errors done in predicting the collection efficiencies of the cavities and the reproducibility of the results, measurements were done several times. This meant that the ferrule was removed and reinserted into the ferrule hole for each measurement, attempting to keep the orientation of the ferrule fixed. To obtain the fraction of light returned to the collection fiber relative to the total amount emitted by the source fiber, reference measurements had to be done. This was done by placing the ferrule holding both the source and collection fiber directly into the detector. The reference signal v_r was measured with the sensitivity of the lock-in amplifier set to q_r. With the probe ferrule placed into a cavity and the collection fiber inserted into the detector, the signal v was measured at a sensitivity of s. The collection efficiency of the whole system was then estimated by

$$\epsilon_c = \frac{v}{v_r}\frac{s}{s_r} \tag{5.1}$$

The collection efficiency as defined in (5.1) include losses due to attenuation of signal in the collection fibers and losses due to back reflections at the glass-air interface of the collection fiber in front of the detector. The attenuation of the fibers are quoted to be on the order of $1\ \mathrm{dB\,km^{-1}}$, and so the losses due to light propagation in the collection fibers are assumed to be negligible. The fraction s/s_r, essentially the gain of the lock-in amplifier, will have an uncertainty. This uncertainty was minimized by choosing sensitivities that kept the measured

signals well within the full scale range of the instrument. A measure of the the uncertainty in the collection efficiencies is in the following set to equal the fluctuations due to repeated measurements.

5.4.1 Measurements with coherent setup

The experimental procedure for measurements of the collection efficiencies with the coherent setup was as follows. First, a reference signal $v_{r,1}$ was measured. The ferrule with source and collection fibers was then lowered into a cavity. The signal was allowed to stabilize before a value v_1 was recorded. The ferrule was then removed from the entrance port and reinserted. Again, the signal was allowed to stabilize and a new value v_2 was recorded. This was repeated 10 times. After 10 repetitions, a new reference signal $v_{r,2}$ was measured to check for drift in the output of the diode. The average collection efficiency of the cavity was calculated by

$$\epsilon_c = \frac{\langle v_i \rangle}{\frac{1}{2}(v_{r,1} + v_{r,2})} \frac{s}{s_r} \tag{5.2}$$

where

$$\langle v_i \rangle = \frac{1}{10} \sum_{i=1}^{10} v_i \tag{5.3}$$

A measure of the variation in ϵ_c was quantified by calculating extremal values ϵ_{max} and ϵ_{min}

$$\epsilon_{max} = \frac{\max\{v_i\}}{\min\{v_{r,1}, v_{r,2}\}} \frac{s}{s_r} \tag{5.4}$$

$$\epsilon_{min} = \frac{\min\{v_i\}}{\max\{v_{r,1}, v_{r,2}\}} \frac{s}{s_r} \tag{5.5}$$

This process was repeated for cavities of aluminium, coated aluminium and PTFE. Table 5.3 lists the fiber configurations that were used for the different materials. Figure 5.13 shows a typical experiment with the coherent setup. Due to large fluctuations in the values of collection efficiencies for the cavities made of aluminium, measurements were done with a ferrule being rotated while inside the entrance port. Using the the aluminium cavity of diameter $D = 1.5$, the ferrule holding fiber configuration A was rotated in increments of 45 °, and a collection efficiency was calculated for each position.

Table 5.3: The table lists the fiber configurations with corresponding cavity materials used in measurements with the coherent setup.

Material	Fiber configurations
PTFE	A, B, C,D
Coated Al	A, B
Al	A

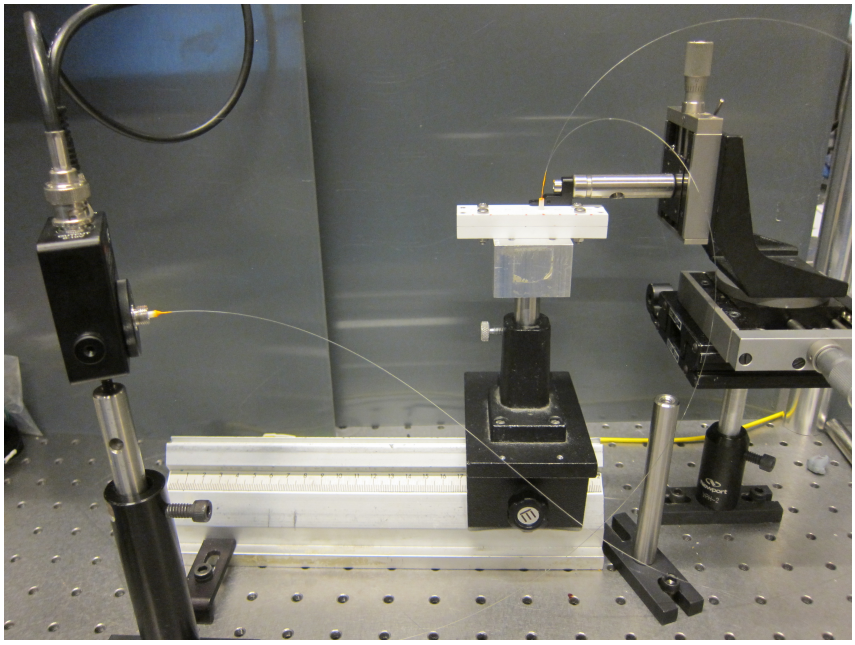

Figure 5.13: The image shows a typical experiment with the coherent setup. The collection fiber was attached to the detector, seen to the left in the image. A ferrule holding source and collection fiber were placed inside the entrance port of a cavity. The yellow fiber to the right in the picture is the SMF (SMF 2) that was connected to the laser diode fiber (SMF 1).

5.4.2 Measurements with broadband setup

To see the effect of a wavelength dependent reflectivity of the cavity walls, it was wanted to do spectral measurements. These measurements were considerably more difficult and time consuming than measurements done with the laser diode. This was due to the low amount of optical power coupled from the spectrophotometer into the source fiber. The sensitivities required for reference measurements were already in the μV range, and the sensitivities required for measurements of the cavities were in the nV range. In order to obtain reliable results, measurements were done with a cavity and fiber configuration that had an adequate collection efficiency. The coated aluminium cavity with diameter $D = 1.25$ mm and fiber configuration B were chosen. By amplifying the voltage at the detector by 10 dB and setting the bandwidth of the light emitted from the spectrophotometer to $\Delta\lambda \simeq 40$ nm a signal of sufficient quality was obtained. The integration time of the lock-in amplifier was set to $\tau = 10$ s and the dwell time at each center wavelength was 30 s. A measurement was done every 40 nm in the range $950 - 1790$ nm.

The broadband setup was extensively used in preliminary experiments throughout the time period of this work. One of these experiments were based on scanning two coaxially aligned fibers across a half sphere of aluminium of diameter 1.5 mm. The fibers were of the same type as in fiber configuration A, but they were both polished. The xyz-stage with the ferrule holder was used to move the fibers across the half sphere in a radial direction, and a voltage was recorded every 10 μm. The collection efficiencies were calculated in the same manner as for the other experiments. The center wavelength was set to $\lambda = 1280$ nm as this was the wavelength where the intensity of the light emitted by the spectrophotometer was strongest. The bandwidth of the light was large, as no spectral information was required.

5.4.3 Attempts at measurements with fluids

After performing the experiments with the fabricated cavities kept in air, it was planned to investigate how the response of the cavities changed when fluids of various absorbing and scattering properties were injected into the cavities. A laser diode operating at $660\ \mathrm{nm}$ was readied for use, in large due to the low amount of water absorption at this wavelength. Scattering and absorbing fluids were prepared. For a scattering fluid, bovine serum albumin (BSA) was dissolved in distilled water at a concentration of $10\ \mathrm{g\,L^{-1}}$. A fluid absorbing at $660\ \mathrm{nm}$ was prepared by adding standard food dye to distilled water. The amount of dye added was such that the absorption coefficient of the solution at $660\ \mathrm{nm}$ was approximately 0.37 $\mathrm{mm^{-1}}$. These solutions were to be diluted, and in some cases mixed to create turbid fluids.

As the paint used in the coating of the aluminium spheres dissolves in water, the plan was to use the PTFE cavities for measurements with fluids. The porosity and lack of structural stability of the PTFE made measurements with fluids difficult. The region where the half spheres were clamped together caused rapid leakage of fluid, and the large pore size of the material caused water and dye particles to seep into the material. Several attempts were made to obtain reliable results without success. The cavities were all finished during the last weeks of the time period of this thesis due to numerous delays in the fabrication process and delays in the delivery of materials, and so there were not sufficient time to design and create new prototypes that could be used for the planned experiments.

Chapter 6

Results and discussion

This chapter contains results from simulations and from experiments. The results from the simulations will be presented first, followed by the results from the experiments. The results will be discussed in order of appearance. A section of general discussion ends the chapter.

6.1 Modeling

The results from the simulations with the Monte Carlo model are divided into four sections. These sections correspond to the type of medium that was modeled. All results have a relative error of less than 10%, and the results are thus presented without error bars for better visibility. The axes of the graphs that presents the results are labeled with the parameters defined in chapter 4.

6.1.1 Transparent medium

Figure 6.1 shows how the collection efficiency varies as a function of cavity radius and wall reflectivity for a transparent medium. The order of magnitude of the collection efficiency is of the same level as for the ideal integrating sphere, which is expected. One can clearly see the importance of a high wall reflectivity, as the collection efficiency scales in an exponential fashion with respect to ρ. The rate of change of the collection efficiency as the wall reflectivity increases is low when the magnitude of the wall reflectivity is low.

In figure 6.2 the portion of photons lost to the entrance port and to the wall is shown. The portion of photons lost to the wall ϵ_w increases monotonically when the cavity radius increases, while the portion of photons lost to the entrance port ϵ_e decreases monotonically. This is due to the fact that the probability of a photon hitting the entrance port is reduced when the cavity radius is increased. The effect of an increased wall reflectivity is that the portion of photons lost to the wall decreases, and this means that there is a higher chance of photons being lost to the entrance port or photons being collected by the collection fiber. This is seen in the symmetry of the results in figure 6.2.

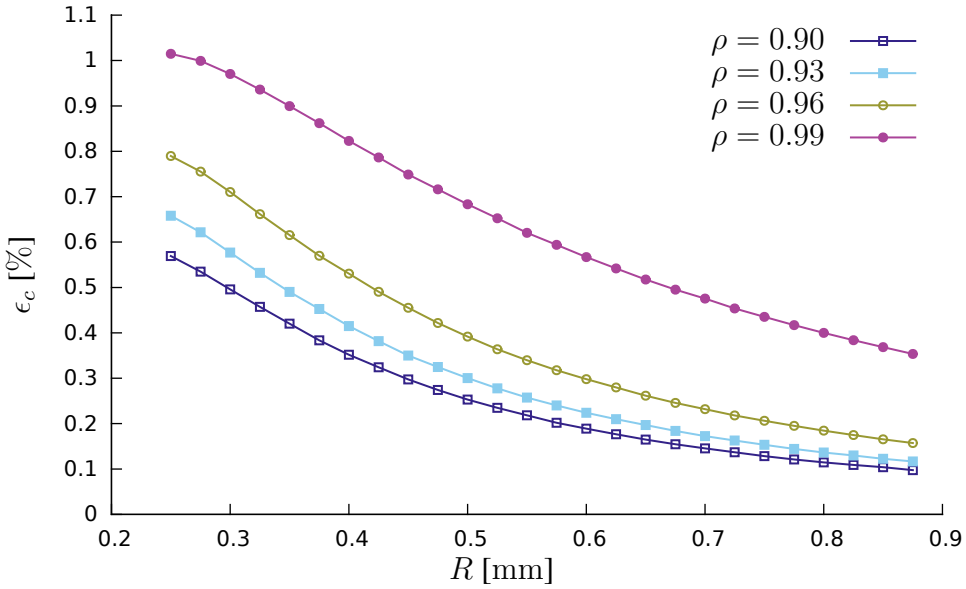

Figure 6.1: The collection efficiency ϵ_c as a function of sphere radius R for four values of the wall reflectivity ρ.

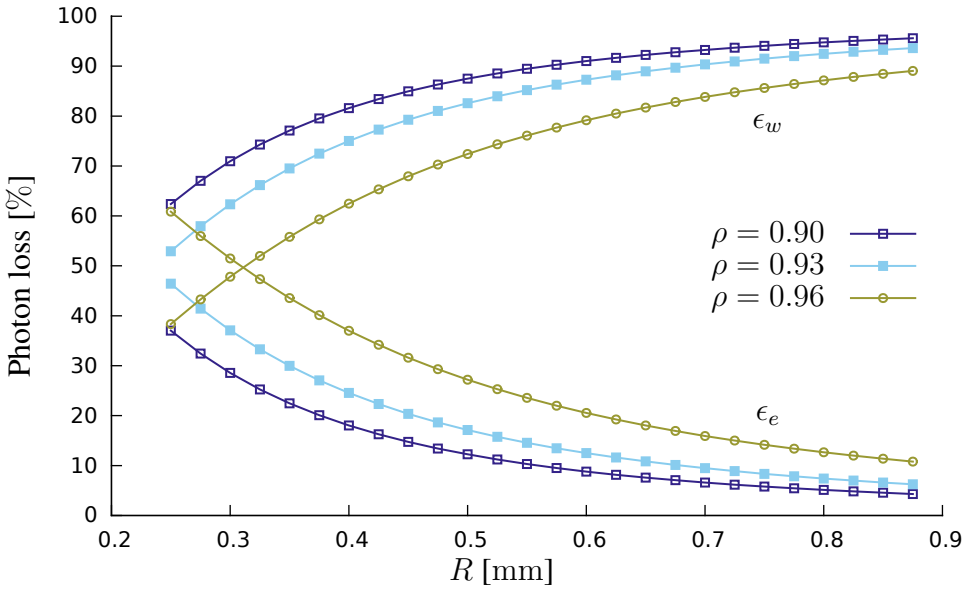

Figure 6.2: The portion of photons lost to the entrance port ϵ_e and to the cavity wall ϵ_w as a function of cavity radius R for three values of wall reflectivity ρ.

In figures 6.3 and 6.4 the mean photon path length and the averaged standard deviation of photon path length are shown as functions of cavity radius for four wall reflectivities, respectively. It is evident that the model suggests that it is possible to achieve path lengths much longer than the characteristic length scale of the probe, which may be set to $L_c = 2D$. The mean path length is seen to scale approximately linearly in R for the larger cavities, with slope determined by ρ. This slope scales exponentially in ρ. This is the same trend as in (4.48), which is to be expected when the cavities become large compared to the size of the entrance port.

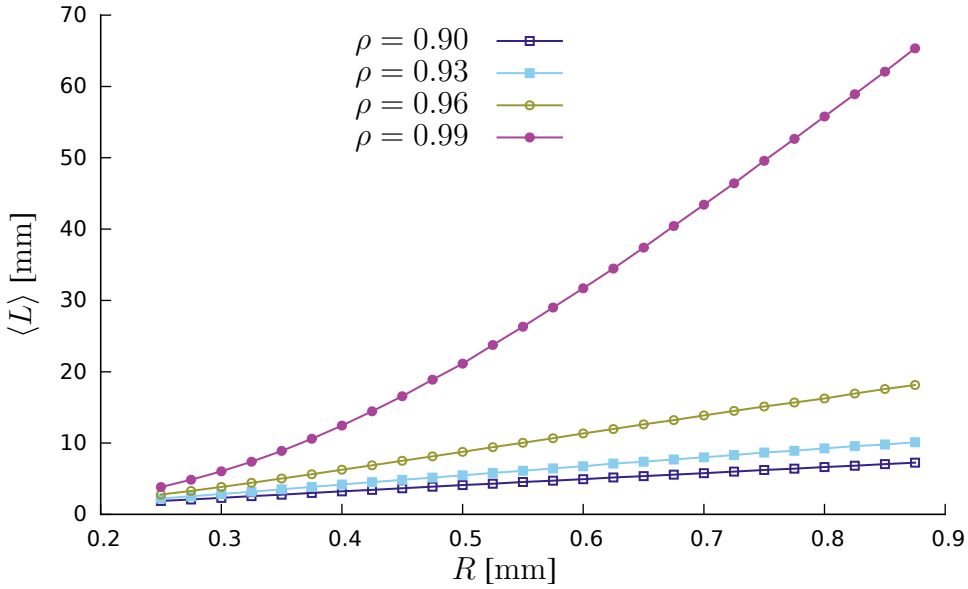

Figure 6.3: The mean path length of photons $\langle L \rangle$ as a function of cavity radius R for four values of wall reflectivity ρ.

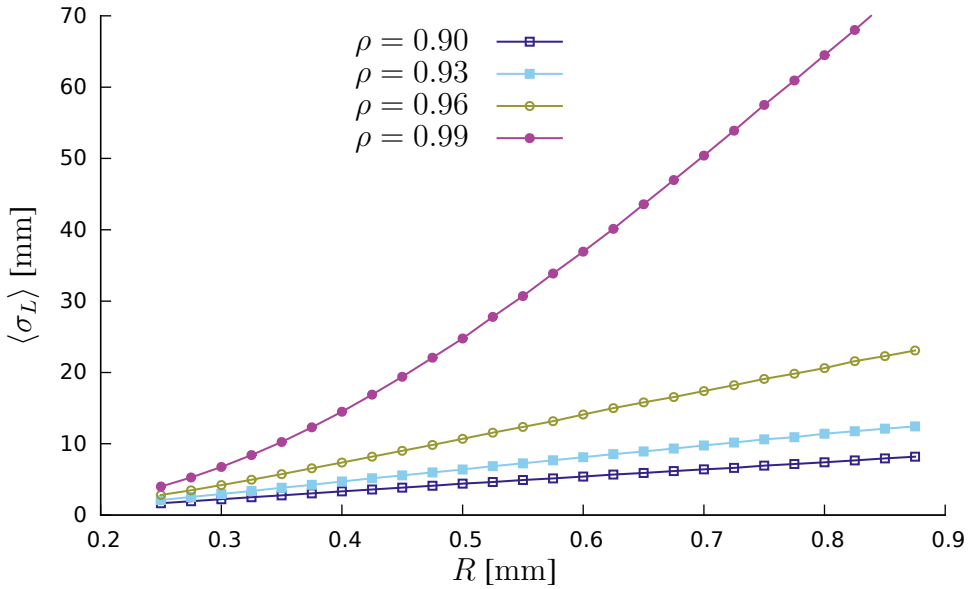

Figure 6.4: The averaged sample standard deviation of path length of photons $\langle \sigma_L \rangle$ as a function of cavity radius R for four values of wall reflectivity ρ.

While the mean path length is large, so is the standard deviation of path lengths. This suggests a broad distribution of path lengths, and a standard deviation that is of the same order of magnitude as the mean is typical for exponentially decaying distributions. Figure 6.5 shows the tail of the distribution of path lengths on a log scale for a cavity with $R = 0.5$ mm and $\rho = 0.96$. The amount of photons emitted into the cavity was here $N = 10^8$. The straight line indicates a nearly perfect exponential behaviour of the distribution. The distribution of path lengths can also be cast into a distribution of collection times if one thinks of the photons as a

pulse of light emitted into the cavity. The shape of such a distribution is equal to the distribution of path lengths if the speed of the propagation of light inside the cavity is well defined. For a cavity of this size, the time scale is on of the order of 10 ps. The exponentially decaying behaviour in figure 6.5 agrees with temporal measurements on spherical integrating cavities on a larger scale [31, 41].

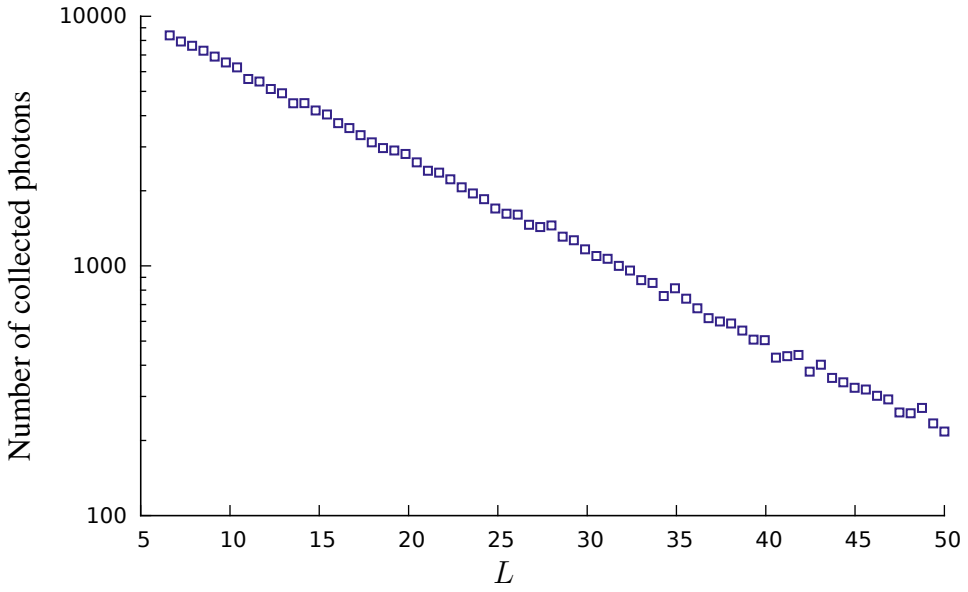

Figure 6.5: The number of collected photons with path length L presented on a log scale. The cavity radius is $R = 0.5$ mm and the wall reflectivity is $\rho = 0.96$. A total of $N = 10^8$ photons were emitted into the cavity.

From the discussion of the ideal integrating sphere in section 2.4, the numerical aperture of the collection fiber may have a large impact on the collection efficiency. This is seen in figure 6.6 where the variation of the collection efficiency with respect to numerical aperture is shown for $\rho = 0.9$ and $\rho = 0.99$ for a cavity with $R = 0.5$ mm. The effect of increased numerical aperture is most pronounced when the reflectivity is high. These results suggests that considerable effort should be put into increasing the numerical aperture of the collection fiber in a future design of a spherical cavity probe.

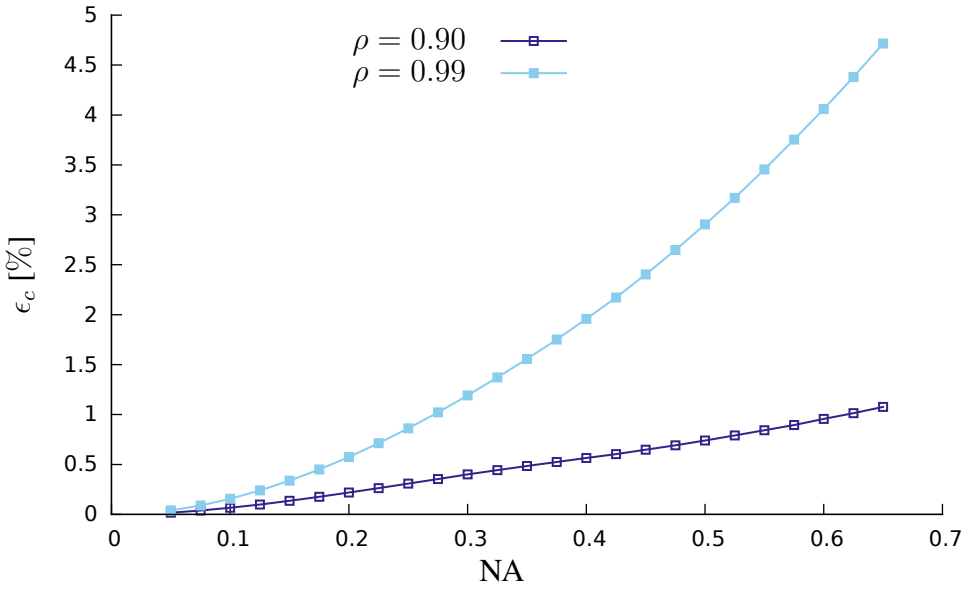

Figure 6.6: The collection efficiency ϵ_c as a function of the numerical aperture NA of the collection fiber for two values of the wall reflectivity ρ. The cavity radius is $R = 0.5$ mm.

6.1.2 Absorbing medium

Figure 6.7 shows the collection efficiency for a cavity filled with an absorbing medium of variable absorption coefficient for three values of wall reflectivity. The radius of the cavity is $R = 0.5$, and 100 data points are represented as continuous lines. One can divide the behaviour of the spherical cavity probe into two regions: the low absorption region and the high absorption region. These regions are separated at an absorption coefficient of α_c. For the probe and fiber geometry modeled in this section, $\alpha_c \approx 0.2$ mm. For $\alpha_a < \alpha_c$, the collection efficiency in figure 6.7 behaves very differently than it does for $\alpha_a > \alpha_c$. In the low absorption region, the collection efficiency drops sharply for small changes in α_a. This is due to the collection fiber collecting photons with a long path length. In the strong absorption region, the photons that travel a long distance is absorbed by the medium, and only the photons with short path lengths survive and are collected by the collection fiber. The spherical cavity probe may thus act as a classical single pass absorption cell in the strong absorption region, while it acts as a multipass absorption cell in the low absorption region.

In figure 6.8 the data in 6.7 is represented in terms of absorbance. The reference is set to $\epsilon_c(0)$ for each value of ρ. The linear behaviour in the strong absorption region indicate that the probe behaves as a single pass cell. However, in the low absorption region there is a non-linear relation between the absorbance and α_a. The functional form of the absorbance is similar to what has been obtained both numerically and experimentally in other works [30, 31]. The slope of the absorbance curve represents how sensitive the probe is to a perturbance of the current absorption coefficient of the fluid in the probe. This slope may be called the effective path length L_{eff} of the light in the probe. For a single pass absorption cell, L_{eff} is the size of the cell. In figure 6.7 one can see that L_{eff} is largest in the low absorption region, decreases as α_a increases and approaches a constant in the high absorption region. This constant is approximately $L_{\text{eff}} \approx L_c = 2D$, i.e on the same scale as the physical size of the probe.

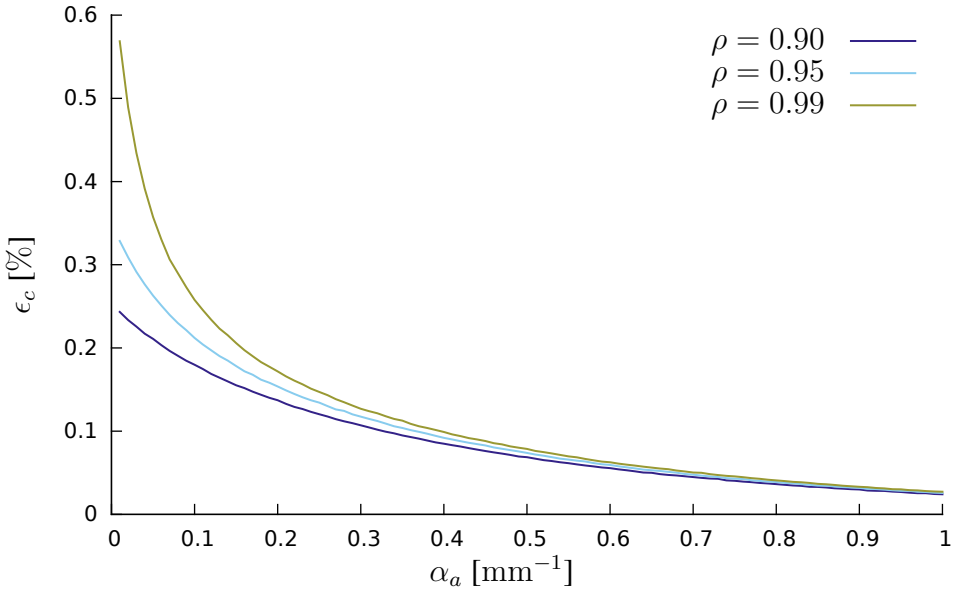

Figure 6.7: The collection efficiency ϵ_c as a function of absorption coefficient α_a for three values of wall reflectivity ρ. The cavity radius is $R = 0.5$ mm. 100 data points are displayed as continuous lines for better visibility.

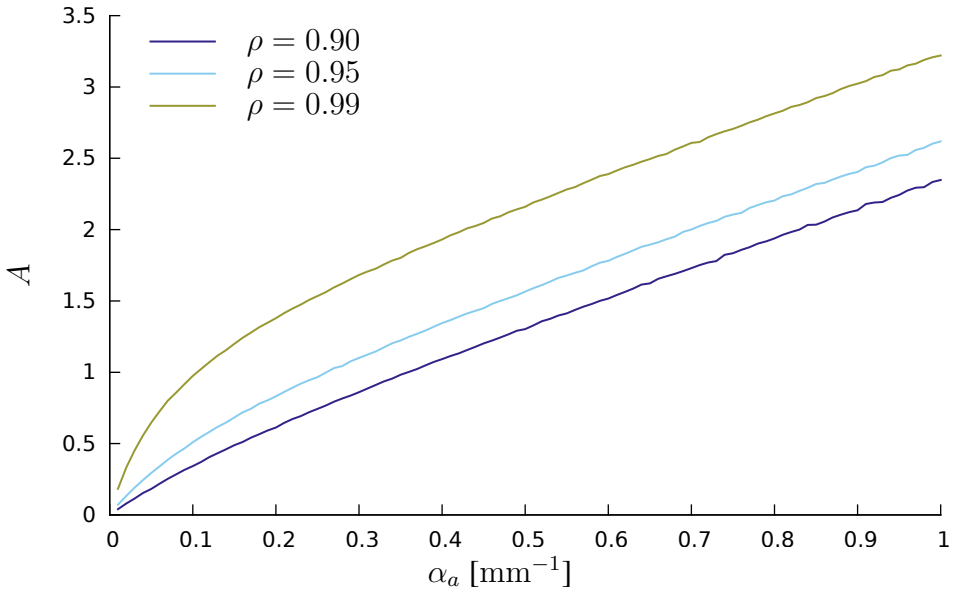

Figure 6.8: The absorbance A, referenced to $\epsilon_c(0)$, as a function of absorption coefficient α_a for three values of wall reflectivity ρ. The cavity radius is $R = 0.5$ mm and the numerical aperture of the collection fiber is NA $= 0.22$. 100 data points are displayed as continuous lines for better visibility.

Figure 6.9 shows results from the same system as was presented in figure 6.8, but with the numerical aperture increased to NA $= 0.5$. It is evident that the non-linear behaviour of the absorbance extends to larger values of α_a. By increasing the collection capabilities of the collection fiber, one effectively extends the low absorption region of the probe.

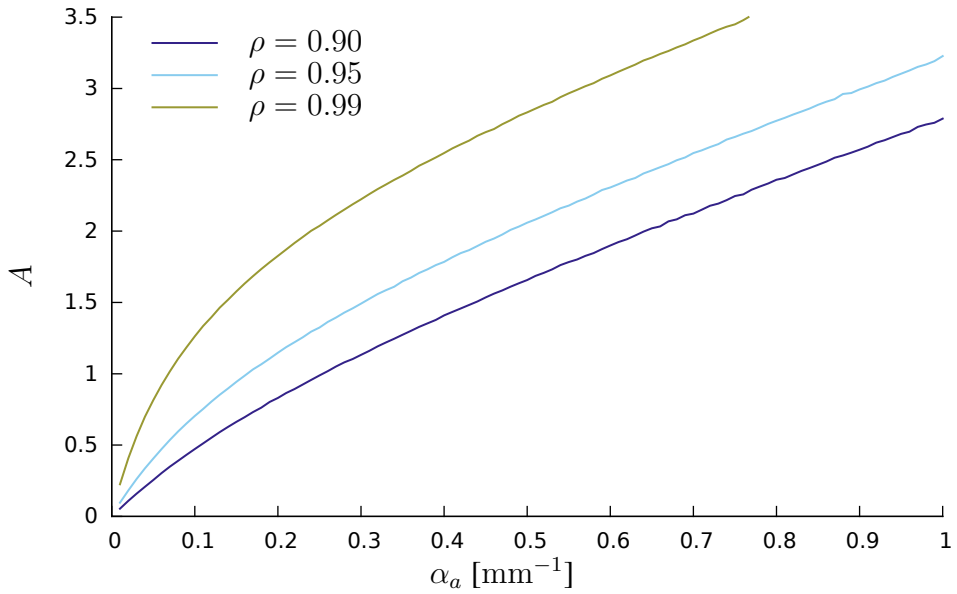

Figure 6.9: The absorbance A, referenced to $\epsilon_c(0)$, as a function of absorption coefficient α_a for three values of wall reflectivity ρ. The cavity radius is $R = 0.5$ mm and the numerical aperture of the collection fiber is NA $= 0.5$. 100 data points are displayed as continuous lines for better visibility.

6.1.3 Scattering medium

Figure 6.10 shows the collection efficiency as a function of the scattering coefficient α_s for three values of the anisotropy factor g. The medium is purely scattering, the cavity radius is $R = 0.5$ mm and the wall reflectivity is $\rho = 0.95$. There is a reduction in the collection efficiency both when α_s is increased and when the scattering becomes more isotropic. This is likely due to photons interacting with the cavity wall more often than if the medium was transparent, resulting in fewer photons reaching the collection fiber. The photons that do reach the fiber will have propagated a longer distance due to the randomization induced by the scattering, and this is seen in figure 6.11 where the mean path length $\langle L \rangle$ is shown as a function of α_s for the same values of g.

These results highlight how a spherical cavity probe may be resistant to scattering effects. One can compare these results with a probe having an unshielded free optical path of L_c. For such a probe, and if one assumes that every scattering event results in loss of a photon, the collection efficiency could scale as $\epsilon_c \propto \exp(-\alpha_s L_c)$. Such a scaling would result in a collection efficiency several orders of magnitude lower than what one could get in a cavity-based probe.

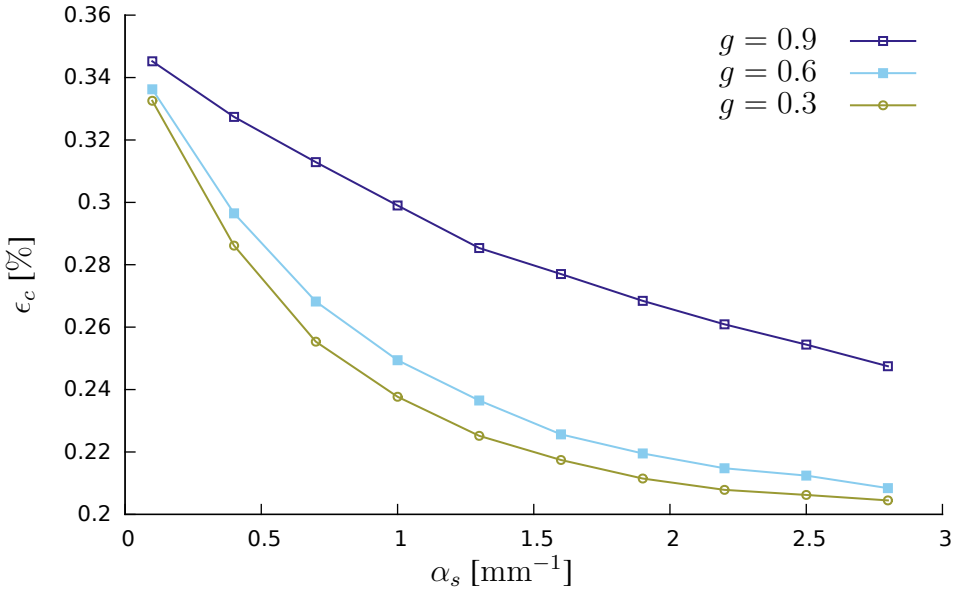

Figure 6.10: The collection efficiency ϵ_c as a function of scattering coefficient α_s for three values of the anisotropy factor g. The cavity radius is $R = 0.5$ mm. and the wall reflectivity is $\rho = 0.95$.

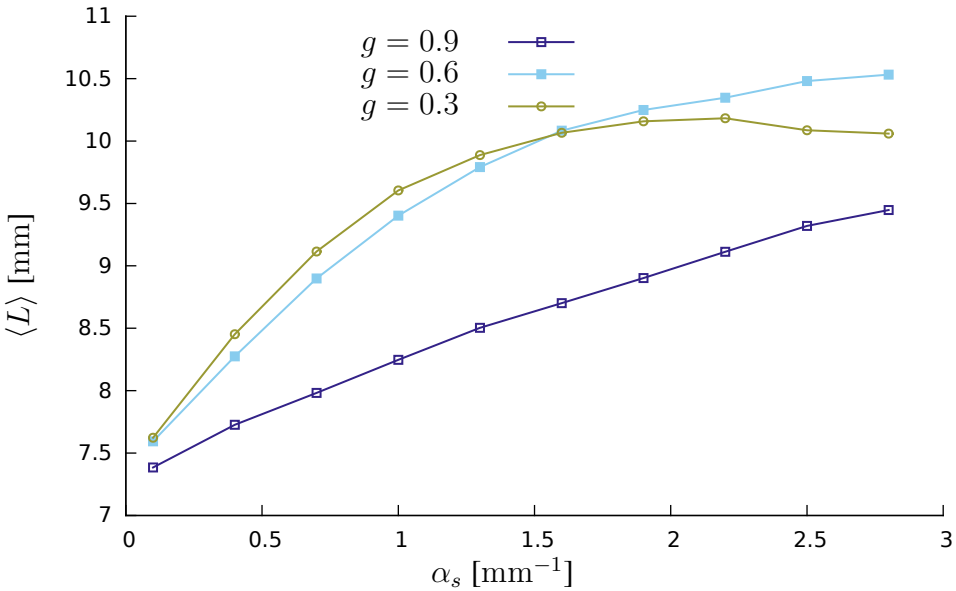

Figure 6.11: The mean path length of photons $\langle L \rangle$ as a function of scattering coefficient α_s for three values of the anisotropy factor g. The cavity radius is $R = 0.5$ mm, and the wall reflectivity is $\rho = 0.95$.

6.1.4 Turbid medium

Figures 6.12 and 6.13 show the variation in collection efficiency for a turbid medium with anisotropy factor $g = 0.9$ and $g = 0.6$, respectively. The cavity radius is $R = 0.5$ mm and the wall reflectivity is $\rho = 0.95$. The results are shown as a function of the absorption coefficient α_a and the dependence on the scattering coefficient α_s is given by the different curves. It can be seen that the collection efficiency is much more sensitive to increased absorption than it is for increased scattering. This is the power of the spherical cavity probe design. The collection efficiency is reduced when the scattering coefficient increases, and this is due to the increased path length of the photons and the resulting increased absorption. By moving to a turbid medium that scatters more isotropic, the collection efficiency is further reduced, as seen in figure 6.13. This is in agreement with the results in figure 6.11, where the path length increases as the anisotropy of the scattering increases. In figures 6.14 and 6.15 the results are presented in terms of absorbance for anisotropy factors $g = 0.9$ and $g = 0.6$, respectively. The behaviour of the absorbance is similar to what it was for for the purely absorbing medium, which may be expected due to the probe being resistant to scattering effects.

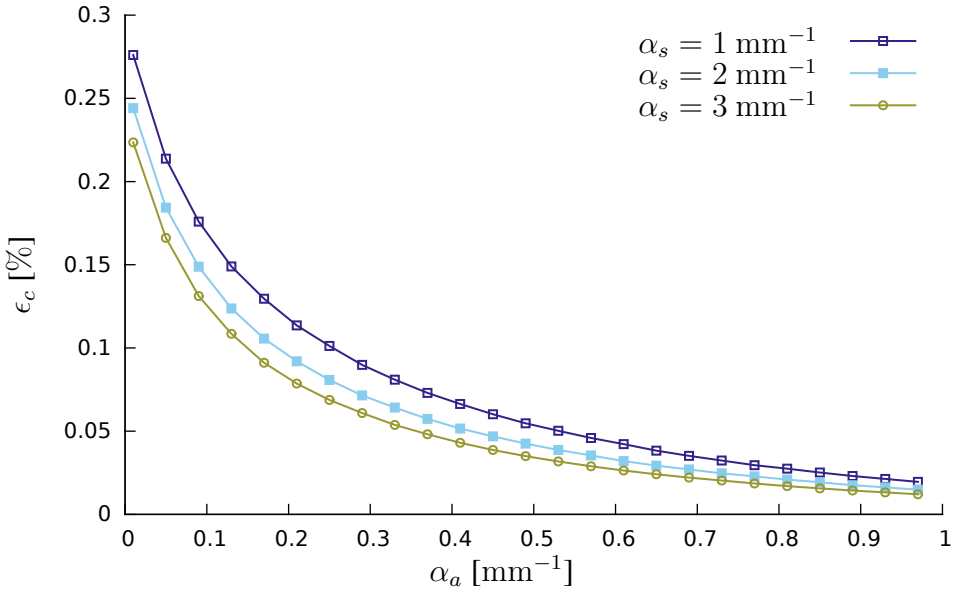

Figure 6.12: The collection efficiency ϵ_c as a function of absorption coefficient α_a for three values of scattering coefficient α_s. The cavity radius is $R = 0.5$ mm, the wall reflectivity is $\rho = 0.95$ and the anisotropy factor is $g = 0.9$.

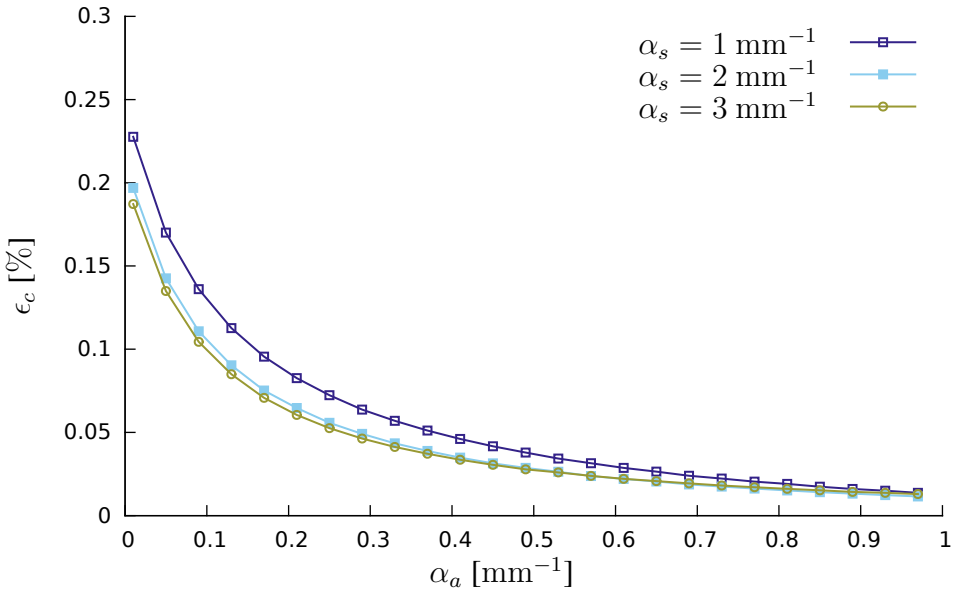

Figure 6.13: The collection efficiency ϵ_c as a function of absorption coefficient α_a for three values of scattering coefficient α_s. The cavity radius is $R = 0.5$ mm, the wall reflectivity is $\rho = 0.95$ and the anisotropy factor is $g = 0.6$.

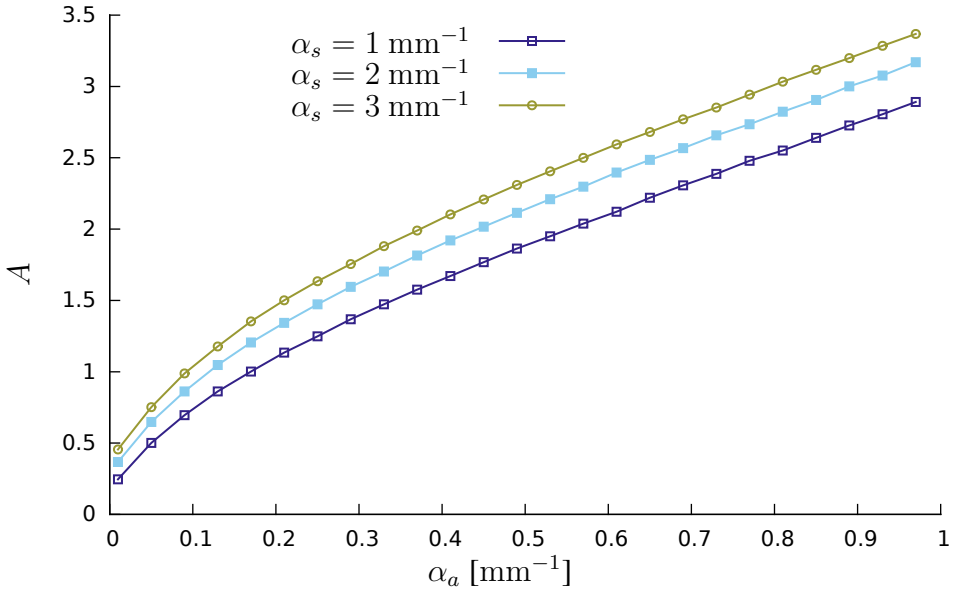

Figure 6.14: The absorbance A, referenced to $\epsilon_c(0)$, as a function of absorption coefficient α_s for three values of scattering coefficient α_s. The cavity radius is $R = 0.5$ mm, the wall reflectivity is $\rho = 0.95$ and the anisotropy factor is $g = 0.9$.

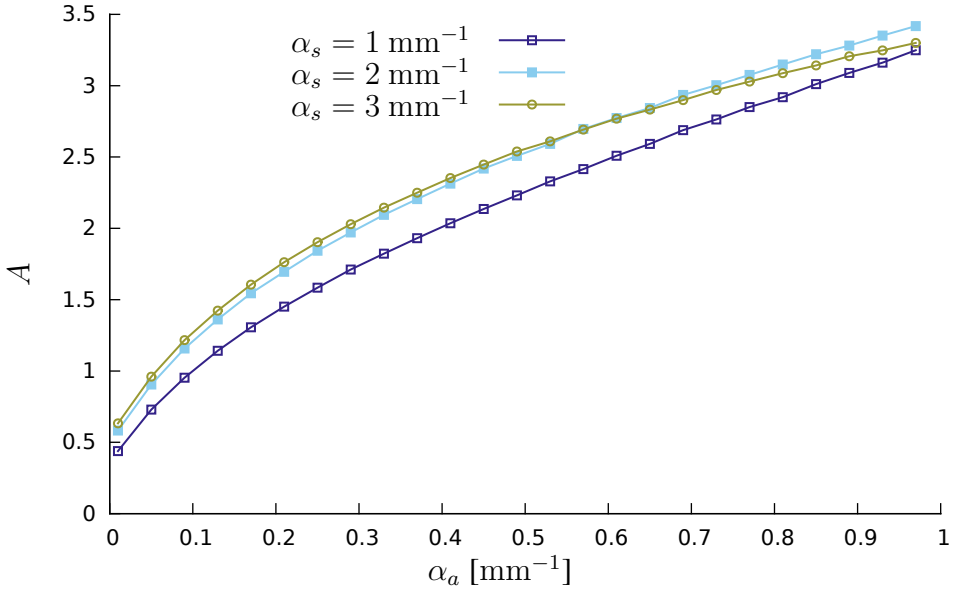

Figure 6.15: The absorbance A, referenced to $\epsilon_c(0)$, as a function of absorption coefficient α_s for three values of scattering coefficient α_s. The cavity radius is $R = 0.5$ mm, the wall reflectivity is $\rho = 0.95$ and the anisotropy factor is $g = 0.6$.

6.2 Experiments

The results from the experimental work are divided into three sections. The results from the measurements with the untreated aluminium cavities will be presented first, followed by the results from the measurements with the cavities made of PTFE. The results from the measurements with the coated aluminium cavities will be presented last. The axes of the graphs that presents the results are labeled with the parameters defined in chapter 5. Errorbars are based on the extremal values calculated by (5.4) and (5.5).

6.2.1 Aluminium cavities

The results from the measurements with the cavities made of aluminium, using the coherent setup and fiber configuration A, are shown in figure 6.16. There are large variations in the collection efficiency ϵ_c for each cavity diameter D, and there is no particular trend in the data. This is likely due to the cavities reflecting specularly, and so the amount of light collected is highly dependent on the positioning of the fibers entering the cavity. The strong dependence on fiber positioning is easily seen in figure 6.17, where the data from measurements with ferrule rotation are shown. By rotating the ferrule it was possible to achieve a change in collection efficiency of an order of magnitude. The results of the radial scan of the half sphere of aluminium with diameter $D = 1.5\ \mathrm{mm}$, using a fiber configuration similar to fiber configuration A and the broadband setup at wavelength $\lambda = 1280\ \mathrm{nm}$, are shown in figure 6.18. There is a clear peak in the collection efficiency when the fibers were above the center of the half sphere. The collection efficiency drops sharply when the fibers were offset about $0.1\ \mathrm{mm}$ to either side of the center of the sphere. This, together with the results in figure 6.17, may explain the apparent random data from measurements on the cavities made of aluminium. One can note that the measured collection efficiencies for the cavities of aluminium are large, and one could consider using a specularly reflecting material in a spherical cavity probe design. However, the large collection efficiency is likely due to a large portion of the light being reflected only once. The path length is thus lower than what one could achieve with a diffusive material. There may be that only a small amount of scattering is necessary make a specular probe design behave as a diffusive probe design [31]. The scattering would effectively do the job of the diffuse walls, randomizing the light distribution in the cavity and increasing the path length. This could allow for an easier fabrication process.

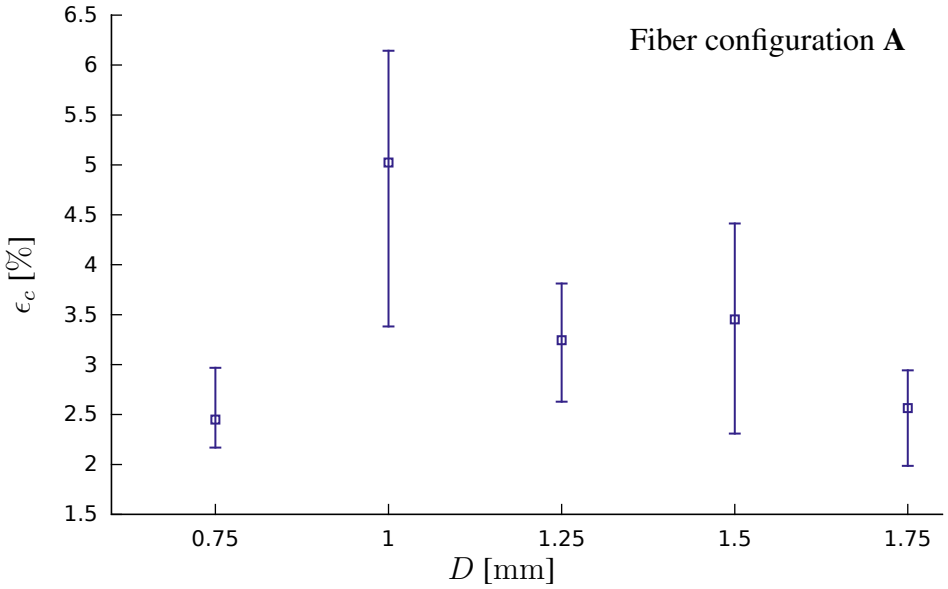

Figure 6.16: The measured collection efficiency ϵ_c of the aluminium cavities using fiber configuration A. D is the cavity diameter.

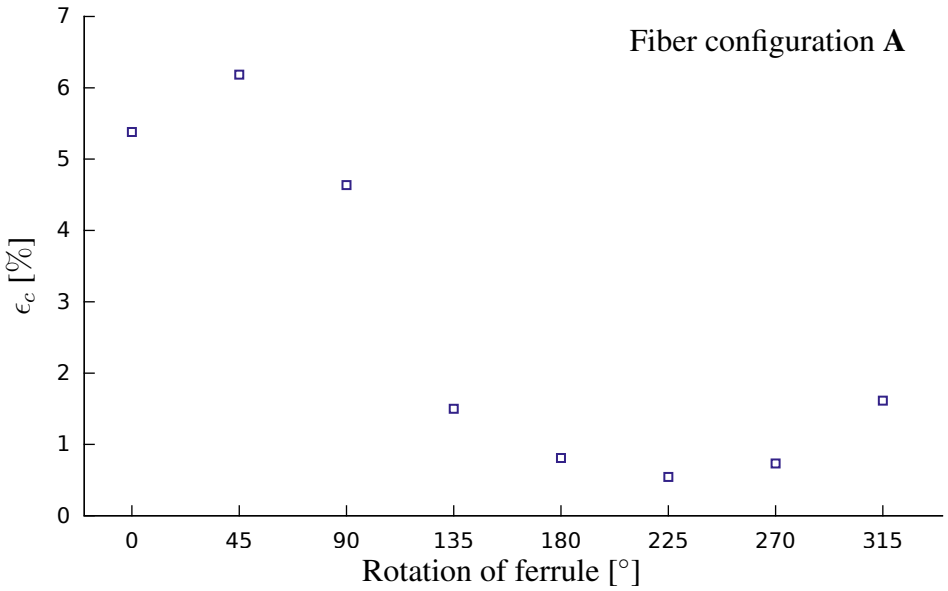

Figure 6.17: The effect of ferrule rotation on the collection efficiency ϵ_c for the aluminium cavity of diameter $D = 1.5$ mm.

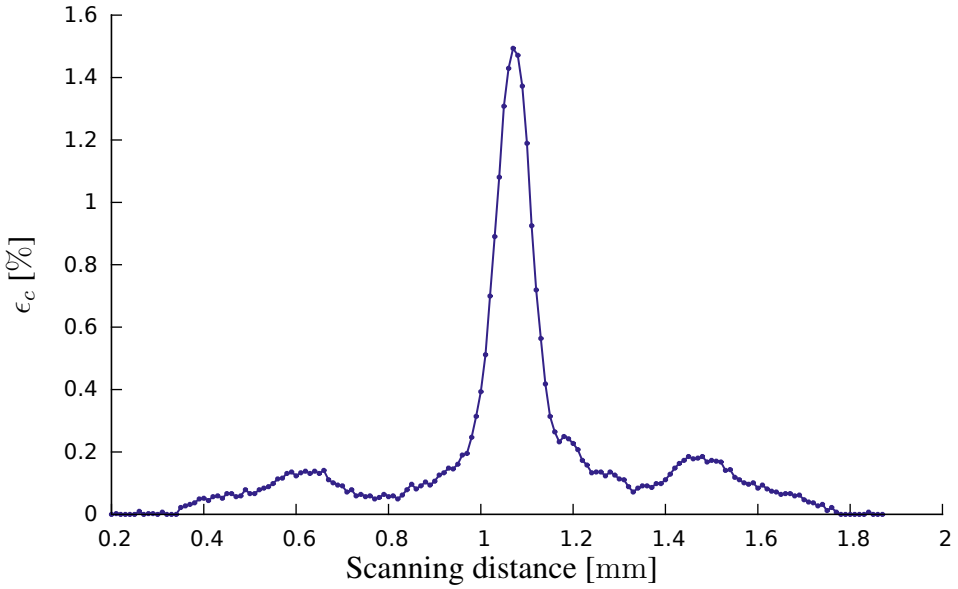

Figure 6.18: The variation in collection efficiency ϵ_c when a fiber configuration similar to fiber configuration A was scanned radially across a half sphere made of aluminium with diameter $D = 1.5$ mm. The scan was incremented at 10 µm.

6.2.2 PTFE cavities

The results from the measurements with the cavities made of PTFE, using the coherent setup and fiber combinations A, B, C and D, are shown in figures 6.19, 6.20, 6.21 and 6.22, respectively. These measurements were, as can be seen from the variation in the collection efficiency for each cavity diameter, much more reproducible than the measurements with the cavities made of aluminium. This is expected because the PTFE cavities reflect light in a diffusive manner. Relative offsets of the fiber positions in the plane of the entrance port of these cavities did not cause the large fluctuations seen for the cavities made of aluminium. The collection efficiencies for all fiber configurations decrease as the diameter of the cavities increases, which is expected. The magnitude of the measured collection efficiencies with fiber configuration A are lower than what the Monte Carlo model predicts. This is partly because the size of the entrance port in the fabricated cavities is much larger than it is in the model. It is also expected that a large amount of light was lost to the region where the half spheres were joined. It may also be that the reflectivity of the cavities was not particularly high. By using the data from the cavity of diameter $D = 1.0$ mm in figure 6.19, and the expression for the collection efficiency in an ideal integrating sphere (2.72), one can estimate the effective reflectivity of the cavity. By doing this one obtains a reflectivity of $\rho \approx 70\%$, which is far from adequate in a spherical cavity probe design.

In going from fiber configuration A to fiber configuration B the core area of the collection fiber is increased by a factor $(200/105)^2 \approx 3.6$, while the rest of the system remains unchanged. One should thus expect approximately a factor 3.6 increase in the collection efficiency when fiber configuration B is used compared to when fiber configuration A is used. As seen in figures 6.19 and 6.20, this is the case. This may suggest that the flux of photons inside the sphere is properly diffused and independent of direction.

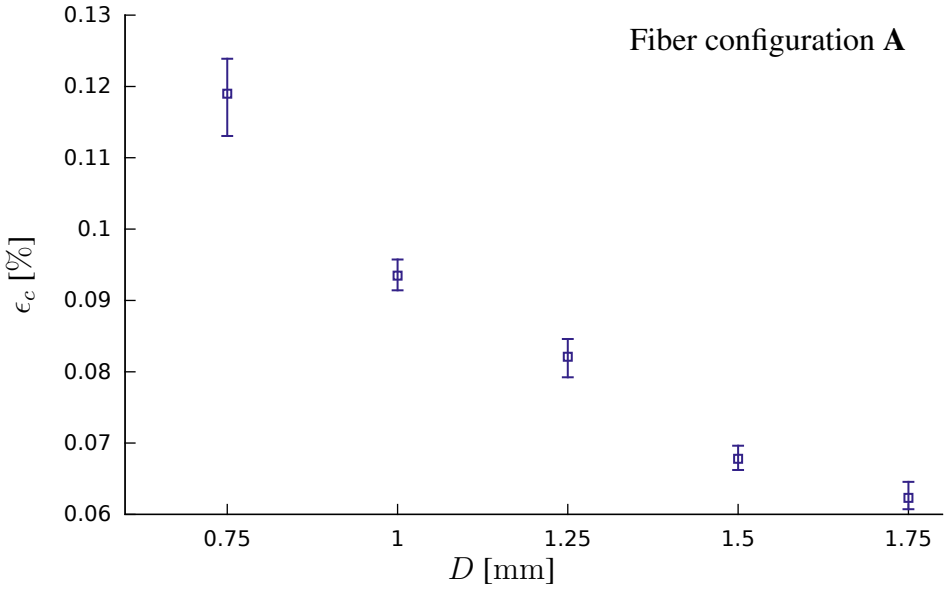

Figure 6.19: The measured collection efficiency ϵ_c of the PTFE cavities using fiber configuration A. D is the cavity diameter.

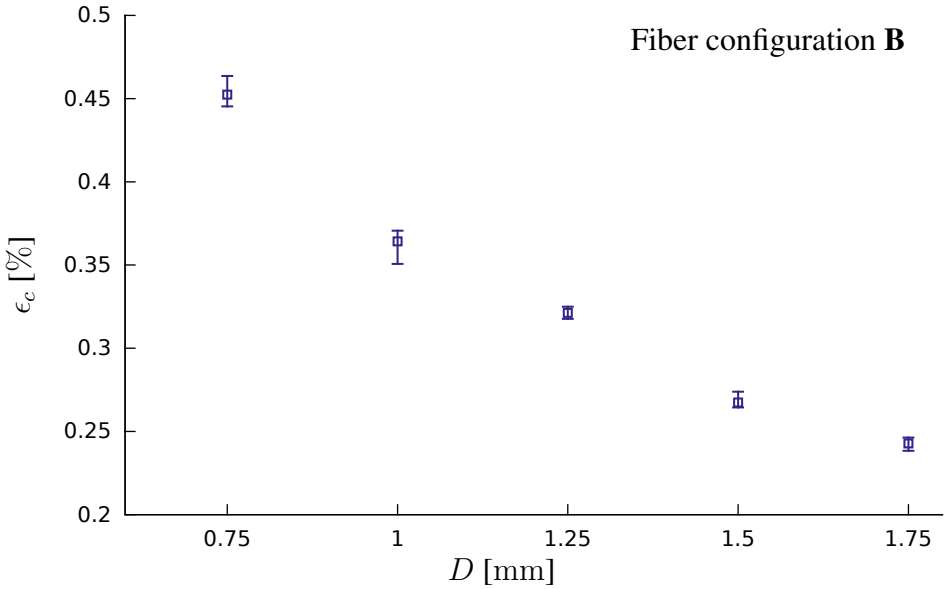

Figure 6.20: The measured collection efficiency ϵ_c of the PTFE cavities using fiber configuration B. D is the cavity diameter.

The fibers with hemispheres, fiber configurations C and D, did not yield better results than the flat ended fibers. If these fibers had a higher numerical aperture than the flat ended fibers, one would likely see a noticeable increase in the collection efficiency. As these fibers were not tested in any way prior to measurements, the principle of using fiber lenses for increased collection efficiency should not be discarded. The position of the collection fibers relative to the sources fibers, seen in figures 5.8 and 5.9, were not adjusted. One could change these distances and see if that has any noticeable effect on the collection efficiency. One could also experiment

with the hemispheres extending further into the cavities. However, the easiest way to increase the collection efficiency would probably be to use a standard flat ended fiber with a higher numerical aperture than the fibers that were used in the experiments.

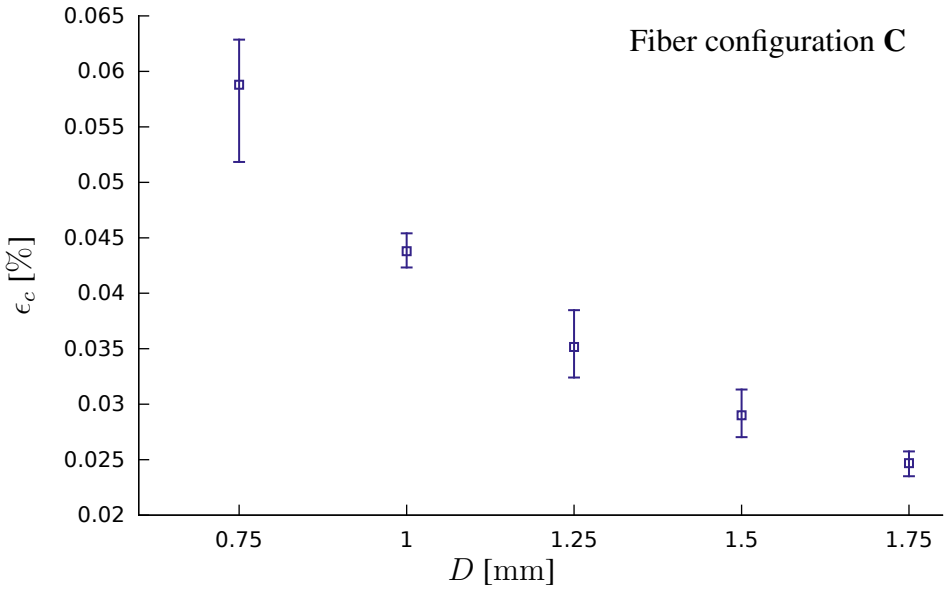

Figure 6.21: The measured collection efficiency ϵ_c of the PTFE cavities using fiber configuration C. D is the cavity diameter.

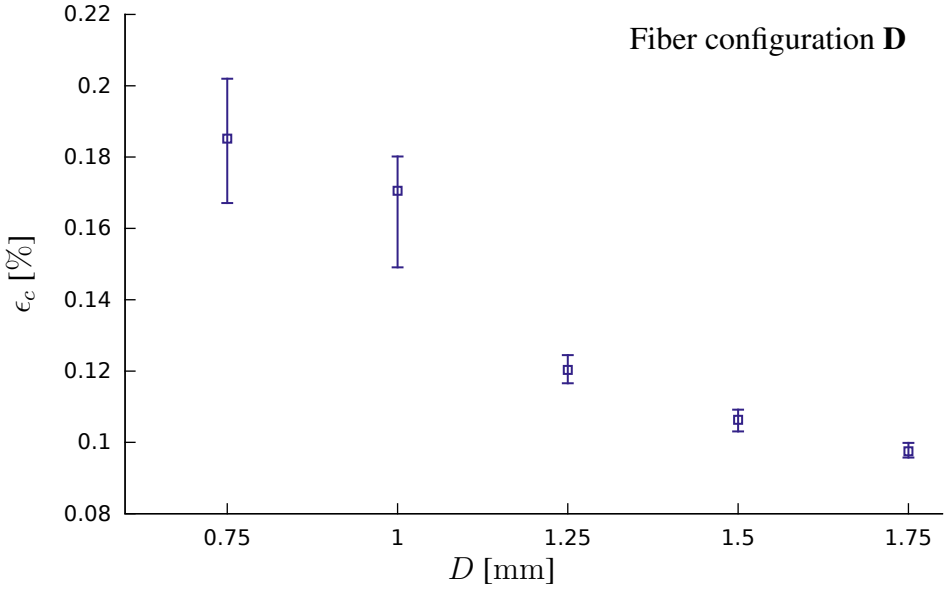

Figure 6.22: The measured collection efficiency ϵ_c of the PTFE cavities using fiber configuration D. D is the cavity diameter.

6.2.3 Coated aluminium cavities

The results from the measurements with the coated aluminium cavities, using the coherent setup and fiber combinations A and B, are shown in figures 6.23 and 6.24, respectively. The qualitative behaviour of these cavities resemble the behaviour of the PTFE cavities. The collection efficiencies for these cavities are approximately a factor 2 larger than for the cavities made of PTFE. This may be due to the coated aluminium having a higher reflectivity than the PTFE. The aluminium cavities were also more precisely fabricated, which could reduce the amount of light lost to the area where the half spheres were joined. It is also possible that the applied diffuse paint caused the size of the cavities to be slightly smaller than the PTFE cavities, further increasing the collection efficiency.

In figure 6.25 the results from the measurements with the coated aluminium using fiber combination A are shown together with results obtained from the Monte Carlo model. The radius of the entrance port used in the simulations was set equal to the radius of the entrance port of the fabricated cavities, i.e. $r_e = D_e/2 = 0.25\ \mathrm{mm}$. The number of system realizations was set to $M = 10$, and simulations were run for wall reflectivities of $\rho = 0.8$ and $\rho = 0.9$. It can be seen that the experimental data behaves similarly to the modeled results for the largest cavities. This does not imply that the model quantitatively predicts the collection efficiencies of the fabricated cavities, as too few experiments have been done. However, it may suggest that the model has some predictive power.

Figure 6.26 shows the dynamic response of the lock-in amplifier used in the spectral measurements when the wavelength was incremented by $40\ \mathrm{nm}$ by the stepper motor. The data is from reference measurements with fiber configuration B inserted directly into the detector. The continuous line represent voltages recorded by the Arduino, while the squares are the last voltages that were recorded before the wavelength was changed. The dwell time at each wavelength was $30\ \mathrm{s}$ and the time constant of the lock-in amplifier was $\tau = 10\ \mathrm{s}$. One can see that the voltages were allowed to settle before the wavelength was incremented. Similar behaviour was seen with the fibers inserted into the cavity with $D = 1.25\ \mathrm{mm}$. Figure 6.27 shows the results from the spectral measurements using the broadband setup, the coated cavity of diameter $D = 1.25\ \mathrm{mm}$ and fiber configuration B. The collection efficiency increases up to $\lambda \approx 1270\ \mathrm{nm}$ before it evens out. If the reflectivities of the cavities were high, one could expect larger differences in the collection efficiency, similar to what was seen in the results from the simulations with a transparent medium. The increase in collection efficiency up to $\lambda \approx 1270\ \mathrm{nm}$ may be due to the reflective properties of the underlying aluminium. Aluminium typically has a reflectivity that increases sharply in the range $800 - 1250\ \mathrm{nm}$ [42].

There is a discrepancy in the value recorded for the collection efficiency at $\lambda = 1550\ \mathrm{nm}$. The value measured using the coherent setup is larger than the value measured using the broadband setup. This may be due to different output intensity profiles of the source fibers. In the coherent setup, the source fiber is coupled to a SMF and this may cause excitation of only the lowest order modes of the source fiber. In the broadband setup, the source fiber is coupled to a MMF of much larger core size, which may result in a higher number of excited modes. The large bandwidth of the light in the broadband setup may also contribute to this discrepancy. The coated aluminium may also not reflect in a perfectly diffuse manner. The increase in collection efficiency for the coherent setup could be due to a part of a more narrow emission profile being reflected specularly. This being said, the spectral measurements were only done once, and so the results are subject to uncertainty.

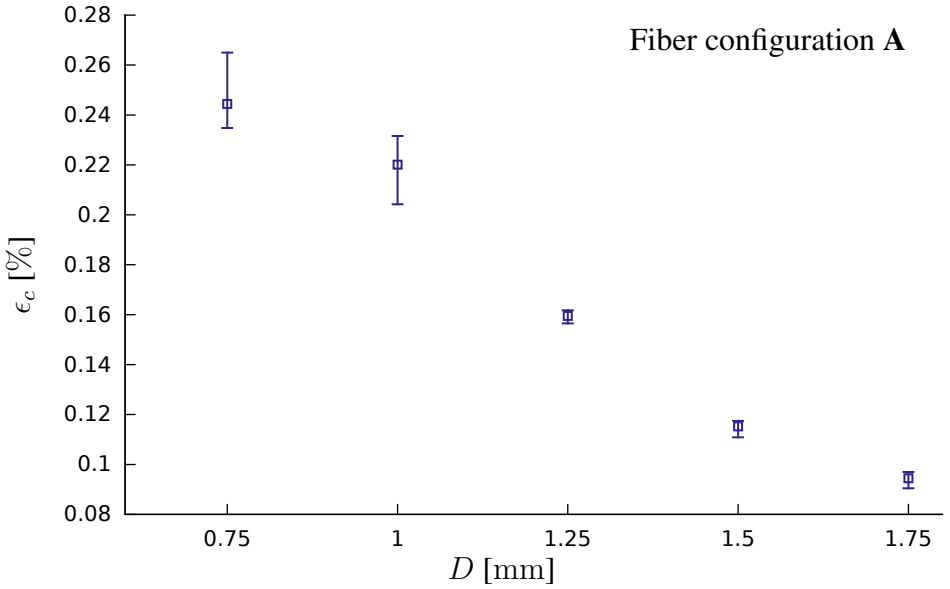

Figure 6.23: The measured collection efficiency ϵ_c of the coated aluminium cavities using fiber configuration A. D is the cavity diameter.

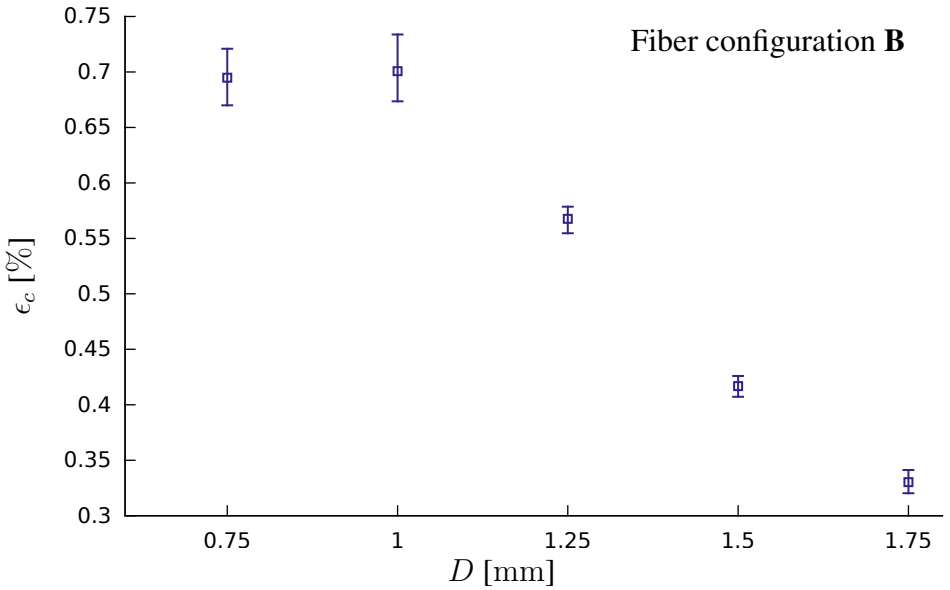

Figure 6.24: The measured collection efficiency ϵ_c of the coated aluminium cavities using fiber configuration B. D is the cavity diameter.

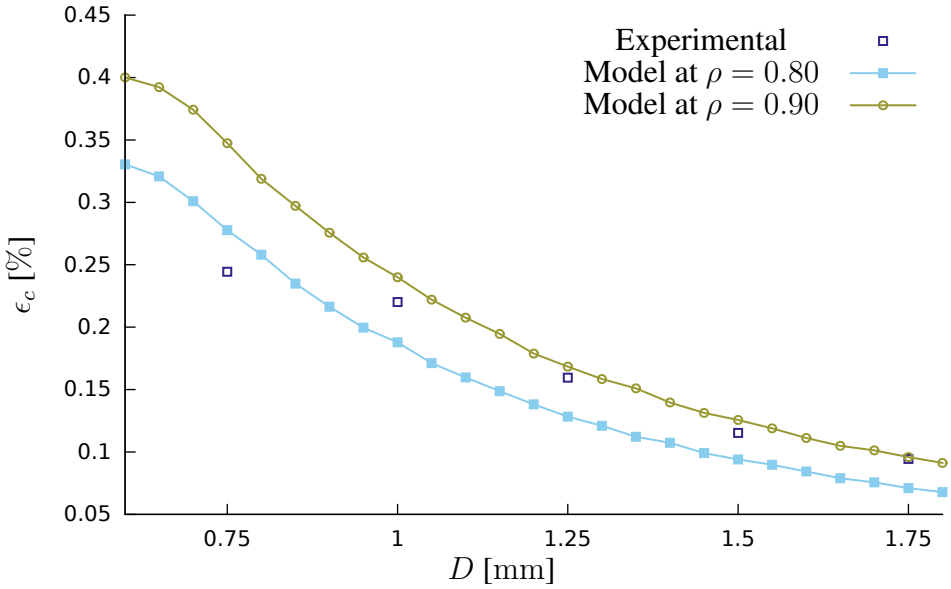

Figure 6.25: The measured collection efficiency ϵ_c of the coated aluminium cavities using fiber configuration A, along with results from the model at two values of wall reflectivity ρ. The radius of the entrance port r_e in the model was set equal to the radius of the entrance port of the fabricated cavities, i.e. $r_e = 0.5$ mm. The number of realizations was $M = 10$. D is the cavity diameter.

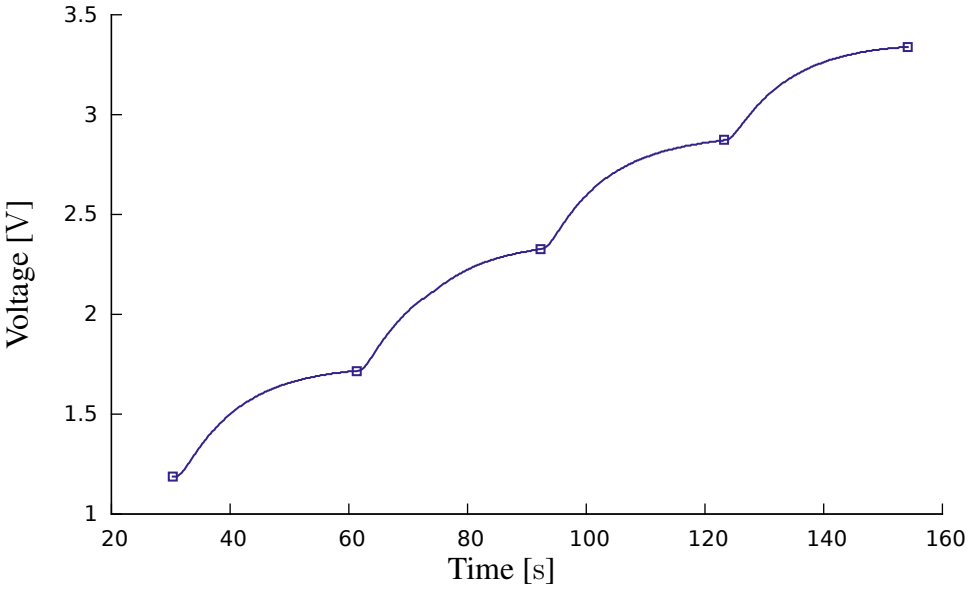

Figure 6.26: A figure showing the dynamic response of the lock-in amplifier when the wavelength was incremented by 40nm. The continuous line represent voltages that were digitized by the Arduino at a high rate, while the squares are the last recorded voltages before the wavelength was adjusted. The dwell time at each wavelength was 30 s and the integration time of the lock-in amplifier was 10 s. The data is from the reference measurement with fiber configuration B.

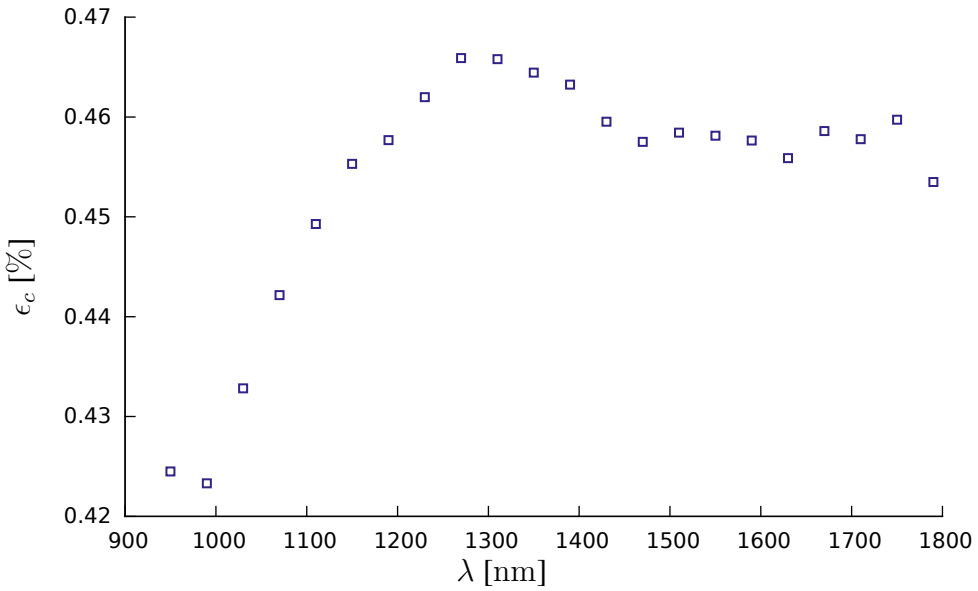

Figure 6.27: The measured collection efficiency ϵ_c of the coated aluminium cavity with diameter $D = 1.25$ mm for various wavelengths λ. Fiber configuration B was used.

6.3 General discussion

The results from the model suggests that a probe design based on spherical cavities may be highly resistant to losses due to light scattering. The possibility of obtaining long path lengths in a small form factor is demonstrated. For weakly absorbing fluids, the spherical cavity probe may act as a multipass absorption cell, yielding increased sensitivity to changes in concentration of absorbing particles. For highly absorbing fluids, there may be evidence that the probe acts as a conventional single pass absorption cell with a path length comparable to the physical size of the cavity. The multipass behaviour of the probe may be extended to fluids with larger absorption coefficients by increasing the light collection capabilities of the probe. This could be done by increasing the numerical aperture of the collection fibers, using larger core fibers or using several collection fibers.

For a typical biofluid with absorption properties dominated by water and for the modeled probe geometry, the weakly absorbing region corresponds to $\lambda < 1400\ \mathrm{nm}$, i.e. in the second overtone band of glucose. The highly absorbing region may be defined as the overtone band of glucose, around $\lambda = 1700\ \mathrm{nm}$. The spherical cavity probe may be a good design for obtaining the long path lengths necessary in probing the second overtone band for glucose specific information. In the first overtone band, the model suggests that the effective path length approaches the physical size of the probe. For a probe with a cavity of diameter $D = 1.0\ \mathrm{mm}$ the effective path length is approximately $L_{\mathrm{eff}} \approx 2\ \mathrm{mm}$, which is the minimum path length suggested in [18]. The spherical cavity probe may then be a design that could yield suitable path lengths across a large wavelength range. However, these are assumptions based on results from a model. Further experimental work should be done to verify what the model suggests.

The results obtained experimentally show that it is possible to use spherical cavities in an optical fiber probe design. The cavities made of PTFE and coated aluminium yield reproducible results. The qualitative behaviour of the collection efficiencies for these cavities, using fiber combinations A and B, is as expected. The coated cavities performed better than the PTFE cavities, and these were significantly easier to fabricate and work with. It is likely that one can improve the performance of the cavities significantly by moving to a more complex fabrication process. The cavities that were used in the experiments were all rather crude. The splicing of the half spheres were likely to cause large losses, and the size of the entrance port was much larger than it would be in a finalized design. Using fibers with larger numerical apertures could also significantly increase the performance of the cavities.

A natural next step in fabricating a spherical cavity probe would be to use perfect hollow spheres as a starting point. Hollow microspheres made of glass are readily available. Different reflective layers could then be placed on the exterior of the spheres. A small entrance port and a port for fluid management could be created by cutting the glass. Source and collection fibers could be placed in a microfluidic tube, and this tube could be fastened to the entrance port of the sphere. A microfluidic pump could be used for pumping sample fluid in and out of the cavity. One could then investigate experimentally how the probe behaves for fluids with various optical properties, and compare that to what was obtained in the modeling of the probe. After this one could move on to experiments with aqueous glucose, and finally one could do experiments with peritoneal fluid.

Chapter 7

Conclusion and outlook

Conclusion

An optical fiber probe based on a spherical cavity has been proposed as a possible design for glucose sensing by NIR absorption spectroscopy in the peritoneal cavity. The envisioned design contains optical fibers in a microfluidic channel, entering a spherical cavity with highly reflective walls. Active pumping of peritoneal fluid in and out of the probe volume, as well as in-vivo rinsing of the probe, may be possible. A Monte Carlo model has been implemented to investigate the behaviour of the probe in turbid media. Results from the model suggest that the probe is resistant to losses due to scattering effects, and the possibility of obtaining optical path lengths larger than the physical size of the probe is demonstrated. Prototypes of spherical cavities have been designed and fabricated in aluminium and PTFE. Experiments have been done with several fiber combinations, and the light collection efficiency of the cavities have been measured. The results indicate that the probe behaves as expected, but also highlight possibilities of large improvements in the performance of the probe when moving to a more suitable fabrication process. Experiments with fluids of different optical properties must be carried out in order to better understand the spherical cavity probe and to verify results from the model.

Outlook

The cavities used in this work allowed for preliminary experimental investigation of the spherical cavity probe design. Successful experiments were only done with the cavities being empty. A prototype should be created that allows for investigation of the response of the probe when it is filled with various fluids. One should move to a cavity which is not made of two half spheres, unless one can reliably seal the splicing region and keep the reflectivity of the inner wall high. Using hollow glass spheres as prototype cavities could be possible. Such spheres are easy to obtain, and they may allow for easy surface modification because it can be done on the exterior of the glass sphere. One could then experiment with different methods of achieving a high wall reflectivity. The glass spheres could be cut to fit a standard microfluidic tubes which would make measurements with fluids more convenient.

The coherent setup could easily be improved by digitizing the output from the lock-in amplifier and writing software that could allow for automated data recording. With a microfluidic tube connected to a glass cavity and to a pump, one could then study the response of the probe in real time. The probe could be placed in a container filled with a fluid, and the optical properties of this fluid could be varied over time. Spectral measurements would probably require

considerably more work with the current status of the modified spectrophotometer. The main disadvantages of the current broadband setup is the low amount of optical power coupled into the source fibers, the low spectral resolution and the low resolution of the microcontroller digitizing the voltage from the lock-in amplifier. With an improved system, or with a different setup, one could do spectral measurements with glucose.

The Monte Carlo model may be further improved if it shows promise compared to experimental results from measurements with fluids. One could implement a reflectivity based on the Fresnel equations, and one could attempt to model inhomogeneous media.

Bibliography

[1] O. World Health, "Global status report on noncommunicable diseases 2014," 2014.

[2] D. M. Nathan, "Long-term complications of diabetes-mellitus," *The New England Journal of Medicine*, vol. 328, no. 23, pp. 1676–1685, 1993.

[3] N. J. Morrish, S. L. Wang, L. K. Stevens, J. H. Fuller, and H. Keen, "Mortality and causes of death in the who multinational study of vascular disease in diabetes," *Diabetologia*, vol. 44, no. S2, pp. S14–S21, 2001.

[4] D. Control, C. Trial, *et al.*, "Intensive diabetes treatment and cardiovascular disease in patients with type 1 diabetes," *The New England journal of medicine*, vol. 353, no. 25, p. 2643, 2005.

[5] N. Oliver, C. Toumazou, A. Cass, and D. Johnston, "Glucose sensors: a review of current and emerging technology," *Diabetic Medicine*, vol. 26, no. 3, pp. 197–210, 2009.

[6] D. R. Burnett, L. M. Huyett, H. C. Zisser, I. Doyle, F. J., and B. D. Mensh, "Glucose sensing in the peritoneal space offers faster kinetics than sensing in the subcutaneous space.(report)," *Diabetes*, vol. 63, no. 7, p. 2498, 2014.

[7] G. Velho, P. Froguel, and G. Reach, "Determination of peritoneal glucose kinetics in rats: implications for the peritoneal implantation of closed-loop insulin delivery systems," *Diabetologia*, vol. 32, no. 6, pp. 331–336, 1989.

[8] B. E. A. Saleh and M. C. Teich, *Fundamentals of Photonics*. Wiley Series in Pure and Applied Optics, United States: Interscience, 2nd ed. ed., 2013.

[9] A. W. Snyder and J. D. Love, *Optical waveguide theory*, vol. 190 of *Science paperbacks*. London: Chapman and Hall, 1983.

[10] V. V. Tuchin, *Handbook of optical sensing of glucose in biological fluids and tissues*. CRC press, 2008.

[11] L. Kou, D. Labrie, and P. Chylek, "Refractive indices of water and ice in the 0.65- to 2.5-μm spectral range," *Appl. Opt.*, vol. 32, pp. 3531–3540, Jul 1993.

[12] A. K. Amerov, J. Chen, and M. A. Arnold, "Molar absorptivities of glucose and other biological molecules in aqueous solutions over the first overtone and combination regions of the near-infrared spectrum," *Applied spectroscopy*, vol. 58, no. 10, p. 1195, 2004.

[13] M. Goodarzi, S. Sharma, H. Ramon, and W. Saeys, "Multivariate calibration of nir spectroscopic sensors for continuous glucose monitoring," *Trends in Analytical Chemistry*, vol. 67, pp. 147–158, 2015.

[14] M. R. Robinson, R. P. Eaton, D. M. Haaland, G. W. Koepp, E. V. Thomas, B. R. Stallard, and P. L. Robinson, "Noninvasive glucose monitoring in diabetic patients: a preliminary evaluation.," *Clinical Chemistry*, vol. 38, no. 9, pp. 1618–1622, 1992.

[15] R. Marbach, T. Koschinsky, F. A. Gries, and H. M. Heise, "Noninvasive blood glucose assay by near-infrared diffuse reflectance spectroscopy of the human inner lip," *Appl. Spectrosc.*, vol. 47, pp. 875–881, Jul 1993.

[16] J. Tenhunen, H. Kopola, and R. Myllylä, "Non-invasive glucose measurement based on selective near infrared absorption; requirements on instrumentation and spectral range," *Measurement*, vol. 24, no. 3, pp. 173–177, 1998.

[17] R. Liu, K. Xu, Y. Lu, and H. Sun, "Combined optimal-pathlengths method for near-infrared spectroscopy analysis," *Physics in medicine and biology*, vol. 49, no. 7, p. 1217, 2004.

[18] K. H. Hazen, M. A. Arnold, and G. W. Small, "Measurement of glucose in water with first-overtone near-infrared spectra," *Appl. Spectrosc.*, vol. 52, pp. 1597–1605, Dec 1998.

[19] V. A. Saptari and K. Youcef-Toumi, "Sensitivity analysis of near-infrared glucose absorption signals: toward noninvasive blood glucose sensing," in *Proc. SPIE 4163, Optical Techniques and Instrumentation for the Measurement of Blood Composition, Structure, and Dynamics*, vol. 4163, pp. 45–54, 2000.

[20] T. Kim-Björklund, B.-M. Landgren, and L. Hamberger, "Peritoneal fluid volume and levels of steroid hormones and gonadotrophins in peritoneal fluid of normal and norethisterone-treated women," *Human Reproduction*, vol. 6, no. 9, pp. 1233–1237, 1991.

[21] J. Maathuis, P. Van Look, and E. Michie, "Changes in volume, total protein and ovarian steroid concentrations of peritoneal fluid throughout the human menstrual cycle," *Journal of Endocrinology*, vol. 76, no. 1, pp. 123–133, 1978.

[22] J. M. Anderson, A. Rodriguez, and D. T. Chang, "Foreign body reaction to biomaterials," in *Seminars in immunology*, vol. 20, pp. 86–100, Elsevier, 2008.

[23] L. C. Clark, L. K. Noyes, R. B. Spokane, R. Sudan, and M. L. Miller, "Long-term implantation of voltammetric oxidase/peroxide glucose sensors in the rat peritoneum," *Methods in enzymology*, vol. 137, pp. 68–89, 1988.

[24] M. Martins, A. Rodrigues, J. M. Pedrosa, M. J. Carvalho, A. Cabrita, and R. Oliveira, "Update on the challenging role of biofilms in peritoneal dialysis," *Biofouling*, vol. 29, no. 8, pp. 1015–1027, 2013.

[25] T. F. Cooney, H. T. Skinner, and S. M. Angel, "Comparative study of some fiber-optic remote raman probe designs. part i: Model for liquids and transparent solids," *Appl. Spectrosc.*, vol. 50, pp. 836–848, Jul 1996.

[26] K. Bescherer, D. Munzke, O. Reich, and H.-P. Loock, "Fabrication and modeling of multimode fiber lenses," *Appl. Opt.*, vol. 52, pp. B40–B45, Feb 2013.

[27] B. C. Quirk, R. A. McLaughlin, A. M. Pagnozzi, B. F. Kennedy, P. B. Noble, and D. D. Sampson, "Optofluidic needle probe integrating targeted delivery of fluid with optical coherence tomography imaging," *Opt. Lett.*, vol. 39, pp. 2888–2891, May 2014.

[28] D. G. Goebel, "Generalized integrating-sphere theory," *Appl. Opt.*, vol. 6, pp. 125–128, Jan 1967.

[29] E. S. Fry, G. W. Kattawar, and R. M. Pope, "Integrating cavity absorption meter," *Appl. Opt.*, vol. 31, pp. 2055–2065, Apr 1992.

[30] J. Hodgkinson, D. Masiyano, and R. P. Tatam, "Using integrating spheres as absorption cells: path-length distribution and application of beer's law," *Appl. Opt.*, vol. 48, pp. 5748–5758, Oct 2009.

[31] J. Erostyák, T. Jávorfi, A. Buzády, K. R. Naqvi, *et al.*, "Comparative study of integrating cavity absorption meters," *Journal of biochemical and biophysical methods*, vol. 69, no. 1, pp. 189–196, 2006.

[32] C. Zhu and Q. Liu, "Review of monte carlo modeling of light transport in tissues," *Journal of biomedical optics*, vol. 18, no. 5, pp. 050902–050902, 2013.

[33] L. Wang, S. L. Jacques, and L. Zheng, "Mcml—monte carlo modeling of light transport in multi-layered tissues," *Computer methods and programs in biomedicine*, vol. 47, no. 2, pp. 131–146, 1995.

[34] L. G. Henyey and J. L. Greenstein, "Diffuse radiation in the galaxy," *The Astrophysical Journal*, vol. 93, pp. 70–83, 1941.

[35] G. He and F. W. Cuomo, "A light intensity function suitable for multimode fiber-optic sensors," *Lightwave Technology, Journal of*, vol. 9, no. 4, pp. 545–551, 1991.

[36] B. G. Crowther, "Computer modeling of integrating spheres," *Appl. Opt.*, vol. 35, pp. 5880–5886, Oct 1996.

[37] J. Kirk, "Modeling the performance of an integrating-cavity absorption meter: theory and calculations for a spherical cavity," *Applied optics*, vol. 34, no. 21, pp. 4397–4408, 1995.

[38] D. Kato, "Light coupling from a stripe-geometry gaas diode laser into an optical fiber with spherical end," *Journal of Applied Physics*, vol. 44, no. 6, pp. 2756–2758, 1973.

[39] C. Brackett, "On the efficiency of coupling light from stripe-geometry gaas lasers into multimode optical fibers," *Journal of Applied Physics*, vol. 45, no. 6, pp. 2636–2637, 1974.

[40] Y. Ryu, Y. Shin, D. Lee, J. Y. Altarejos, E. Chung, and H.-S. Kwon, "Lensed fiber-optic probe design for efficient photon collection in scattering media," *Biomed. Opt. Express*, vol. 6, pp. 191–210, Jan 2015.

[41] M. T. Cone, J. D. Mason, E. Figueroa, B. H. Hokr, J. N. Bixler, C. C. Castellanos, G. D. Noojin, J. C. Wigle, B. A. Rockwell, V. V. Yakovlev, and E. S. Fry, "Measuring the absorption coefficient of biological materials using integrating cavity ring-down spectroscopy," *Optica*, vol. 2, pp. 162–168, Feb 2015.

[42] H. E. Bennett, M. Silver, and E. J. Ashley, "Infrared reflectance of aluminum evaporated in ultra-high vacuum," *J. Opt. Soc. Am.*, vol. 53, pp. 1089–1095, Sep 1963.

Appendix A: Monte Carlo implementation

The Monte Carlo model was implemented in standard C++98 and compiled with G++ on a Linux based system. The Mersenne Twister algorithm, implemented in the Gnu Scientific Library (GSL), was used as the PRNG. The implementation is object oriented, and is not especially focused on performance. The time required for tracing a single photon with high precision in turbid media is typically on the order of 1 μs. As the full model consists of a few thousand lines of code, the code will not be listed in this thesis. The code is uploaded to Github and is freely available (`https://github.com/permagnusw/MC_photonTransport.git`). The code may also be supplied upon request.